Statistical analysis and intercomparison of WAM model data with global ERS-1 SAR wave mode spectral retrievals over 3 years

P. Heimbach, S. Hasselmann, and K. Hasselmann

Max-Planck-Institut für Meteorologie, Hamburg, Germany

Abstract. Ocean wave spectra were retrieved from a set of ERS-1 synthetic aperture radar (SAR) wave mode (SWM) spectra between January 1993 and December 1995. An assessment is given of the SWM data quality and the retrieval performance as well as the operational feasibility of the retrieval algorithm. Sensitivity studies are performed to demonstrate the weak residual dependence of the retrieval on the first-guess input spectrum. The mean spectral parameters of the SWM retrievals are compared with spectral parameters from collocated wave model (WAM) spectra. The time series of SWM-retrieved and WAM-derived monthly mean significant wave heights H_s in various ocean basins show good overall agreement but with a small systematic underestimation of H_s by the WAM. A decomposition of the wave spectra into wind sea and swell reveals an average 10% overprediction of the wind sea by the WAM while swell is underpredicted by 20–30%. The positive wind-sea bias exhibits no clear wave height dependence, while the negative swell bias decreases with swell wave height. This could be due to a too strong damping in the WAM at low frequencies. Detailed regional investigations point to the existence of smaller-scale phenomena, which may not be adequately reproduced by the WAM at the present resolution of the wind forcing. Finally, an intercomparison is made of the observed and modeled azimuthal cutoff length scales, and global distributions are investigated. Ratios of the observed azimuthal cutoff wavenumber to the mean azimuthal wavenumber component indicate that about 75% of the swell can be directly resolved by the SAR, while about 70% of the wind sea lies at least partially beyond the cutoff.

1. Introduction

One of the major drivers of the first European Remote Sensing Satellite ERS-1, launched on July 17, 1991, was the applications in wave research and wave forecasting. Through the wave mode [see, e.g., *European Space Agency (ESA)*, 1993; *Brüning et al.*, 1994] of the synthetic aperture radar (SAR) [see, e.g., *Harger*, 1970; *Allan*, 1983; *Bamler and Schättler*, 1993], ERS-1 provided, for the first time, detailed spectral information on the sea state globally, continuously, and in quasi-real time, far beyond the capabilities of other wave observation systems.

The development of improved ocean wave models for operational wave forecasts and the computation of wave climatologies from past wind field data is of considerable economic benefit for numerous activities, such as ship routing, fisheries, offshore operations, and coastal protection [see, e.g., *ESA*, 1996]. Beyond these practical applications an understanding of the dynamics of waves is essential also for an improved understanding of the mechanisms that govern the transfer of momentum, sensible and latent heat, and gases such as CO_2 across the air-sea interface, an area of research that is rapidly gaining significance through the development of sophisticated global coupled ocean-atmosphere carbon cycle climate models [*Komen et al.*, 1994; see also *Weber et al.*, 1993; *Mastenbroek et*

al., 1993; *Jähne and Monahan*, 1995; *Janssen and Viterbo*, 1996; *Weisse and Alvarez*, 1997].

An accurated representation of the wind stress from air-sea bulk transfer coefficients, especially the relationship between the wind stress, wind profile, and sea state, is important for studies of the wind-driven ocean circulation. The dependence of wind stress on sea state is still an open question [see, e.g., *Geernaert*, 1990; *Komen et al.*, 1998]. Although recent analyses of Humidity Exchange Over the Sea Main Experiment (HEX-MAX) (1986) data from the Humidity Exchange Over the Sea Experiment (HEXOS) project [see *Smith et al.*, 1992; *Janssen*, 1997] suggest only a limited sea state dependence, *Rieder et al.* [1994] and *Fairall et al.* [1996], from the analysis of data from the Surface Waves and Processes Program (SWAPP) campaign (1990) and the Tropical Ocean-Global Atmosphere Coupled Ocean-Atmosphere Response Experiment (TOGA COARE) project, respectively, report deviations between the directions of the wind stress and the wind velocity under the influence of swell. The investigations of data from the SWAPP campaign (1990) by *Large et al.* [1995] and from the Ocean Storm Experiment (1987) by *Rieder* [1997] also indicate a complex dependence of the sea surface drag on the wind profile and the wind-sea and swell components of the sea state. The new information from ERS-1/2, including both wave spectral data and scatterometer wind measurements, could aid significantly in shedding light on the relevant mechanisms. Long-term climatologies based on continuous global wave field observations would furthermore be valuable for assessing possible changes of wave climate due to global greenhouse warming or other climate changes [see, e.g., *Bacon and Carter*,

1991; *von Storch et al.*, 1993; *Wave and Storms in the North Atlantic (WASA) Group*, 1995; *Bouws et al.*, 1996].

The potential of forthcoming ERS-1 wave data has been a strong motivation for significant advances in wave modeling and methods of satellite data assimilation (compare the detailed presentation in work by *Komen et al.* [1994]). However, we shall not discuss the various proposed wind and wave data assimilation schemes for modern third-generation wave models in this paper [see, e.g., *Hasselmann et al.*, 1988; *Lionello et al.*, 1992, 1995; *Hasselmann et al.*, 1994; *Bauer et al.*, 1996b; *Hasselmann et al.*, 1997; *Breivik et al.*, this issue], but will focus rather on the analysis of the imagette spectra provided by the ERS-1 SAR wave mode (SWM) data and the applicability of the data for wave model validation.

The period of our analysis extends over the 3-year period January 1, 1993, to December 31, 1995, for which reliable ERS-1 SWM data were available. Prior to January 1, 1993, the SWM product was still in a process of modification. On April 21, 1995, ERS-2 was launched. It has now replaced ERS-1 in providing near–real-time global SWM data. It is hoped that the continuity and operational application of global SAR wave data will be ensured in the future through the launch of ENVISAT in 1999, for which an advanced SAR (ASAR) is foreseen [*ESA*, 1997].

The retrieval of ocean wave spectra from SAR imagette spectra is not a simple exercise. The SAR imaging mechanism is strongly nonlinear through the distortions induced by the wave orbital motions (the "velocity bunching mechanism," compare the MARSEN review in work by *K. Hasselmann et al.* [1985]). This results, among other effects, in image smearing and a loss of information beyond the so-called azimuthal cutoff wavenumber, corresponding typically to wavelengths shorter than about 100–200 m in the satellite flight direction. In addition, ocean wave spectra from satellite SAR images suffer from a basic 180° frozen-image ambiguity. This shortcoming can in principle be overcome by making use of the information on the wave propagation direction contained in successive components of multilook images [e.g., *Young et al.*, 1985; *Vachon and Raney*, 1991; *Johnsen*, 1992; *Bao and Alpers.*, 1998; *Engen and Johnsen*, 1995]. However, although the feasibility has been demonstrated, the technique has not yet been implemented operationally. Nevertheless, even with these limitations, *Hasselmann and Hasselmann* [1991] (hereinafter referred to as HH) were able to develop an efficient inversion algorithm enabling a reliable retrieval of ocean wave spectra from SAR spectra within the computational constraints of real-time operational applications [see also *Krogstad*, 1992; *Bao et al.*, 1994; *Krogstad et al.*, 1994]. An improved algorithm has recently been proposed by *S. Hasselmann et al.* [1996] (hereinafter referred to as HBHH). This retrieval algorithm has been used in the present study.

The WAM model plays a central role in our analysis [*Wave Model Development and Implementation (WAMDI) Group*, 1988]. It is used to provide the first guess for the wave spectral retrievals, and we use the WAM model predictions again in intercomparing the modeled and retrieved wave spectra. However, the approach is not as circular as this may appear, since it has been demonstrated by HBHH and is further verified in this paper that the improved retrieval algorithm used here is insensitive to the initial input spectrum. The first-guess information is used essentially only to remove the 180° ambiguity and augment the retrieved spectrum beyond the azimuthal cutoff.

The WAM model now runs routinely at most operational forecasting centers and has been implemented at more than 100 research institutions. It has been extensively validated through case studies and field data, including fetch-limited wave growth conditions and extreme storm conditions, and on a statistical basis against buoy data [see *Komen et al.*, 1994].

Validation of the WAM model using spaceborne data has so far been limited to H_s data derived from satellite altimeters. A comprehensive compilation of WAM validation studies using spaceborne altimeter data from Seasat (1978), Geosat (1985–1989), ERS-1 (1991–1996), and TOPEX/POSEIDON (since 1992) as well as a global comparison between collocated ERS-1 and TOPEX altimeter significant wave heights is given by *Bauer and Staabs* [1998].

Most validation exercises indicate a good overall agreement between the model and observations, but significant differences are nevertheless occasionally found. The discrepancies tend to differ from study to study and have usually been attributed to errors in the forcing wind field or, in some cases, to inadequate model resolution. Small systematic deviations of the model from a larger ensemble of altimeter wave height data have also been partly attributed to differences in the instrument calibrations or in the sensor algorithms or to differences in the spatial and temporal sampling. In their intercomparison of altimeter data from different satellites, *Bauer and Staabs* [1998] state that no definite conclusion can yet be drawn regarding which altimeter wave height data set is closest to the true sea state. Nevertheless, such intercomparisons, in conjunction with model data, are helpful in clarifying the characteristics of the different data sets and identifying possible error sources in either the data or the model.

Although providing continuous global coverage, altimeter data suffer from the basic limitation of yielding only significant wave heights. When trying to detect detailed deficiencies in the spectral properties of a wave model, validation studies based on altimeter data alone are therefore of restricted value. The SAR is at present the only instrument able to provide the required detailed two-dimensional spectral data with continuous global coverage. Following demonstrations of the feasibility of retrieving wave spectra from SAR image spectra for aircraft and the first ocean satellite Seasat [*Hasselmann et al.*, 1991], a first validation of the ERS-1 SAR wave mode was carried out for a limited 3-day data set in the Atlantic [*Brüning et al.*, 1993, 1994]. Various aspects of the ERS-1 SWM product have been investigated also by other authors [e.g., *Krogstad*, 1994; *Hansen et al.*, 1994; *Chapron et al.*, 1995; *Breivik et al.*, 1995; *K. Hasselmann et al.*, 1996; *Heimbach et al.*, 1996; *Kerbaol and Chapron*, 1996; E. Bauer and P. Heimbach, manuscript in preparation, 1998]. However, the present study represents the first attempt at a global assessment of the complete ERS-1 SWM data set.

In our intercomparison of retrieved SAR wave spectra with the WAM model over the 3-year period effectively covered by ERS-1, we shall be able to validate not only the SAR wave mode data product and retrieval algorithm but also the WAM model at a higher level of spectral detail than was previously feasible. However, in considering the full ERS-1 data set we have necessarily had to restrict the analysis to an essentially statistical investigation. We hope that the general results presented here will nonetheless reveal a number of interesting features that will stimulate further detailed case studies addressing specific dynamical questions.

The paper is organized as follows. Section 2 briefly reviews

the basic inputs to the SAR spectral retrieval algorithm, describing the SAR wave mode data (section 2.1), the nonlinear wave-to-SAR spectral mapping relation and inversion technique (section 2.2), and the WAM model (section 2.3). The retrieval process is assessed in section 3 with respect to the quality of the input SWM data (section 3.1), the fidelity of the retrieval, as expressed by the correlation between the observed and simulated SAR spectra (section 3.2), and the sensitivity of the retrieval with respect to the first guess (section 3.3). In section 4 the spectral retrievals are intercompared with the WAM model spectra. Time series of monthly mean significant wave heights and regression coefficients are presented for the total wave field in section 4.1 and for separate wind-sea and swell contributions in section 4.2. More detailed regional and zonal intercomparisons of wind-sea and swell wave heights, wavelengths, and directions are presented in section 4.3. Case studies for the South Pacific Ocean, a meridional data section through the mid-Pacific, and a global analysis of long-swell components are discussed in sections 4.4, 4.5, and 4.6, respectively. In section 5 the observed and simulated azimuthal cutoff parameters characterizing the nonlinearity of the SAR imaging process are intercompared, the impact of the cutoff on the retrieval of swell and wind-sea systems is investigated, and a proposed dependence of the cutoff on the wind speed is tested. The principal conclusions of our investigation are summarized in section 6.

2. Derivation of Wave Spectra From ERS-1 SAR Wave Mode Data

2.1. ERS-1 SAR Wave Mode Fast Delivery Product

The operation of the ERS-1 synthetic aperture radar (SAR) in the intermittent sampling wave mode provided for the first time global two-dimensional wave spectral data in near-real time. In contrast to the 100- × 100-km full-swath SAR image mode, which can be operated only during maximally 10% of the orbit and while in line-of-sight of a ground station, the SAR wave mode (SWM) 10- × 5-km snapshot imagettes are recorded every 200 km along the satellite track. The data are stored on board and transmitted once per orbit to the ERS ground stations. This yields a daily coverage of the global wave spectral field (with occasional gaps when the SAR was operated in full-swath mode) at an along-track resolution comparable with the model resolution, but with a lower cross-track resolution of order 1000–2000 km. The imagettes are fast Fourier transformed to 512 × 512 wavenumber spectra, which are subsequently averaged and converted to 12 × 12 polar wavenumber coordinates (see Table 3; detailed descriptions are given in work by ESA [1993], Brooker [1995], and Hasselmann et al. [1998]).

The European Space Research Institute (ESRIN) at Frascati, Italy, distributes the European Space Agency (ESA) fast delivery product (FDP) in quasi-real time to the major operational forecasting centers. We received the FDP via the United Kingdom Meteorological Office (UKMO) at Bracknell, England, and the Deutscher Wetterdienst (DWD) at Offenbach, Germany.

2.2. Retrieval of Wave Spectra From SAR Wave Mode Spectra

2.2.1. Closed nonlinear spectral integral transform. The nonlinear imaging theory of ocean waves by a SAR is by now well understood (compare the Marine Remote Sensing Exper-

iment (MARSEN) review by K. Hasselmann et al. [1985]). The imaging is produced by two mechanisms: the linear real aperture radar (RAR) modulation of the backscatter cross section and the orbital motion effects that induce Doppler shifts modifying the phase history of the backscattering signals used to reconstruct the SAR image. The RAR modulation is caused by hydrodynamic interactions between the short backscattering Bragg waves and long waves and the tilting of the backscattering surface by the long waves. The orbital motion Doppler shifts produce azimuthal displacements of the backscattering elements in the SAR image plane, leading to a redistribution of the apparent backscattering density ("velocity bunching"). If the azimuthal displacements become comparable with a typical ocean wavelength, the image becomes nonlinearly distorted. For large displacements compared with a wavelength the image is effectively smeared out. This occurs at the so-called high-wavenumber azimuthal cutoff of the SAR image spectrum.

First simulations of the fully nonlinear velocity bunching mechanism were achieved using Monte Carlo methods [see Alpers, 1983; Alpers et al., 1986; Brüning et al., 1990]. This technique, however, requires considerable computing time and does not lend itself readily to an inversion, as required for the construction of a retrieval algorithm.

The inversion problem became tractable through the derivation of a closed nonlinear integral expression for the mapping of the ocean wave spectrum into a SAR image spectrum [HH; see also Krogstad, 1992; Bao et al., 1994; Krogstad et al., 1994]. The nonlinear integral can be represented as the Fourier transform of a nonlinear function of the auto- and cross-covariance functions $f^R(\mathbf{r})$, $f^v(\mathbf{r})$ and $f^{Rv}(\mathbf{r})$ of the RAR image intensity $I^{RAR}(\mathbf{r})$, and the orbital velocity $v(\mathbf{r})$. It contains an exponential cutoff factor $\exp[-k_x^2 \xi^2]$ that describes the azimuthal falloff of the image spectrum beyond an azimuthal cutoff wavenumber k_x, where $\xi = v \cdot R/U$ is the root-mean-square (rms) azimuthal displacement, given by the product of the rms orbital (range) velocity v and the range-to-platform velocity ratio $\beta = R/U$ (see HH).

The imaging theory and nonlinear mapping relation have been verified in a number of field experiments with airborne SARs, such as the Labrador Extreme Waves Experiment (LEWEX) [see Beal, 1991] and the Synthetic Aperture Radar and X Band Ocean Nonlinearities—Forschungsplattform Nordsee (SAXON—FPN) campaign [see Plant and Alpers, 1994] as well as with spaceborne SARs on board Seasat (see the special Seasat issue of the Journal of Geophysical Research (volume 88, number C3) and Hasselmann et al. [1991]), the space shuttle missions shuttle imaging radar B (SIR-B) [e.g., Alpers et al., 1986; Monaldo and Lyzenga, 1988; Brüning et al., 1988], and the Grand Banks ERS-1 SAR Wave Spectra Validation Experiment, which also included a validation against airborne SARs (see the special issue of Atmosphere Ocean (volume 32, number 1) and the ALMAZ-1 satellite mission [Wilde et al., 1994]).

For aircraft SARs the quasi-linear approximation of the SAR imaging expression, obtained by terminating the Fourier series expansion after the first linear terms but retaining the nonlinear exponential azimuthal cutoff factor, is often an acceptable approximation [see e.g., Monaldo and Lyzenga, 1986; Beal et al., 1991; Monaldo and Beal, 1995, and references therein]. However, the quasi-linear approximation is unable to account for the nonlinear image distortions inherent in the imaging process for the high range-to-platform velocity ratios
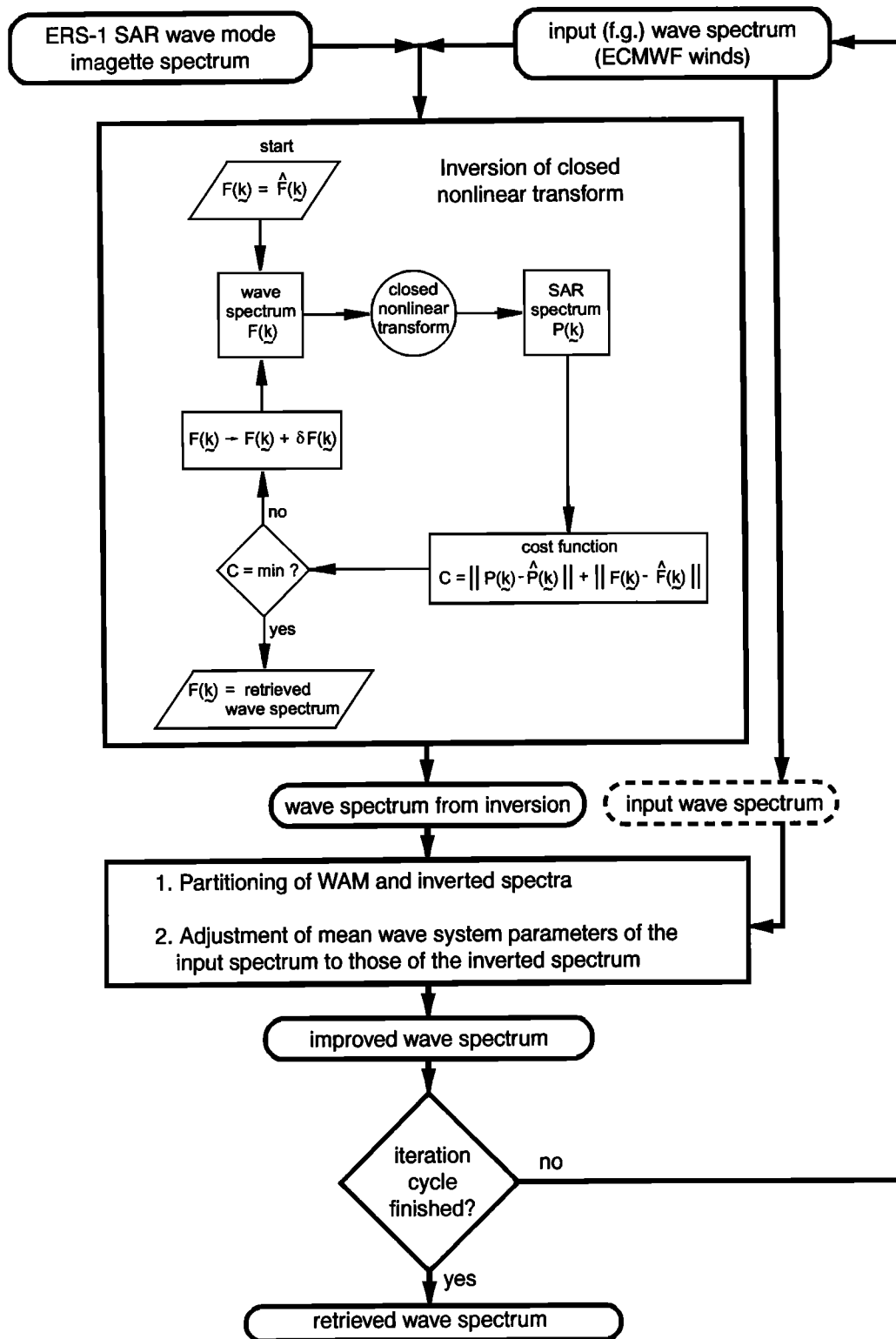
Figure 1. Flow chart of the retrieval algorithm showing the inner loop iterative inversion procedure of the closed nonlinear transform and the outer loop iterative updating of the input spectrum using a spectral wave partitioning scheme.

typical of satellite SARs (for ERS-1, $R/U = 112$ s, which is much larger than typical R/U ratios for low-flying aircrafts).

2.2.2. Retrieval algorithm. Subsequent to their derivation of the nonlinear integral transform, HH presented an algorithm for inverting the spectral mapping relation. Their

retrieval algorithm has since been extended (HBHH) by adding an explicit cutoff adjustment term to the cost function and a second iteration loop that successively modifies the first-guess input spectrum (see flow chart, Figure 1 and section 3.3). The latter extension effectively decouples the retrieval from

the original first-guess spectrum. As one of the aims of this paper is to assess the performance of the improved retrieval algorithm, we briefly review the main features of the technique.

2.2.2.1. Inversion of the nonlinear transform: The first step of the retrieval algorithm is the inversion of the nonlinear spectral mapping relation for a given first-guess input spectrum by minimizing a suitably defined error cost function (inner iteration loop in Figure 1). A first guess is required for two reasons.

1. Since the standard SAR product is an image of the instantaneous sea surface, it contains a 180° directional ambiguity. The ambiguity can be resolved only through additional information from a first-guess spectrum.

2. The nonlinear velocity bunching mechanism smears out the short wave components beyond an azimuthal cutoff wavenumber dependent on the rms orbital velocity. The missing information must again be augmented by a first-guess wave spectrum. However, this limitation is partially overcome by HBHH by including an explicit penalty term in the cost function for errors in the azimuthal cutoff (not shown in Figure 1), which is sensitive to short waves beyond the cutoff (see section 5 for a validation of the cutoff fitting procedure).

A valuable feature of the SAR spectral retrieval algorithm is the availability of an internal calibration based on the level of the background clutter spectrum. Thus the retrieved spectra can be calibrated in absolute wave height units without reference to the SAR instrument calibration or measurements of the absolute backscattering cross section [see *Alpers and Hasselmann*, 1982; *Brüning et al.*, 1994].

2.2.2.2. Spectral partitioning and iterative updating of the input spectrum: Although the overall level of the high wavenumber part of the spectrum is adjusted through the inclusion of an explicit azimuthal cutoff penalty term in the cost function, the inversion method modifies the detailed form of the spectrum only in the main part of the spectrum for which direct SAR spectral information is available. A straightforward inversion of the SAR spectrum therefore normally leads to unrealistic discontinuities in the transition zone near the azimuthal cutoff wavenumber separating the spectral regions with and without direct SAR information (HH).

This difficulty is overcome in the revised algorithm of HBHH by introducing a spectral partitioning scheme into the additional iteration loop that updates the input spectrum (compare Figure 1). The iteration consists of repeatedly replacing the input spectrum used for the inversion for the iteration cycle $k + 1$ by the wave spectrum derived from the inversion in the previous iteration cycle k. However, instead of simply replacing the spectra wavenumber by wavenumber, the transfer is implemented via a spectral partitioning scheme (a modified form of the original partitioning algorithm of *Gerling* [1992]; see *Brüning et al.* [1994] and HBHH). This effectively extends the available SAR information below the azimuthal cutoff into higher wavenumbers beyond the cutoff. The new input spectrum retains the continuity properties of the original input spectrum, but the scales and propagation directions of the wave systems of the new spectrum are adjusted to the inverted spectrum. For details we refer to HBHH.

In the present study, five iterative updates of the input spectrum were carried out. As discussed by HBHH, the iteration leads to a closer agreement between the observed and simulated SAR spectrum for the first iteration cycles but then often begins to diverge. We have accordingly selected as the best retrieval the solution that yields the smallest dimensionless square error ε between the SAR spectrum computed from the
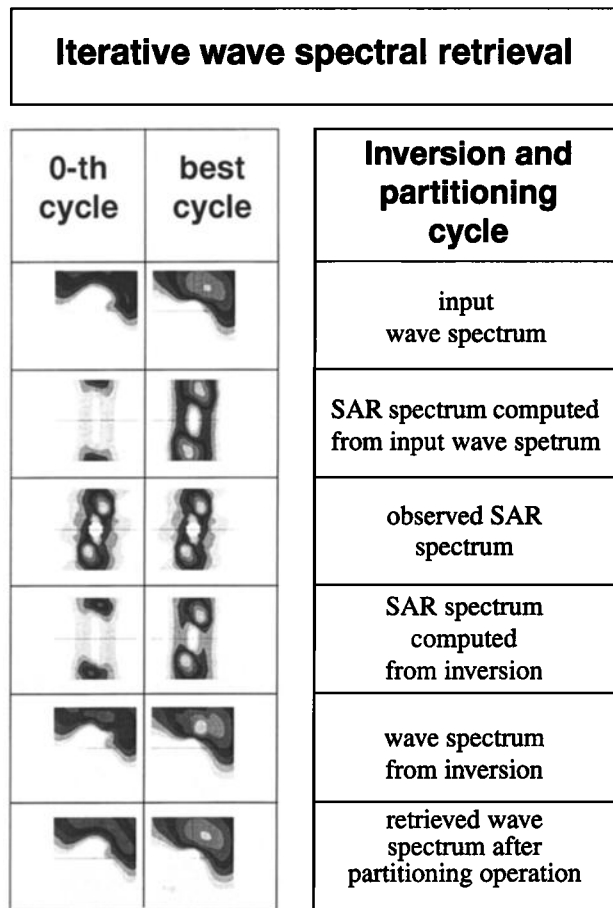

Figure 2. Example of the iterative wave spectral retrieval operation on a Cartesian 128 × 128 wavenumber grid.

input wave spectrum and the observed SAR spectrum (compare HBHH and Figure 2).

2.3. WAM Model

The wave model spectra used as first-guess input for our retrievals (and for the later retrieval-model intercomparisons) were computed with the ECMWF operational wave forecast model WAM cycle 4 every 6 hours on a global 3° × 3° (since July 1994, 1.5° × 1.5°) latitude-longitude grid [*Janssen et al.*, 1996]. As wind forcing, we used the ECMWF analyzed wind field u_{10} at 10-m height. For the period of the present analysis, ERS-1 scatterometer winds were not yet being assimilated into the analysis [see *European Centre for Medium-Range Weather Forecasts (ECMWF)*, 1995].

The WAM model solves the energy balance equation

$$\frac{D}{Dt} F = \frac{\partial}{\partial t} F + \frac{1}{\cos \varphi} \frac{\partial}{\partial \varphi} (\dot{\varphi} \cos \varphi F) + \frac{\partial}{\partial \psi} (\dot{\psi} F) + \frac{\partial}{\partial \theta} (\dot{\theta} F)$$

$$= S_{in} + S_{nl} + S_{ds} \tag{1}$$

for the two-dimensional wave spectrum $F = F(f, \theta; \varphi, \psi, t)$ as a function of frequency f and direction θ on a spherical coordinate grid φ, ψ (see appendix, section A2). The source terms on the right-hand side are integrated using an implicit integration scheme with a time step of 15 min, while the integra-

tion of the advection terms on the left-hand side is performed using a first-order upwind scheme with a time step of 30 min.

As a third-generation model (as opposed to second-generation models), the WAM model introduces no prior assumptions on the shape of the spectrum but determines the evolution of the spectrum by direct integration of the transport equation from first principles, as expressed by the structure of the three source terms as follows [*WAMDI Group*, 1988; *Günther et al.*, 1992; *Komen et al.*, 1994].

1. The input term S_{in} describing the wind forcing is proportional to the wave spectrum. In WAM cycle 4 used in the present study the wind input is based on *Miles'* [1957] critical layer mechanism for laminar flows as adopted by *Snyder et al.* [1981], with modifications by *Janssen* [1989, 1991, 1992] to include the effect of a wave-induced stress τ_w.

2. The nonlinear transfer term S_{nl} is represented by the so-called direct interaction approximation of the full Boltzmann collision integral expression describing the conservative spectral energy transfer due to resonant weak nonlinear wave-wave interactions [see *Hasselmann and Hasselmann*, 1985; *S. Hasselmann et al.*, 1985, and references therein].

3. The dissipation term S_{ds} is the least well known. The dominant dissipation process is generally regarded as whitecapping, which involves many scales of breaking waves. However, as a process which is weak in the mean, it follows from general principles [*Hasselmann*, 1974] that it can normally be represented as a quasi-linear process. The form implemented in WAM cycle 4 is based on a parameterization explored by *Komen et al.* [1984] and extended by *Janssen* [1991].

3. Retrieval Assessment

An assessment of the overall performance of the combined ERS-1 SAR wave mode system and retrieval procedure involves several complementary aspects.

1. The first aspect is data quality, which concerns the quality of the SWM product in terms of signal-to-noise and contamination with nonwavelike features [HH; *Brüning et al.*, 1994]. Nonlinear image distortions, on the other hand, as an inherent property of the measurement mechanism, are not regarded as a quality reduction of the SWM product.

2. The second aspect is retrieval performance, which refers to the ability of the retrieved wave spectrum to reproduce the observed SAR spectrum. If the SAR spectrum computed from the retrieved wave spectrum via the full nonlinear forward transform agrees closely with the observed wave spectrum, as measured, for example, by the normalized spectral error, the retrieval has high fidelity. This is clearly the first goal of a retrieval algorithm. A retrieval with high fidelity has extracted all the information that is available from the SAR spectrum [see HH; *Brüning et al.*, 1994; HBHH]. An assessment of the retrieval fidelity or performance together with the data quality is given in section 3.1.

3. The third aspect is retrieval validation, which assesses the degree of agreement of the retrieved spectrum with the true wave spectrum. We shall address this problem in later sections of this paper by intercomparing the retrievals with model data. A comparison with model data has the advantage that both data sets are available globally for the complete two-dimensional wave spectra and throughout the entire 3-year analysis period. But the approach naturally raises the question whether model spectra can be regarded as reasonable approximations of the true wave spectra. However, this is a basic shortcoming of all intercomparisons. Normally, it is not possible to regard either of the two data sets of an intercomparison as a faithful replica of the true state. All one can do is cross-validate the data in an attempt to gain a synthetic assessment of both data sets, taking into account their individual shortcomings.

Validation of ERS-1 SAR retrievals against other wave observations has been undertaken to date only for wave height data from satellite altimeters. Unfortunately, although satellite altimeters also provide global continuous coverage, the lack of detailed spectral information limits the value of such validation exercises. Nevertheless, a global intercomparison of a 1-year global data set of significant wave heights retrieved from ERS-1 SWM with collocated TOPEX/POSEIDON altimeter data has recently been performed by E. Bauer and P. Heimbach (manuscript in preparation, 1998). A regional stratification of the data similar to that introduced here (see section 4) exhibited good overall agreement between SWM-retrieved and altimeter wave heights but indicated some differences between the altimeter wave heights. The ERS-1 altimeter H_s data were found to be generally lower by an average of 0.2 m than the other two data sets. The TOPEX data agreed to within 5–10% with the SWM data in the tropics throughout the year and in the extratropics during summer, i.e., generally for low sea states. However, they were systematically higher by about 15% in the midlatitude winter, i.e., for high sea states. In general, the validation exercise indicated a satisfactory overall accuracy of SWM-retrieved significant wave heights.

4. The last aspect is operational efficiency. Three considerations are relevant for the assessment of operational efficiency: (1) the number of SWM spectra delivered to the operational forecast center (in the present case, ECMWF) in quasi-real time per month, or, equivalently, the percentage of time that the end-to-end SWM system was functioning satisfactorily in the operational quasi real-time mode; (2) the percentage of the received SWM spectra for which the operational center was able to provide collocated first-guess wave spectra as input for the retrievals; failure to provide an input spectrum can be either due to reception of the SWM product outside the relevant operational time window (which is classed as a failure of the delivery system), or to system interruptions at ECMWF; and (3) the computational load of the operational production of global SWM spectral retrievals; at a peak frequency of one SWM spectrum every 30 s it is imperative to keep central processing unit (cpu) time low; this requires a trade-off between the number of iterative cycles of the input wave spectrum and cpu time.

We shall study the first two considerations regarding the production reliability in section 3.1 and study the third consideration of computational efficiency in section 3.2. A sensitivity analysis of the retrieval with respect to the first-guess input spectrum is given in section 3.3.

3.1. Data Quality and Retrieval Performance

The 3-year set of ERS-1 SWM data between January 1993 and December 1995 comprises a total of some 1.2 million wave spectra with an average daily output of 1100 spectra. The number of monthly available SWM spectra is shown in Figure 3. The dark column segments indicate the number of fast delivery product (FDP) spectra for which no first-guess model spectra were available. The envelope of the FDP columns shows a high value from the outset. A low FDP content was found during the summer seasons 1993 and 1994. For summer 1993 this can be explained by a change in the setup of the operational wave-forecasting facilities; the origin of the second minimum is not clear.
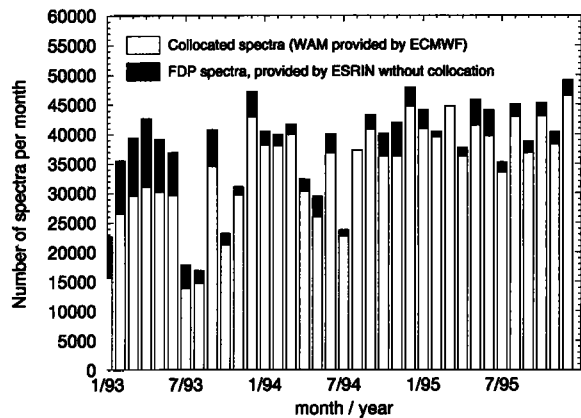
Figure 3. Number of monthly available ERS-1 synthetic aperture radar (SAR) wave model (SWM) data. SWM spectra that could be collocated with wave model (WAM) spectra are represented by the light lower column segments; those for which no first-guess model spectra were available are represented by the dark upper segments.

The retrieval process incorporated two quality tests: a data quality test for the input SWM data and a fidelity test for the retrieval. The input SWM data was rejected if the signal-to-noise ratio of the image spectrum (defined as the ratio of the spectral peak to the clutter noise background) was less than 3 dB or if the first-guess wave height was below 0.1 m. The retrieved spectra were discarded if the cost function was not reduced to less than half of its initial value. Furthermore, all spectral information beyond 800 m wavelength was excluded. These frequently represent nonwavelike sea surface features like slicks, wind rows, etc. [Brüning et al., 1994]. Statistical analyses (compare section 4) indicate that swell of extreme wavelengths beyond 800 m are rare.

Figure 4 shows that with the beginning of the quasi real-time distribution of the FDP through the European Space Research Institute (ESRIN) in February 1993, maximally 2% of the data

showed low signal-to-noise ratios. Another 10% of the data were rejected because the first-guess wave height was too low ($H_s < 0.1$ m).

For roughly 85% of the remaining data the retrieval algorithm achieved an acceptable performance, with cost function reductions to <0.5 of the initial value, while for one third a reduction factor of <0.1 was achieved. Spectra with a cost function reduction factor lower than 0.5 for which the azimuthal clutter cutoff adjustment or the convergence of the iterative inversion procedure was poor were nevertheless retained in the subsequent analysis, as their fidelity measured in terms of the pattern correlation coefficient was generally still acceptable. The remaining 15% inversions, for which the ratio of the final to initial cost could not be reduced below 0.5, generally exhibited relatively low pattern correlations between the simulated and observed SAR spectra and were discarded from the further analysis. The number of monthly available SWM-retrieved spectra that passed both tests is geographically relatively homogeneous and is varied with the size of the ocean basin from 1500 in the North Atlantic to 5000 in the tropical Pacific.

The retrieval performance is represented in Figure 5 in terms of the distributions of the pattern correlation coefficients for the simulated and observed SAR spectra for the summer 1994 and winter 1994–1995 seasons in the northern and southern hemisphere. All distributions show a rather narrow peak around 0.9, indicating that for the major part of the data successful retrievals of high fidelity were achieved. The winter distributions in both hemispheres appear to be peaked toward slightly higher correlations than the summer distributions, suggesting that the retrieval performance is generally higher for high sea states (as may be expected from the generally higher signal-to-noise ratios for higher sea states).

3.2. Iteration Procedure

As described in section 2.2.2, five iterations of the input wave spectrum were carried out, and the inversion that yielded the smallest error between the observed and simulated SAR spectrum was then selected as the final retrieval. A time series of
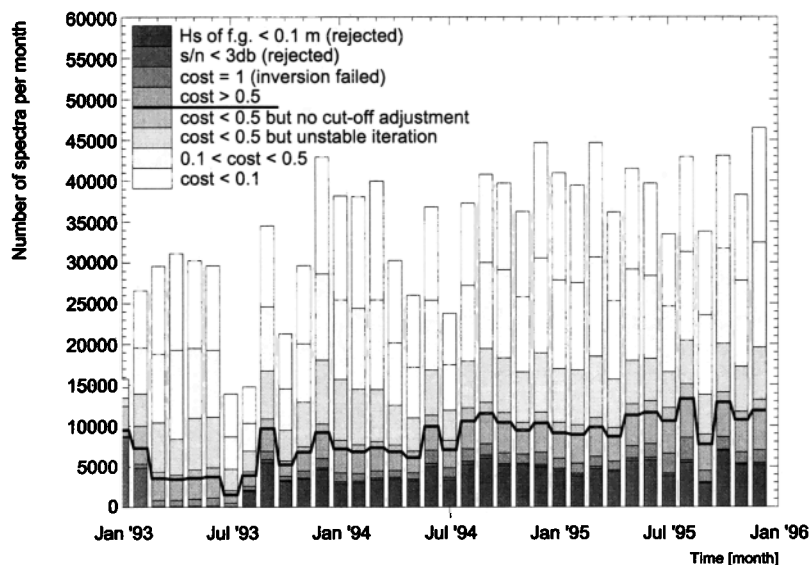

Figure 4. Data quality and performance of the retrieval algorithm measured in terms of the cost function reduction factor. Retrievals with a cost function reduction below 0.5 are regarded as reliable (above thick solid line). For data of too poor quality, no retrieval was attempted (below thick solid line).
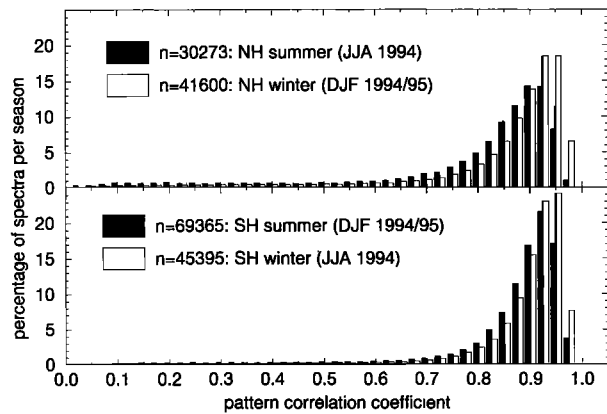
Figure 5. Fidelity of the retrieval algorithm measured in terms of the pattern correlation coefficient between the observed and simulated SAR image spectrum in the (top) northern hemisphere and (bottom) southern hemisphere.

the monthly distribution of the number of iterations yielding the best retrieval revealed a stable behavior throughout the 3 years. Table 1 shows the average percentage of spectra for which N iterations of the input spectrum yielded an optimal retrieval. For about 92% of the retrievals an iteration of the input spectrum yielded an improvement, 75% showing a further improvement for more than one iteration. For operational applications a trade-off must be sought between computing time and the improvement in retrieval with increasing number of iterations. We discuss the trade-off first with respect to the impact on the retrieval fidelity, as expressed by the pattern correlation between the simulated and observed spectrum, and subsequently with respect to actually retrieved wave parameters.

The rate at which the error between the simulated and observed image spectrum decreases with the number of iterations, given the number of iterations N for an optimal retrieval, is illustrated in Figures 6a and 6b, which show the histograms of the pattern correlation for August 1995 northern and southern hemisphere, respectively. The total set of spectra for each hemisphere is divided into five samples $S_0, \cdots, S_4$, where S_N denotes the set of spectra for which the optimal retrieval was achieved after N iterations (the last iteration set S_5 is not considered in this analysis because it also contains spectra that would have required more than five iterations for an optimal retrieval). All histograms are normalized to unit integral values. The graphs correspond, from bottom to top, to spectra requiring zero, one, two, etc. iterations for optimal retrieval, and for each sample S_N the evolution of the histogram from iteration to iteration is depicted by $N + 1$ distribution curves.

Table 1. Percentage of Spectra for Which N Iterations Yielded an Optimal Retrieval

Number of Iterations (N)	Number of Spectra, %
0	8
1	17
2	17
3	15
4	13
≥ 5	30

The behavior is similar in both hemispheres. The largest impact on the retrieval is found in performing the first iteration. The impact of subsequent iterations diminishes with increasing N.

As an alternative way of assessing the impact of the number of iterations on the retrieval performance, we used the same data sample of August 1995 to carry out a series of retrieval experiments in which the number of input iterations was set at a different fixed number M in each experiment. The best of the M iterations, defined in terms of the dimensionless error, was then taken as the retrieval. For each experiment this yielded a distribution curve of the pattern correlation index, shown in Figure 7 for the northern and southern hemispheres. The distributions are qualitatively similar to Figure 6. Both results suggest that at least one iteration should be carried out and that two iterations may represent an acceptable trade-off of retrieval improvement against computing time; the additional improvements beyond $M = 2$ tend to be rather small.

To assess the impact of the number of iterations not only on the fidelity measure but also on the retrieved wave parameters, a regression was carried out between the significant wave heights H_s of the retrieved spectra with and without iteration of the input spectrum. The regression parameters listed in Table 2 confirm that the retrieved wave heights do indeed converge with increasing iteration. The largest change is found as before for the first iteration, but the step from one to two iterations is also nonneglible, supporting the previous conclusion that it appears advisable to carry out at least one but preferably two iterations.

3.3. Sensitivity of the Retrieval With Respect to the First Guess

Through the inclusion of the deviation between the first-guess (fg) input spectrum and the inverted spectrum as a (weakly weighted) regularization term in the cost function, the retrieved spectrum tends to be biased toward the input spectrum. However, the bias is systematically reduced in the HBHH scheme through successive iterations of the first-guess input. In this section we investigate the sensitivity of the retrieval with respect to the first-guess input spectrum.

Three forms of synthetic modifications of the input spectrum were investigated: an increase or decrease in energy, a frequency scale change, and a rotation. In all cases the modifications were largely eliminated in the retrieved spectra. We discuss in the following in detail only the impact of doubling the wave height or increasing the energy by a factor of 4. The impact is illustrated first for four typical wave spectra corresponding to the various combinations of azimuth or range traveling waves in strong or light winds.

Plates 1a–1d depict the various retrieval steps of the four spectra. In all cases it is apparent that the first inversion already removes most of the artificial error introduced into the modified wave spectra, but the error is suppressed still further in the subsequent iteration of the input spectrum. Table 3 summarizes the impact of the retrieval on characteristic wave parameters of the four spectra. In all four cases the significant wave heights retrieved from ERS-1 SWM data using modified WAM fg spectra H_s (modified (mod), retrievals (re)) agree closely to those H_s (unmodified (orig), re) retrieved using the original WAM fg spectra. The azimuthal cutoff wavelengths $\lambda_{az}(\cdots, \text{re})$ could be reliably adjusted to the observed (obs) values $\lambda_{az}(\text{obs})$. Plates 1a–1d clearly illustrate the relationship between the cutoff length scale and the high-frequency energy
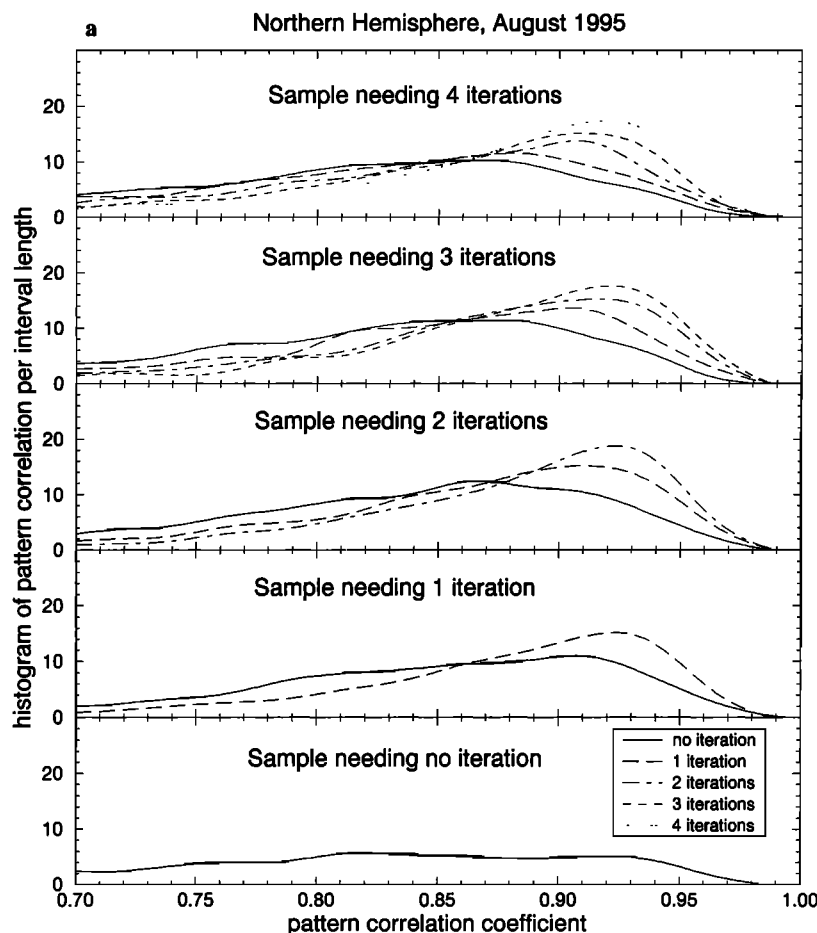
Figure 6. Distribution of pattern correlation in the (a) northern hemisphere and (b) southern hemisphere. The data sets of each panel consist of all spectra for which exactly N iterations produced the optimal retrieval (see Table 1). The curves within each panel indicate the improvement in pattern correlation with increasing number of iterations.

content (see, e.g., the SAR spectrum simulated from the modified input spectrum in Plates 1a and 1d). While for the original WAM fg spectra less than five iterations were often sufficient to find the best estimate, the modified WAM fg spectra required all five iterations to adjust to the best solutions. Table 3 shows that the initial errors $\varepsilon(\cdots, fg)$ between the observed and simulated SAR spectrum are reduced considerably through the retrieval process.

To assess the sensitivity of the retrieval for a larger ensemble of cases, we have repeated the retrieval using WAM fg spectra similarly increased by a factor of 4 for a 1-day set of some 1100 ERS-1 SWM spectra on June 7, 1995. For the analysis we have considered only retrievals for which both the original and the modified retrievals yielded an acceptable fidelity level, corresponding to a normalized SAR spectral error $\varepsilon < 0.3$. As can be expected, this eliminated some of the cases that passed the quality test for the original spectra but not for the modified spectra.

Figure 8 shows the regression between the significant wave heights retrieved using the original and modified WAM fg input spectra. The regression coefficient is 1.15. Thus the retrieval reduced the relative error of the modified fg wave heights on average by a factor of 6, from 1 to 0.15. The error would have been reduced still further if more iterations of the input spectrum had been carried out. However, typical errors

of the first-guess wave fields are significantly smaller than the synthetic errors considered here, so that five iterations are normally quite adequate (see section 3.2).

4. Statistical Intercomparisons

Global and regional intercomparisons between the collocated spectral wave parameters retrieved from ERS-1 SWM spectra and computed with the WAM model were carried out for the 3-year period January 1, 1993, to December 31, 1995. The collocation was performed using the nearest model grid point and nearest 6-hour model synoptic time to the observation location and time.

In a first analysis the data were divided into eight ocean basin regions, namely, the North, tropical, and South Pacific; the North, tropical, and South Atlantic; and the tropical and South Indian Ocean, with tropical boundaries at 25°N–25°S. Linear regressions were performed of the collocated data for monthly, seasonal, and the full-period data sets (see appendix, section A3). Figure 9 shows as an example the seasonal regression between WAM model and SWM-retrieved H_s values in the northern hemisphere extratropics, the tropics, and the southern hemisphere extratropics for the northern hemisphere winter December, January, and February (DJF) 1993–1994.
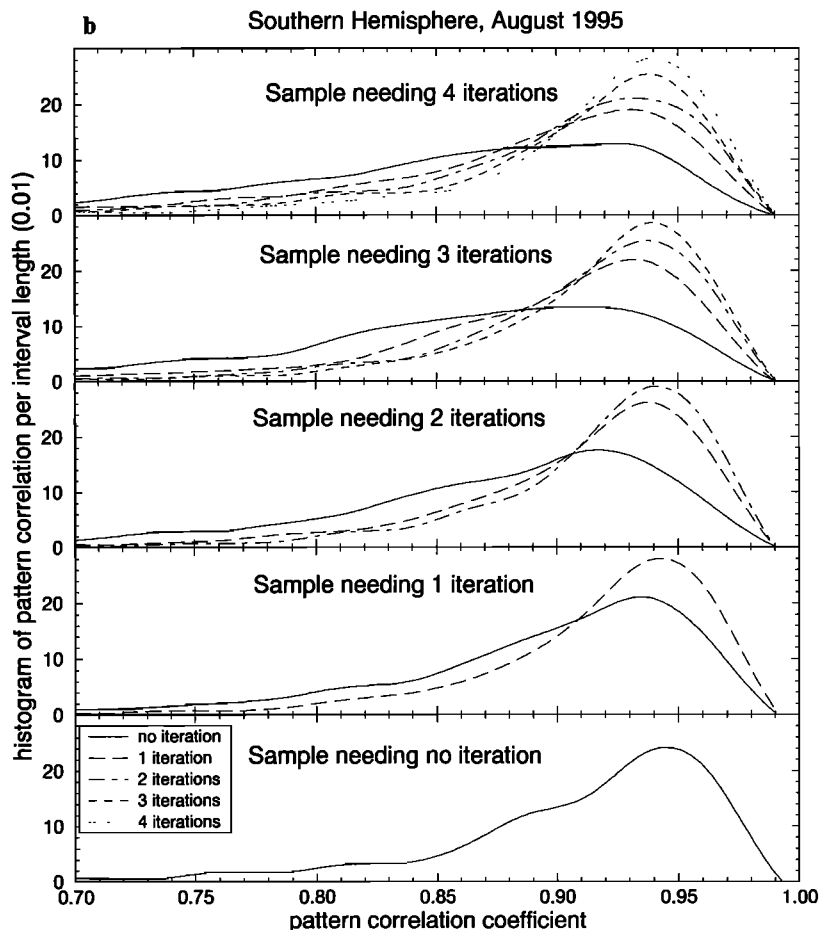
Figure 6. (continued)

4.1. Comparison of Integral Properties

4.1.1. Monthly mean H_s. Figure 10 compares the time series of monthly mean significant wave height in different regions of the Atlantic, Pacific, and Indian Ocean retrieved from ERS-1 SWM (dashed line) and computed by the WAM model (dotted line). The overall agreement is satisfactory. There is a more pronounced annual cycle in the northern hemisphere than in the southern hemisphere, the summer wave heights decreasing more strongly to about 1.5 m in the north as compared to 2.5 m in the south. This reflects the higher abundance of low-pressure wind systems that still prevail in the southern midlatitude zonal belt during the summer season. In the northern hemisphere the monthly mean H_s values are higher (by about 10%) in the Atlantic than in the Pacific, while the opposite holds for the southern hemisphere (20% higher values in the Pacific than in the Atlantic). The maxima of the South Atlantic winter are also less strongly pronounced than in the other southern and northern basins for the winter seasons. The tropical Atlantic and Pacific show essentially no annual cycle, with monthly mean H_s values fluctuating about 2 m in the tropical Pacific and 1.75 m in the tropical Atlantic. In contrast, the tropical Indian Ocean exhibits a marked seasonal cycle reflecting the monsoons. Pronounced maxima comparable to those in the North Atlantic (although somewhat broader) are found also in the Southern Indian Ocean.

4.1.2. Bias. Despite the satisfactory overall agreement between modeled and retrieved wave heights, a small but systematic underestimation of H_s by the WAM model relative to the ERS-1 SWM data is seen in Figure 11 (solid line). The bias is more pronounced for low sea state summer conditions. A different behavior for different ocean basins is again apparent. In the northern hemisphere the negative bias shows a pronounced seasonal cycle, with larger values during summer (low sea states) than winter (high sea states). The bias in the tropical Pacific and Atlantic oceans also exhibits a weak seasonal cycle that follows the northern hemisphere, in contrast with the bias of the tropical Indian Ocean, which follows the Southern Indian Ocean. The southern hemisphere basins, finally, exhibit an approximately constant negative bias without a significant seasonal modulation.

4.1.3. Regression line slope. In addition to the bias a second useful parameter characterizing the statistical relation between modeled and retrieved wave heights is the slope b of the regression line (we have defined the regression line here as passing through the zero point of the axes, for details see appendix, section A3). Figure 12 (solid line) shows time series of b for the monthly data sets. Values greater (smaller) than 1 represent under(over)-estimated model values compared to observation. The time series for b are seen to follow the behavior of the bias, as expected.
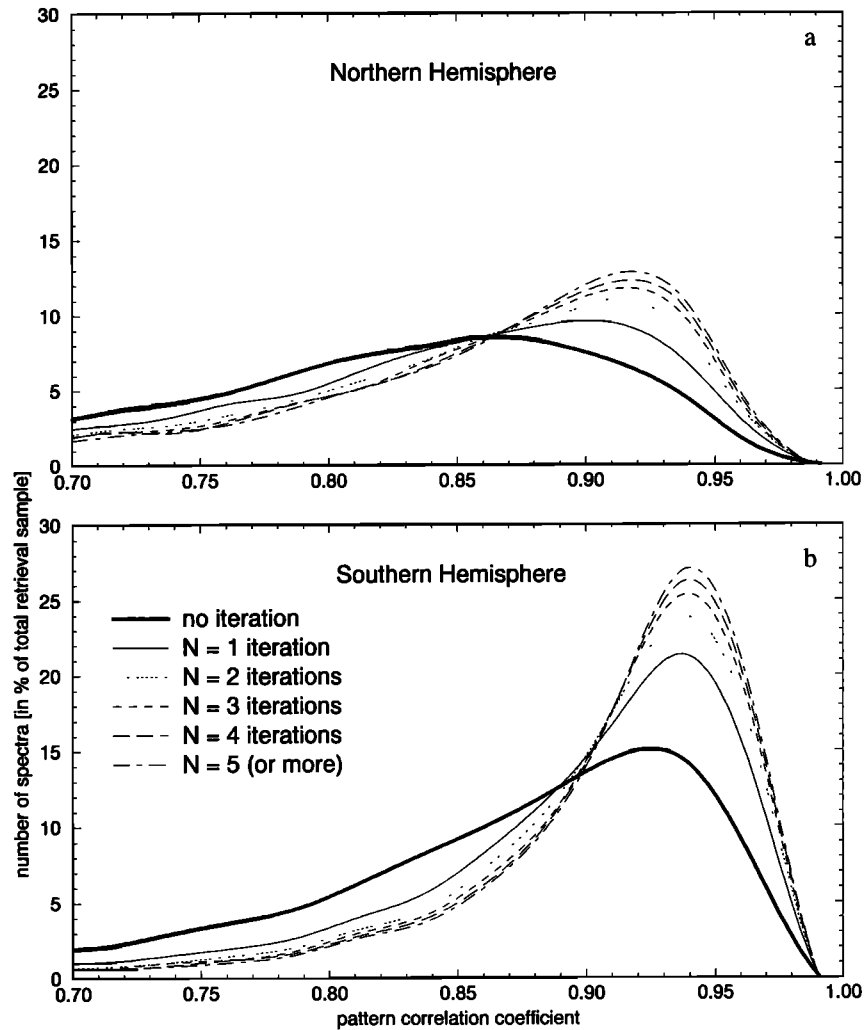
Figure 7. Distribution of pattern correlation in the (a) northern hemisphere and (b) southern hemisphere. In contrast to Figure 6, each panel is based on the same set. The data set is subjected to a series of retrieval runs, each retrieval differing in the prescribed maximum number of iterations allowed. The retrieval fidelity increases with increasing maximum permitted number of iterations.

4.1.4. Correlation. Time series of monthly correlation coefficients obtained from the regression are shown in Figure 13 (solid line). In the extratropical northern and southern hemisphere, fairly constant values of the order of 0.8 are found, except for a weak seasonal cycle in the North Pacific, with minima corresponding to low northern hemisphere summer sea states. The tropical Atlantic and Pacific exhibit somewhat lower correlation levels between 0.5 and 0.7. Winds in the tropics are generally low, so that the wave spectra are dominated by swell (see section 4.2). This suggests that the degree of agreement between model and observation is generally higher for locally generated wind seas than for swell that has traveled to the observation location from distant sources. This interpretation will be supported later in section 4.2 by the correlation time series of partitioned wind-sea and swell systems.

4.2. Comparison of Spectral Partitionings

A more detailed intercomparison of modeled and retrieved wave spectra can be obtained by partitioning the spectra into wave systems (compare section 2.2.2; for details of the partitioning system, the method for cross-assigning individual wave systems of the collocated modeled and retrieved wave spectra, and the criteria applied in the discrimination between young and old wind sea, mixed wind sea–swell, and pure swell systems, we refer to HBHH). For the present analysis we have included in the wind-sea category young and old wind-sea systems (as defined by HBHH), while swell refers to "pure" swell. Mixed wind-sea–swell systems are not included in either category and are also not presented as a separate wave system

Table 2. Change in Mean Retrieved H_s and Regression Parameters With Increasing Number of Iterations for a 1-Month Global Sample of ERS-1 SWM Data

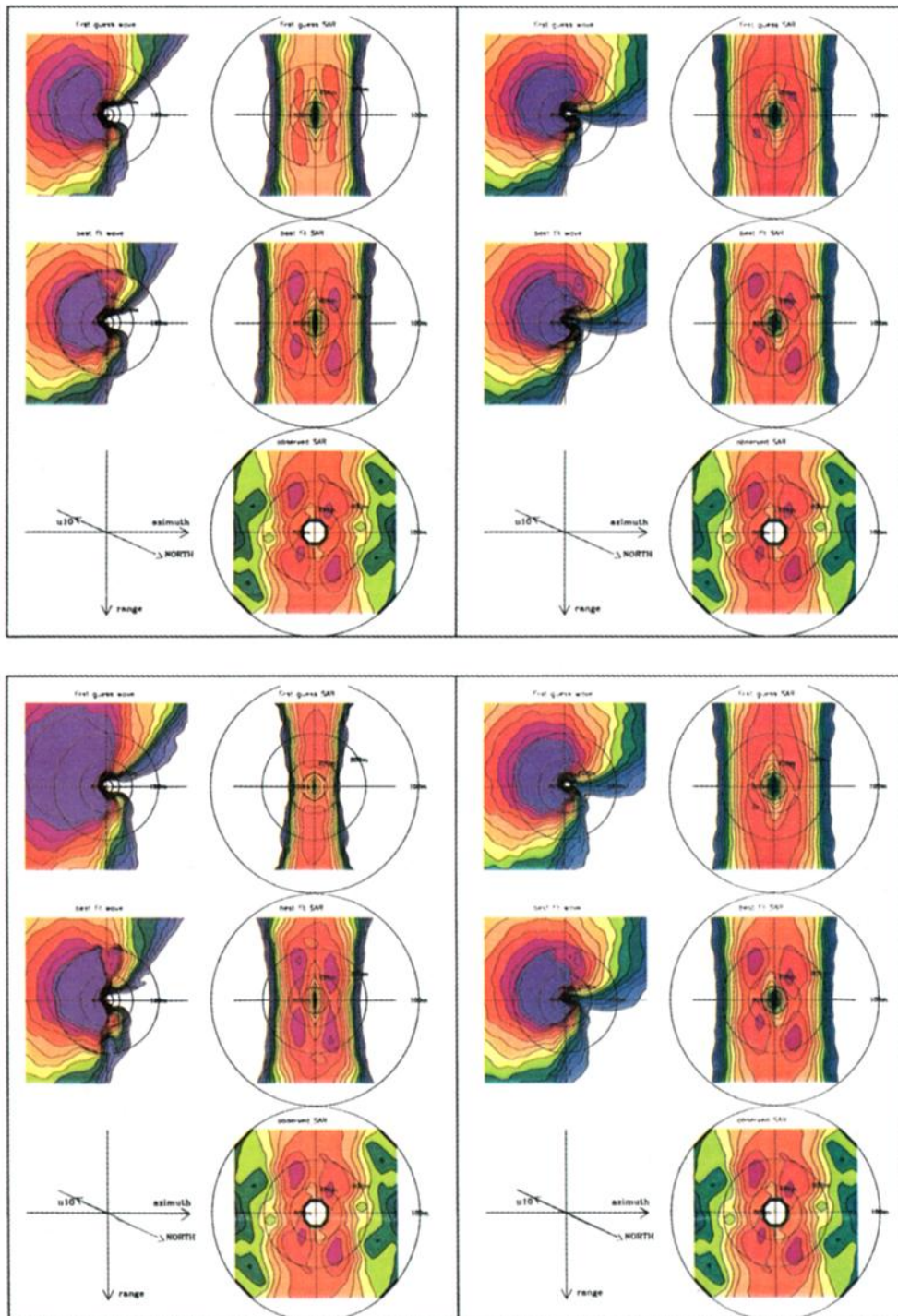|	Iteration					
	0	1	2	3	4	5
H_s, m	3.01	3.17	3.25	3.29	3.31	3.33
Slope	⋯	0.993	1.011	1.020	1.028	1.036
Correlation	⋯	0.942	0.897	0.874	0.859	0.846

There are 19,129 entries.

Plate 1a.   Input and retrieved wave spectra with associated SAR spectra for azimuthally traveling waves under strong winds. Top two quadrants show unmodified input spectrum; bottom two quadrants show input spectrum increased by a factor of 4. Left quadrants show straightforward inversion without iteration of the input spectrum; right quadrants show the best retrieval of five iterations of the input spectrum. First row in each quadrant shows the (left) input spectrum (in the case of the optimally iterated input spectrum this is identical to the retrieval) and (right) associated computed SAR spectrum; second row in each quadrant shows the inverted wave spectrum (prior to application of smoothing and interpolation by wave system partitioning) and associated computed SAR spectrum; bottom row, right side in each quadrant shows observed SAR spectrum.
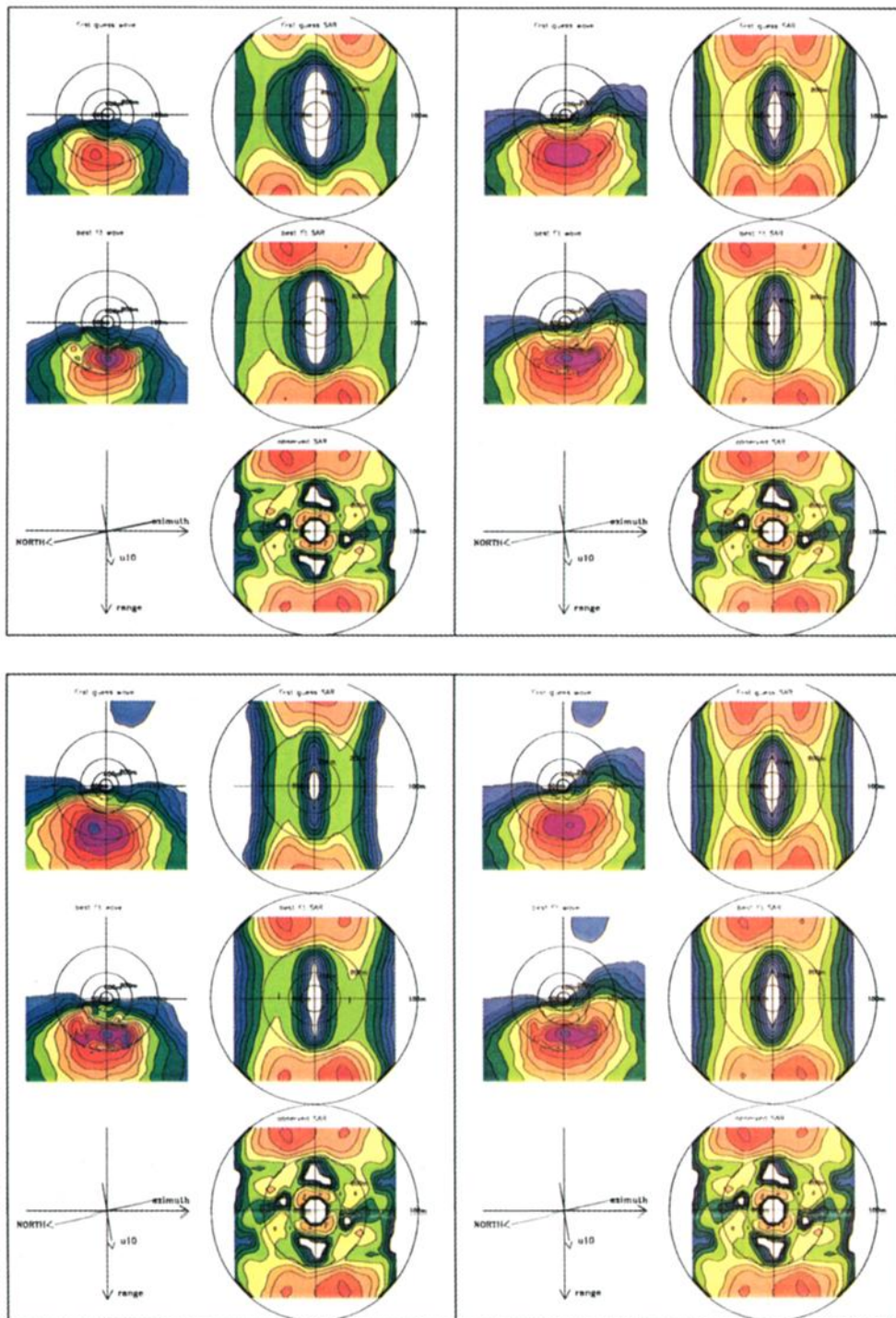
Plate 1b. Same as Plate 1a but for range traveling waves under light winds.

class since their contribute to the total wave energy is relatively small.

Plate 2 shows as an example the global distributions of the modeled and observed average number of swell systems per spectrum for the northern hemisphere winter DJF 1993–1994. The largest number of swell systems is found in the tropics, which receive swell from the midlatitude high wind regimes in both hemispheres as well as locally generated swell by the fluctuating trade winds. The ability of both the model and the SAR system to distinguish between a relatively large number of

different wave systems and the agreement between the simulated and observed distributions of this characteristic structural spectral parameter is encouraging.

The corresponding distributions for wind-sea systems are not shown. Theoretically, they should be nearly uniform at a value ≈1, since a wind sea is always present as soon as a light breeze occurs. However, for the operational WAM model, which was integrated with a resolution of 3° × 3° (later 1.5° × 1.5°), such light winds cases, as well as typical wind-sea situations with changing wind directions, yielded wave systems that
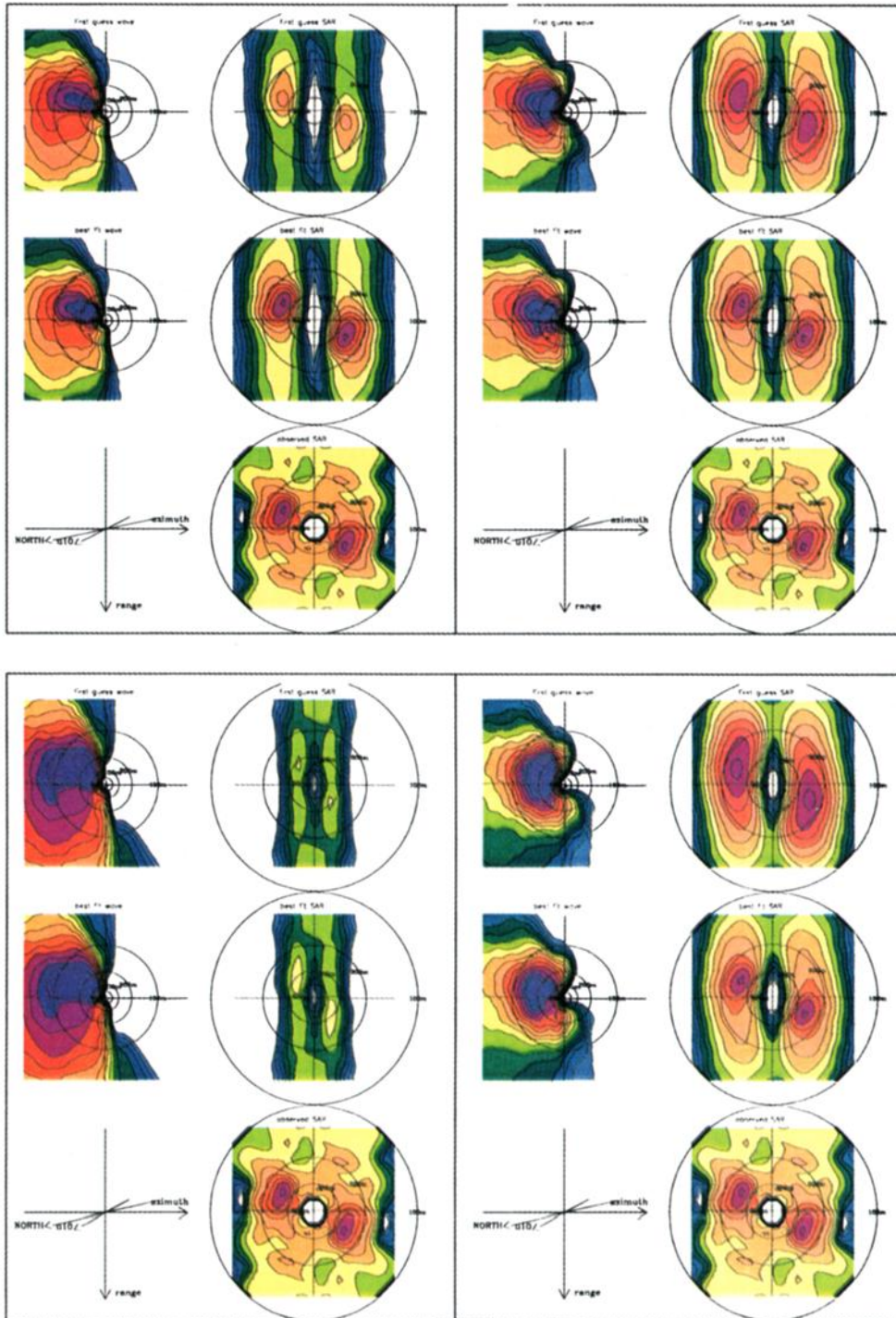
Plate 1c. Same as Plate 1a but for azimuthally traveling waves under light winds.

were normally classed as mixed wind-sea–swell systems rather than pure wind sea (compare HBHH). The SAR is similarly unable to detect or adequately resolve wind-sea systems for low to moderate wind speeds because of the azimuthal high wavenumber cutoff (although, as explained above, partially resolved wind seas are reconstructed in the retrieval system of HBHH using the information on the azimuthal cutoff in combination with the partitioning scheme incorporated in the iterative updating of the input spectrum). The data on wind-sea systems presented in the following refer therefore only to wind seas generated by fairly

large, moderate to strong wind fields that produce spectra satisfying the pure young or old wind-sea criteria of HBHH.

The time series of the monthly mean swell wave heights H_{sw} (defined as the significant wave height corresponding to the total swell energy summed over all swell systems) are shown in Figure 14 for the modeled (dashed lines) and retrieved (long-dashed lines) swell in different basins of the Atlantic, Pacific, and Indian Ocean. Also shown are the simulated and observed monthly mean wind-sea wave heights H_{ws} (dotted and dotted-dashed lines, respectively). The general agreement between
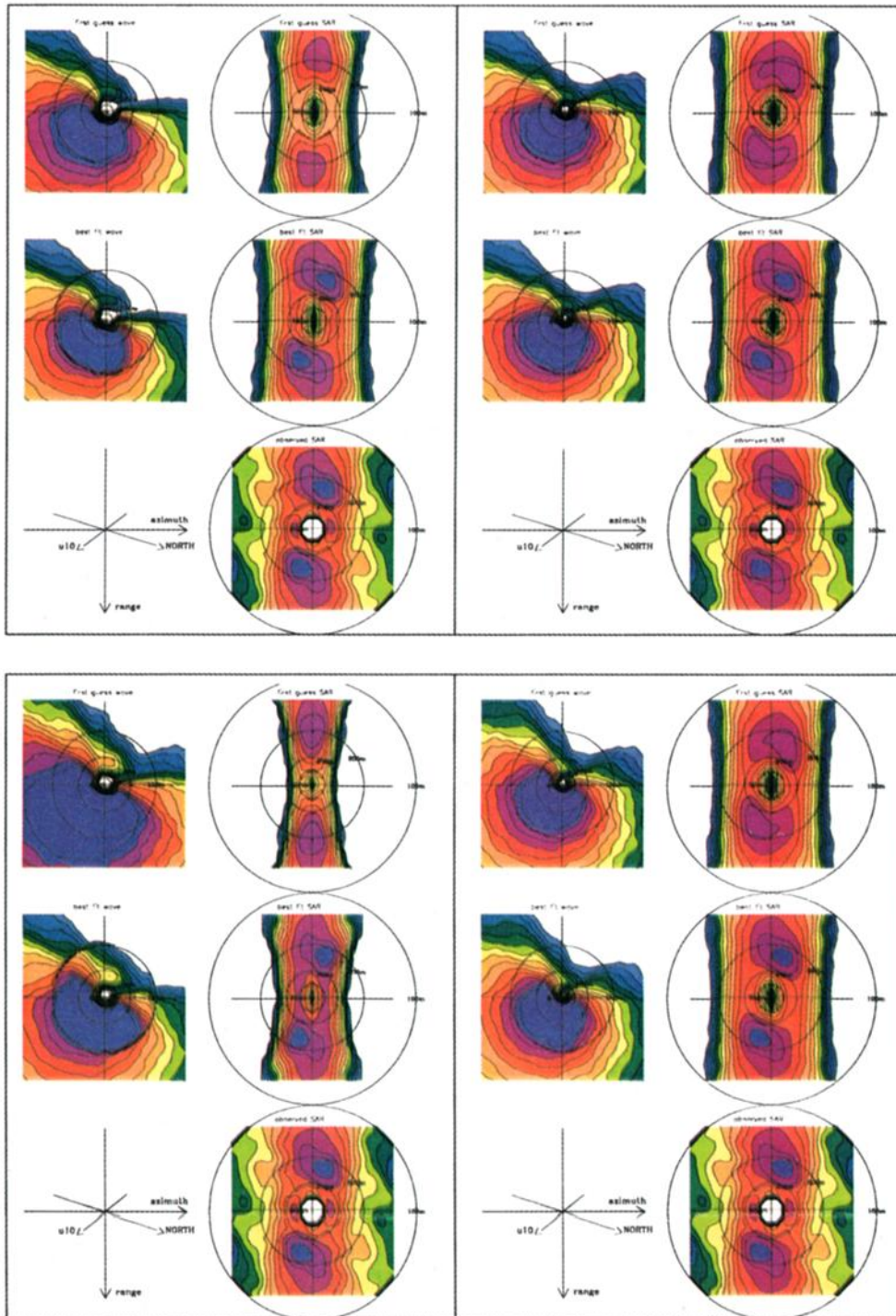
Plate 1d. Same as Plate 1a but for near-range traveling waves under strong winds.

model and observation and the distinctive annual cycles is again confirmed.

However, a discrimination is now possible with respect to the small systematic deviations noted earlier between the simulated and observed total wave heights. Whereas the WAM wind sea tends to be slightly overpredicted by about 10% relative to the retrieved data, with larger relative deviations for high sea states corresponding to winter conditions, the swell wave heights are systematically underestimated by about 20–30%.

The overestimation of wind sea is most pronounced for high

monthly mean H_{wi} during winter seasons, whereas the underestimation of swell, especially in the northern hemisphere, is seen most clearly for low swell, i.e., during summer. The biases for wind sea and swell in the northern hemisphere exhibit strong seasonal cycles, whereas in the southern hemisphere they remain fairly constant. We note that the swell biases exhibit a slight downward trend that is not present in the wind-sea biases. The time series of the slope of the monthly regression lines for wind sea and swell (Figure 12, dotted and dashed lines, respectively) follow the bias lines.

Table 3. Retrieval Impact on Characteristic Wave Parameters of Four ERS-1 SWM Spectra

	Spectrum Number			
	1	2	3	4
Date	June 2, 1995	June 6, 1995	June 7, 1995	June 8, 1995
Time, UTC	0128	1003	0726	1907
u_{10}, m/s	19.0	4.0	7.6	20.5
θ_{wind}, deg	180	272	345	126
ϕ_{az}, deg	10	99	3	126
H_s, m				
orig, re	5.3	1.7	2.3	5.5
mod, re	5.5	1.6	2.8	5.6
λ_{az}, m				
obs	259	191	181	239
orig, fg	266	185	188	259
orig, re	258	187	180	242
mod, fg	299	197	>400	309
mod, re	259	188	178	242
n_{iter}				
orig	5	5	3	2
mod	5	5	5	5
ε				
orig, fg	0.68	0.48	2.46	0.66
orig, re	0.10	0.09	0.17	0.08
mod, fg	0.77	0.41	6.55	0.52
mod, re	0.11	0.09	0.45	0.10

Retrievals (re); unmodified (orig) and modified (mod) WAM first-guess (fg) spectra.

As the magnitudes of the wind-sea and swell wave heights are of the same order, the different features of the wind-sea and swell biases cannot be explained simply by a dependence on wave height but must be attributed to the different spectral and dynamical properties of wind sea and swell. We have considered four possible causes for the differences.

1. The hydrodynamic transfer function occurring in the SAR mapping relation is poorly known. The present nonlinear forward mapping uses the theoretical modulation transfer function (MTF) proposed by *Feindt* [1985] without the wind dependent terms (see HH). Experiments with a wind dependent MTF showed little influence on the retrieval in the case of ERS-1 SWM spectra (W. R. Plant, private communication, 1995). This is to be expected for spaceborne SARs for which the velocity bunching mechanism is the dominant mapping contribution due to the high R/V ratio [see *Alpers et al.*, 1981, Figure 6; *Brüning*, 1994]. In the limited domain of linear mapping for range traveling waves, where the RAR MTF becomes important, it contains also a significant contribution from the geometrically well-defined tilt modulation MTF. Errors in the hydrodynamic MTF should appear as systematic errors in only a small subset of data representing range traveling waves, rather than in a difference between wind sea and swell distributed rather uniformly over all data. Thus the hypothesis of errors in the hydrodynamic MTF causing differences in the statistics of wind-sea and swell errors appears improbable.

2. Recent results from wave data assimilation exercises in which both the wave field and the generating wind field were updated suggest that in certain areas of the Atlantic and Pacific the ECMWF-analyzed wind fields produce too strong winds and thus too strong wind seas [see, e.g., *Bauer et al.*, 1996a, b; *Hasselmann et al.*, 1997; *Heimbach et al.*, 1996]. However, if this were the only error, an overestimation of the wind sea would necessarily lead also to an overestimation of the swell that

emerges from the storm region, which is not found. Another source of error must therefore be sought.

3. The combination of an overestimation of the wind sea together with an underestimation of swell suggests a possible error in the balance between wind-sea and swell dissipation. The balance could be modified to conform with the SAR data either by increasing the exponent characterizing the frequency dependence of the dissipation source function, which would decrease the ratio of swell to wind-sea dissipation, or by increasing the nonlinearity dependence, which would similarly result in a relatively weaker dissipation of long swell, which is characterized by smaller wave slopes.

4. The transition regime between wind sea and swell in the area close to but outside the immediate wind generation region, where the wind forcing has already decreased but the nonlinear interactions are still important, plays a critical role in determining the ratio of wind-sea to swell energy [see, e.g., *Snodgrass et al.*, 1966; *S. Hasselmann et al.*, 1985; *Young et al.*, 1987]. It is conceivable that the strongly simplified discrete interaction parametrization of the nonlinear energy transfer implemented in the WAM model is inadequate for a proper representation of this process. Deficiencies in the parametrization of the nonlinear energy transfer may thus be considered as another candidate for explaining the different biases.

We have also considered numerical errors associated with the first-order upwind propagation scheme employed in the WAM model. In developing the WAM model, two schemes where tested: a first-order upwind scheme and a second-order leapfrog scheme [*WAMDI Group*, 1988]. While the first-order scheme produced a higher numerical dispersion, a diffusion term had to be introduced in the second-order scheme to supress negative energies occurring in regions of high gradients, which resulted in a comparable effective diffusion. Because of the relatively small differences between the two schemes the simpler first-order scheme was chosen. A third-order scheme has also been proposed [*Tolman*, 1992, 1995]. However, numerical errors in the propagation scheme can be excluded in principle as the origin of the spatially and temporally averaged mean global bias in swell energy. Provided the propagation schemes satisfy the standard requirement of energy conservation, all schemes will necessarily yield the same globally averaged swell energy, even though they yield different spatial distributions for individual swell cases.

We regard the third candidate of a too strong damping for low-frequency swell as the most likely explanation for the negative swell bias. This is supported by a plot of the relative bias of the WAM wave heights relative to the SAR as a function of wave height for both wind sea and swell, shown in Figure 15 for the data sample June, July, and August (JJA) 1994. The wind-sea graphs show a fairly constant relative bias of 15–25% for wave heights $H_{wi} > 1$ m, except for a slight positive slope in the northern hemisphere. In contrast, all swell graphs exhibit a more or less pronounced change in relative bias from negative values at low H_{sw} (-35% in the North Pacific (NP), North Atlantic (NA), tropical Pacific (TP), and tropical Atlantic (TA) and -15% in the South Pacific (SP), South Atlantic (SA), South Indian (SI), and tropical Indian (TI)) to positive values at high H_{sw} (except in the SP, where a -10% bias remains).

This can be understood by the dependence of swell height on propagation distance. The farther a swell system has propagated, the lower its energy level due to geometrical dispersion (and, to a smaller extent, dissipation; compare *Snodgrass et al.* [1966]). At the same time, if the dissipation is too large, as
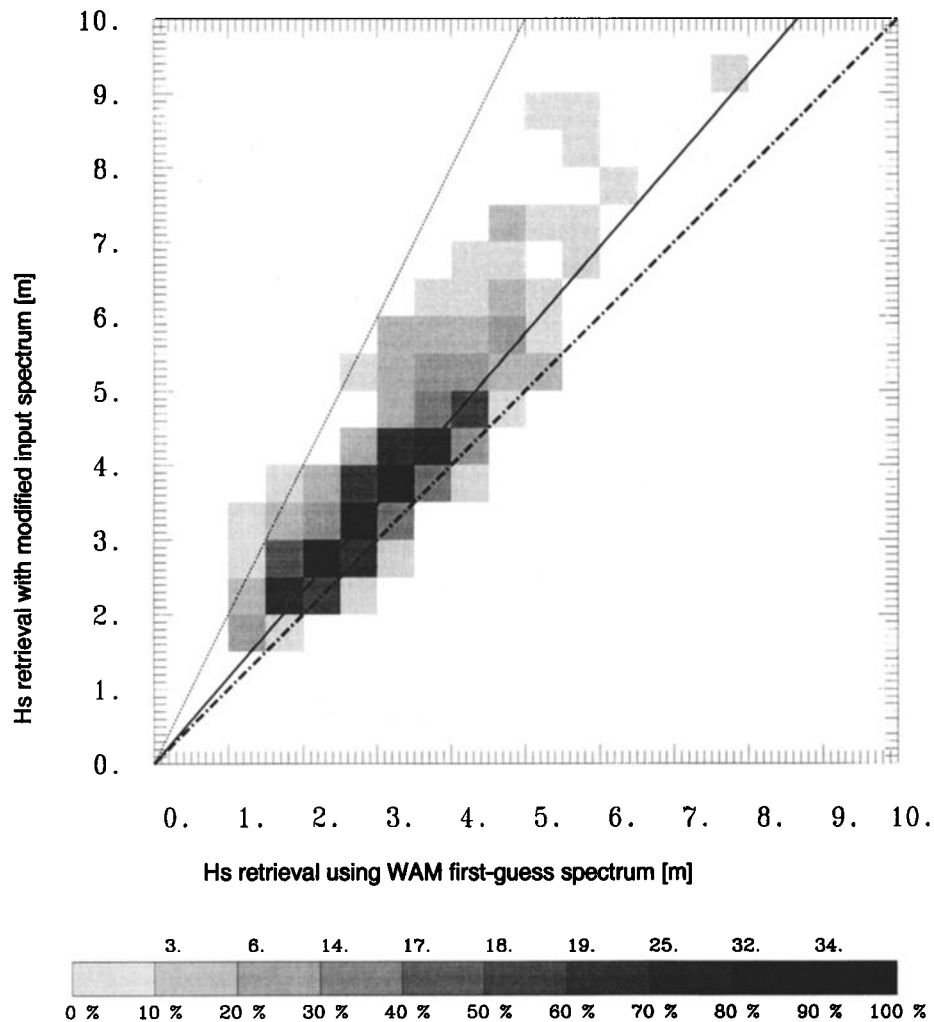
Figure 8. Regression between significant wave heights retrieved using the original and modified WAM first-guess input spectra for a 1-day set of ERS-1 SWM spectra on June 7, 1995.

hypothesized, the farther the swell has propagated, the larger the negative bias of the swell relative to the observations. Thus we should expect a direct correlation between the bias and the swell wave height, as seen in Figure 15.

The impact of the swell propagation distance on the bias could be demonstrated more directly if the swell propagation distance or, equivalently, swell age was computed by the WAM model. Unfortunately, this is not one of the output quantities of the standard WAM model. However, *Bauer et al.* [1996b] have developed a WAM model version for their Green function spectral data assimilation scheme which provides this information, and E. Bauer (personal communication, 1996) has kindly made available wave age data in the Atlantic for the period November 1992 with which we could test the assumed correlation between wave age and wave height. (The term wave age is meant here and in the following literally as the elapsed time since the waves last experienced a significant wind input, in contrast to the alternative usage of the term in wind-sea studies as the ratio of the phase velocity to the wind speed.) Figure 16 shows the average wave age over this period as a function of H_s for the North, tropical, and South Atlantic. The plots confirm that low H_s is associated on the average with high wave ages, especially in regions of low wind activity. Thus, in

the statistical average, it appears justified to regard the wave height in Figure 15 as a proxy for the wave age.

A remark needs to be made concerning the operational WAM model data. Since August 1993, ERS-1 altimeter wave height data have been assimilated by ECMWF into the WAM model using an optimal interpolation scheme, thereby influencing the first-guess wave field through the analysis 6 hours earlier. The swell wave field is thus continuously updated by the assimilation of new wave height data, thereby reducing the impact of systematic model errors in the propagation of swell over large distances.

However, an investigation of altimeter wave heights suggests that the impact on the first-guess data available for the present study is probably rather limited [see *Bauer and Staabs*, 1998; E. Bauer and P. Heimbach, manuscript in preparation, 1998]. First, no marked change in the monthly mean significant wave height time series can be seen for the northern hemisphere summer 1993 at the time when operational assimilation of altimeter H_s into the WAM model was introduced (Figure 10). Furthermore, the careful study by *Bauer and Staabs* [1998] revealed a systematic shift in the monthly mean wave height time series of the ERS-1 altimeter beginning in January 1994 relative to 1993 [see *Bauer and Staabs*, 1998, Figure 8], the
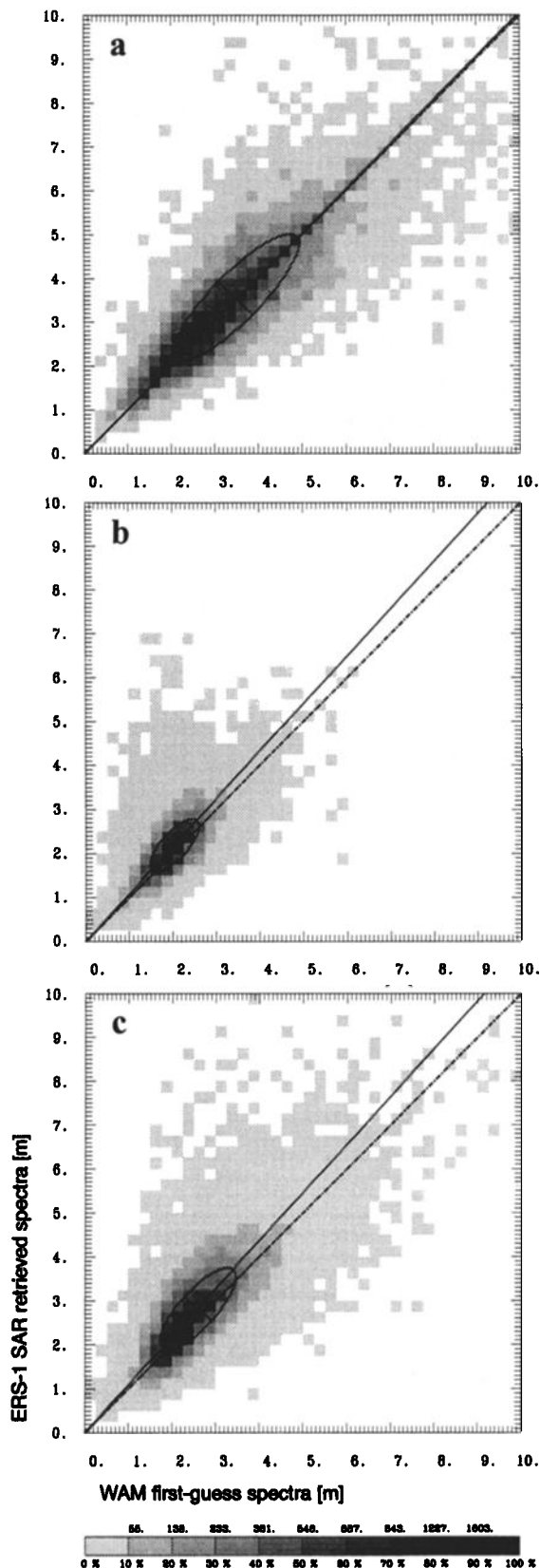
Figure 9. Comparison between ERS-1 SWM-retrieved and WAM model wave heights for DJF 1993–1994 in (a) the northern hemisphere extratropics, (b) the tropics (between 25°N and 25°S), and (c) the southern hemisphere extratropics. Solid lines represent the regression line and covariance ellipse; the dashed-dotted line represents the diagonal.

values for 1994 being reduced by as much as 0.6 m in the northern hemisphere extratropics and in the tropics. This results in a systematic shift in the bias between WAM and the ERS-1 altimeter wave heights in the transition from 1993 to 1994. If the assimilation of altimeter data had a significant impact on the first-guess data, a shift in the H_s time series for the WAM toward lower values should have been noticeable both in the summer of 1993, when the assimilation scheme was introduced, and at the end of 1993, when the ERS-1 altimeter algorithm was apparently modified. Although some indication of this effect may be apparent in the northern hemisphere extratropics, no influence is seen in the tropics, where the swell contribution is largest. We are therefore reasonably confident that although our model data are undoubtedly affected by the assimilation of altimeter data, the dynamical aspects we discuss later are still apparent in the data set.

A more quantitative analysis of the wind-sea and swell bias requires a regional and directional statification of the data, as discussed in section 4.4. A still more illuminating approach would probably be to study the propagation of individual wave systems, using the WAM model without data assimilation. However, this is beyond the scope of the present statistical analysis.

The time series of the correlation coefficient obtained from the regression analysis show another interesting difference between wind-sea and swell systems (Figure 13, dotted and dashed lines, respectively). Whereas the correlation for wind sea maintains a fairly constant high level of 0.9, the correlation for swell is lower and undergoes stronger variations between 0.6 and 0.8 in the northern hemisphere and in the tropics. Only the southern hemisphere exhibits a fairly constant correlation for swell of 0.8. This can be explained by the large and variable wave ages (propagation distances) of swell systems. Accepting the interpretation of the observed swell bias as resulting from an overestimation of the swell dissipation, the ratio of the predicted to measured swell energy will be a function of the propagation distance. The large range of propagation distances occurring in the ocean will therefore reduce the correlation between the modeled and observed swell wave heights and will lead also to variations in the correlation level depending on the season, i.e., the location of the storm areas.

4.3. Regional and Seasonal Intercomparison of Modeled and Retrieved Wind Sea and Swell

Further insight can be gained by looking at regionally stratified data as a function of season. To this end we have mapped all collocated WAM and SAR wave system data, subdivided again into wind sea and swell, for four consecutive seasons from winter (DJF) 1993–1994 until fall (September, October, and November (SON)) 1994 on a 5° × 5° global ocean grid. Plates 3a and 3b and Plates 4a and 4b show the distributions for the wind-sea and swell wave heights, respectively, while the associated "directional wave roses" representing the energy-weighted distributions of the wave propagation directions in the different ocean basins are reproduced in Figures 17a and 17b. The directional wave roses were computed as the square root of the mean energy for each 30° angular sector.

4.3.1. Wind-sea wave heights.
The wind-sea distributions (Plates 3a and 3b) reflect the seasonal properties of the atmospheric circulation [see, e.g., *Peixoto and Oort*, 1992]. In the northern and southern hemisphere extratropics the wind-sea wave heights are governed by the midlatitude westerlies. The regions of strongest wind-sea activity in DJF (northern hemi-
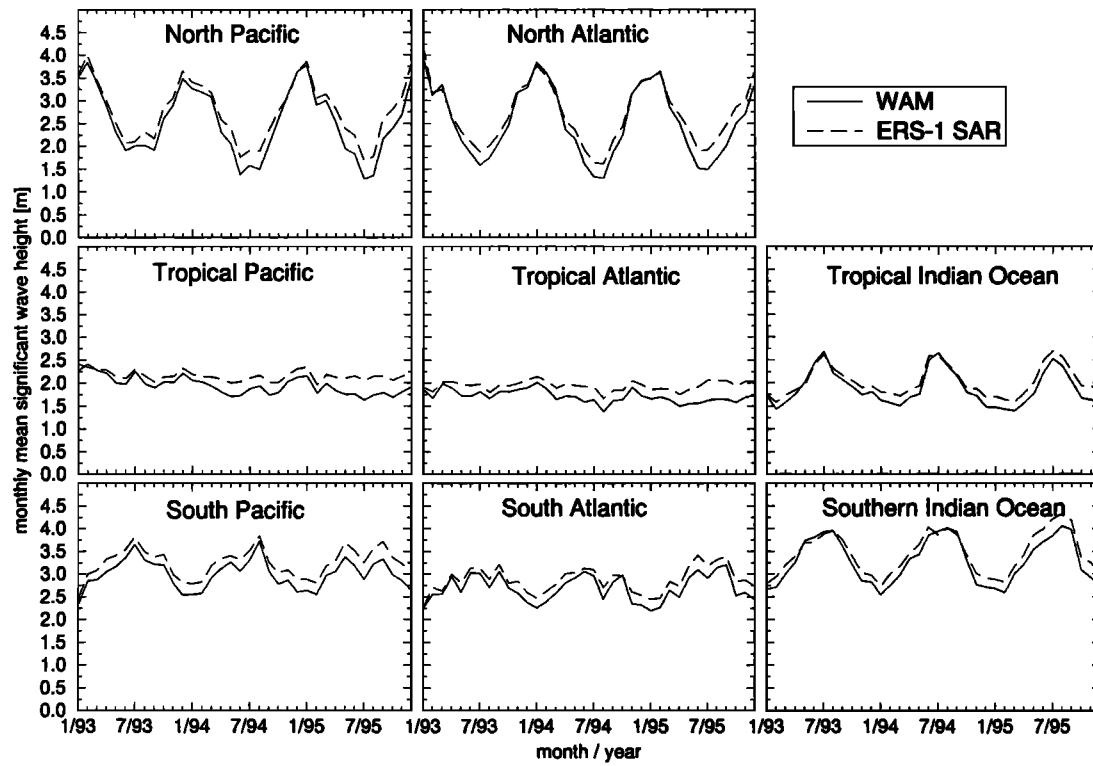
Figure 10. Time series of monthly mean significant wave heights between January 1993 and December 1995 for different ocean basins. Dotted lines refer to WAM model values, and dashed lines refer to ERS-1 SWM values.
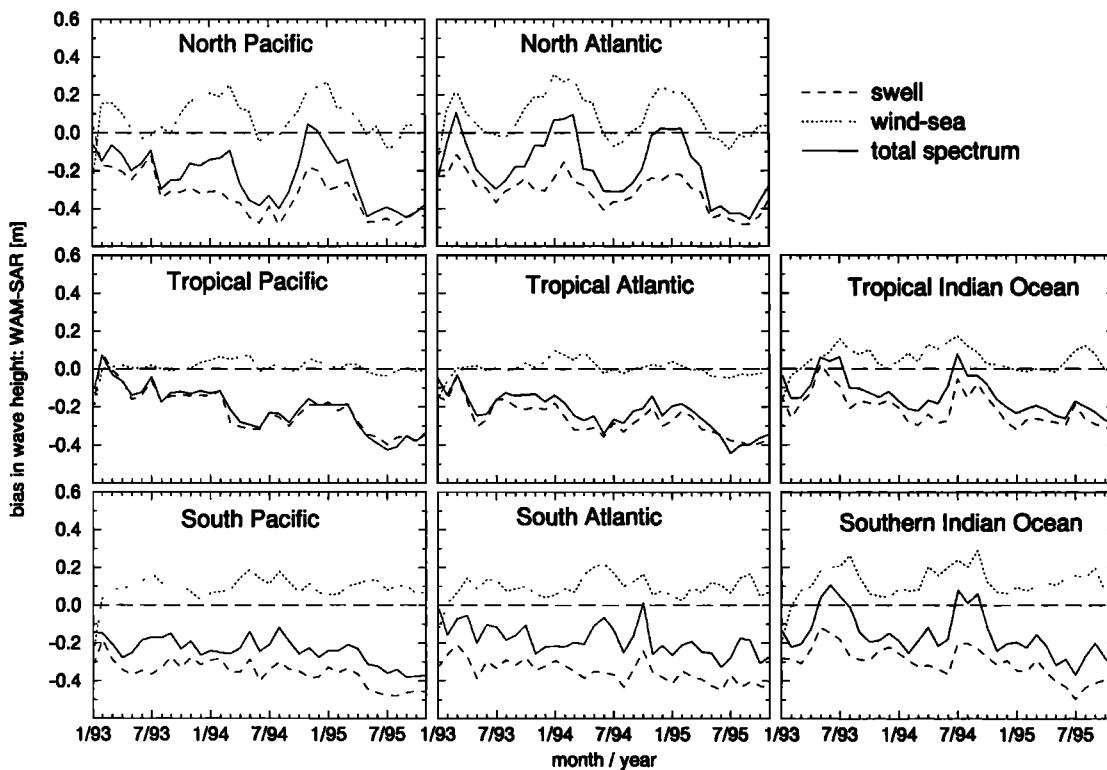

Figure 11. Same as Figure 10, but for the bias between monthly WAM model and ERS-1 SWM significant wave heights (solid line), wind-sea wave heights (dotted line), and swell wave heights (dashed line).
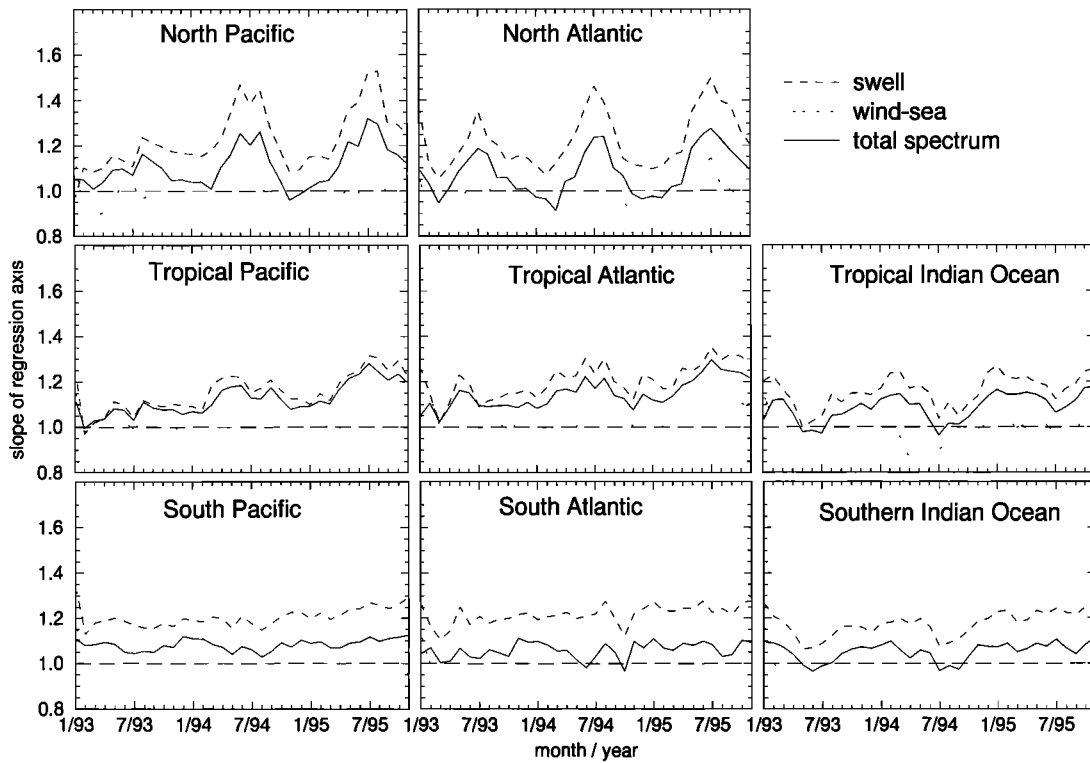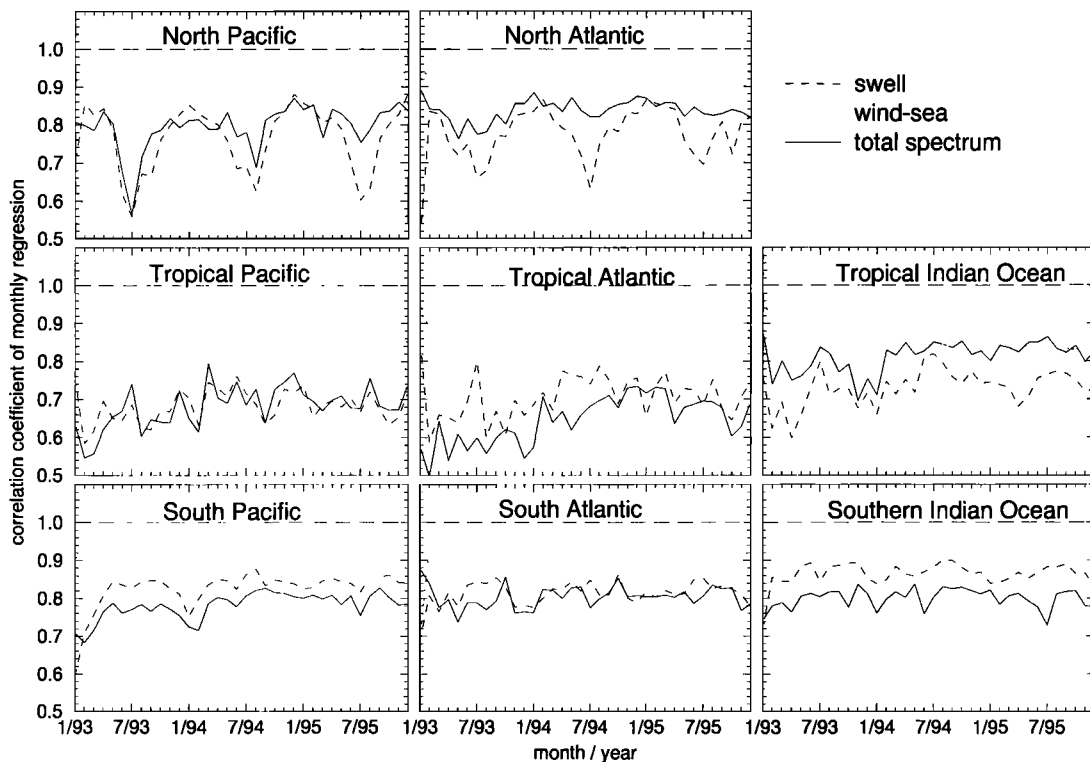
Figure 12. Same as Figure 10, but for the slope of the monthly regression between WAM model and ERS-1 SWM significant wave heights (solid line), wind-sea wave heights (dotted line), and swell wave heights (dashed line).

Figure 13. Same as Figure 10, but for the correlation of the monthly regression between WAM model and ERS-1 SWM significant wave heights (solid line), wind-sea wave heights (dotted line), and swell wave heights (dashed line).
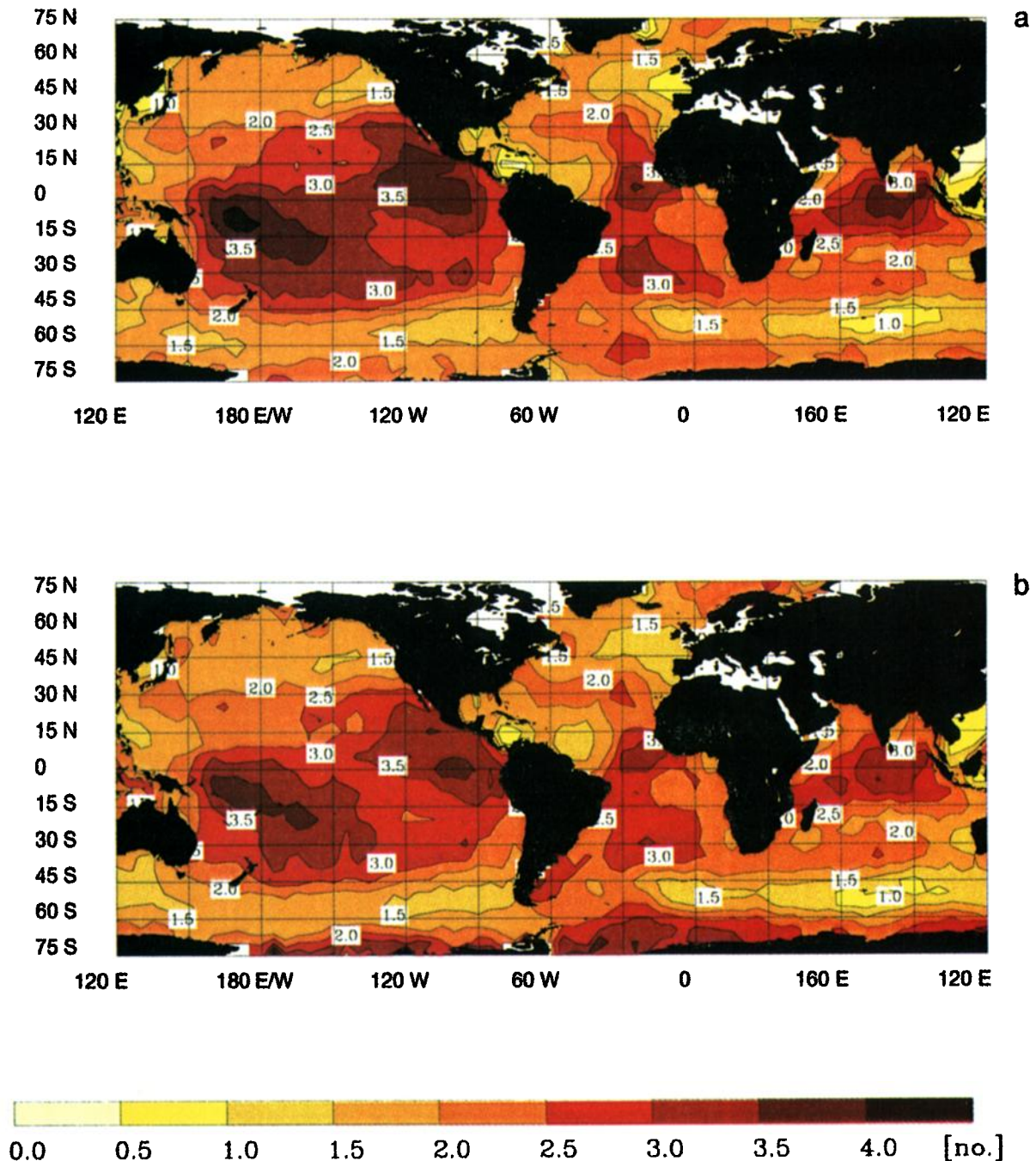
Plate 2. Global map of the average number of swell partitionings per spectrum for DJF 1993–1994. (a) WAM model; (b) ERS-1 SWM.

sphere winter) are found in the vicinity of the Aleutian low in the North Pacific and the Islandic low in the North Atlantic. A belt of moderate H_{ws} is found in the southern hemisphere midlatitudes, driven by the summer westerly wind belt around the Antarctic.

In the southern hemisphere winter JJA the highest wind seas are found in the midlatitude westerly wind belt in the southern hemisphere. Strong monsoon-driven wind-sea systems propagating to the NE and NW are found also in the Arabian Sea. In the tropics the dominant wave propagation direction is determined by the easterly trade winds, which are generally stronger in the winter seasons.

An alternative view of the global sea state structure is pro-

vided by the latitudinal distribution of the zonally averaged wave heights and directions for wind sea and swell (Figures 18a and 18b, respectively). The following features can be recognized: (1) low wave heights in the seasonally shifting equatorial Intertropical Convergence Zone (ITCZ) due to weak surface easterlies; (2) northwestward (in the southern hemisphere) to southwestward (in the northern hemisphere) propagating waves of moderate wave height in the trade wind regimes on either side of the ITCZ; (3) low wave heights in the region of the subtropical semipermanent high-pressure cells around 30°N to 30°S (the horse latitudes); (4) strong wind-sea systems in the midlatitude west wind belts, particularly in the roaring forties, fighting fifties, and screaming sixties in the winter
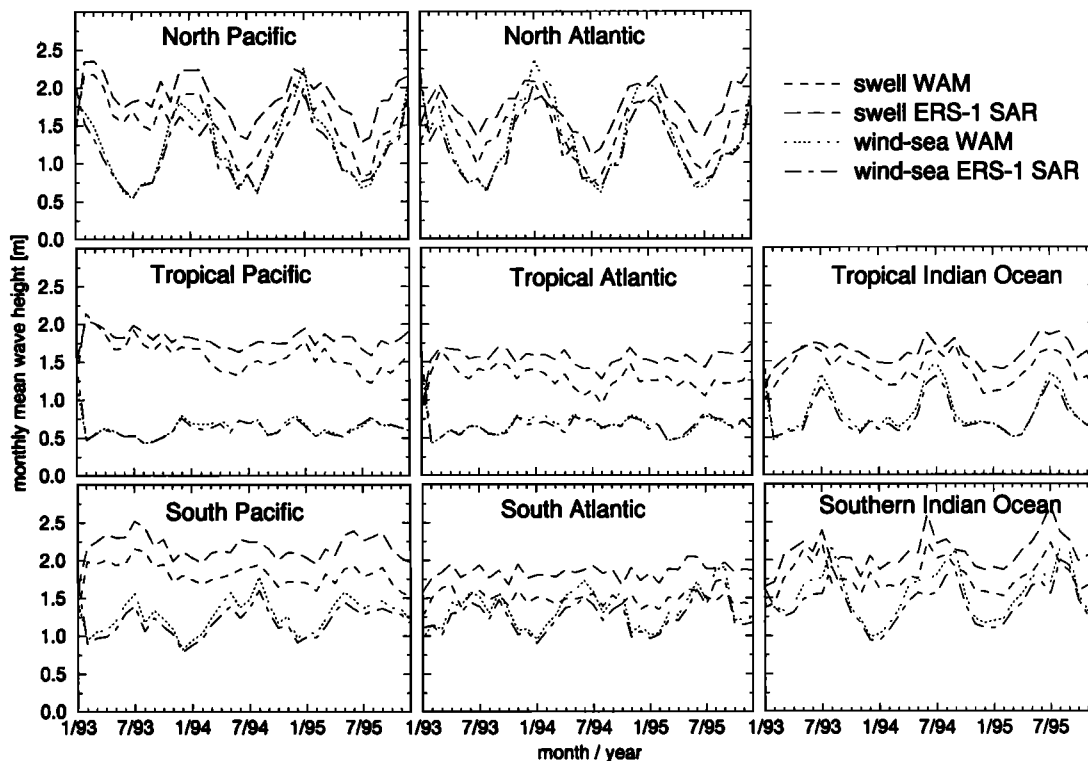
Figure 14. Same as Figure 10, but for the monthly mean wind-sea and swell wave heights.
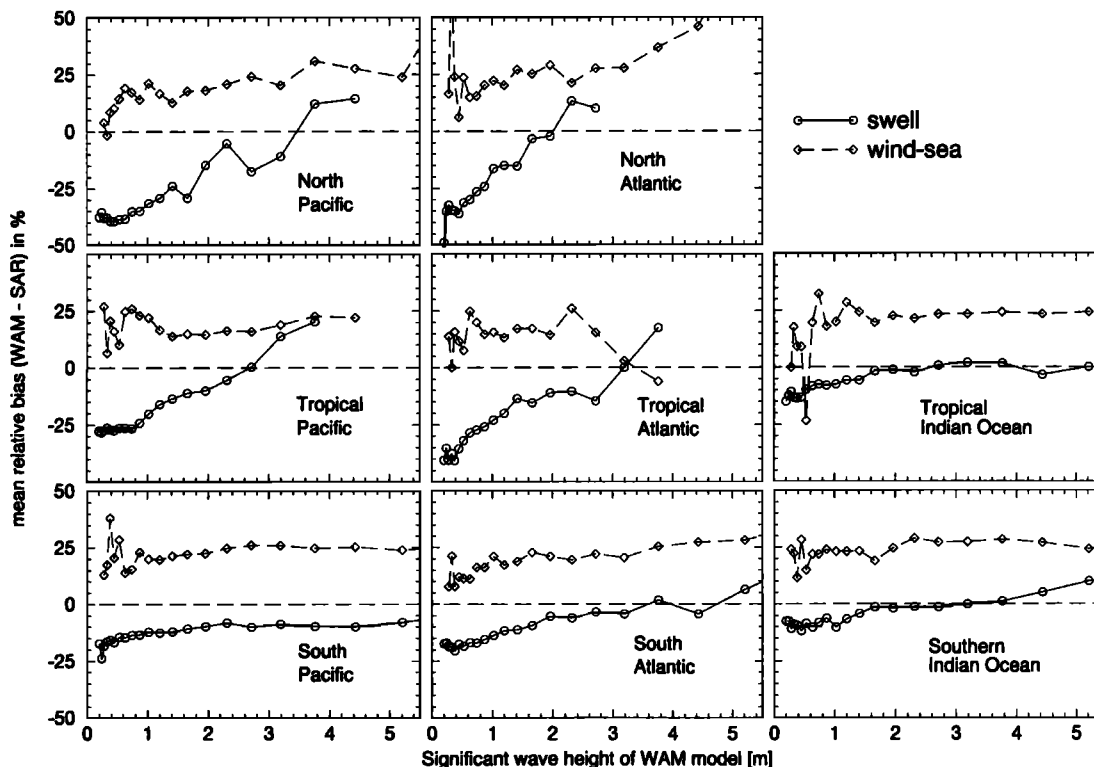

Figure 15. Mean relative bias between WAM and ERS-1 SWM as a function of the WAM model wave height for June, July, and August (JJA) 1994. Solid lines refer to swell, and dashed lines refer to wind sea.
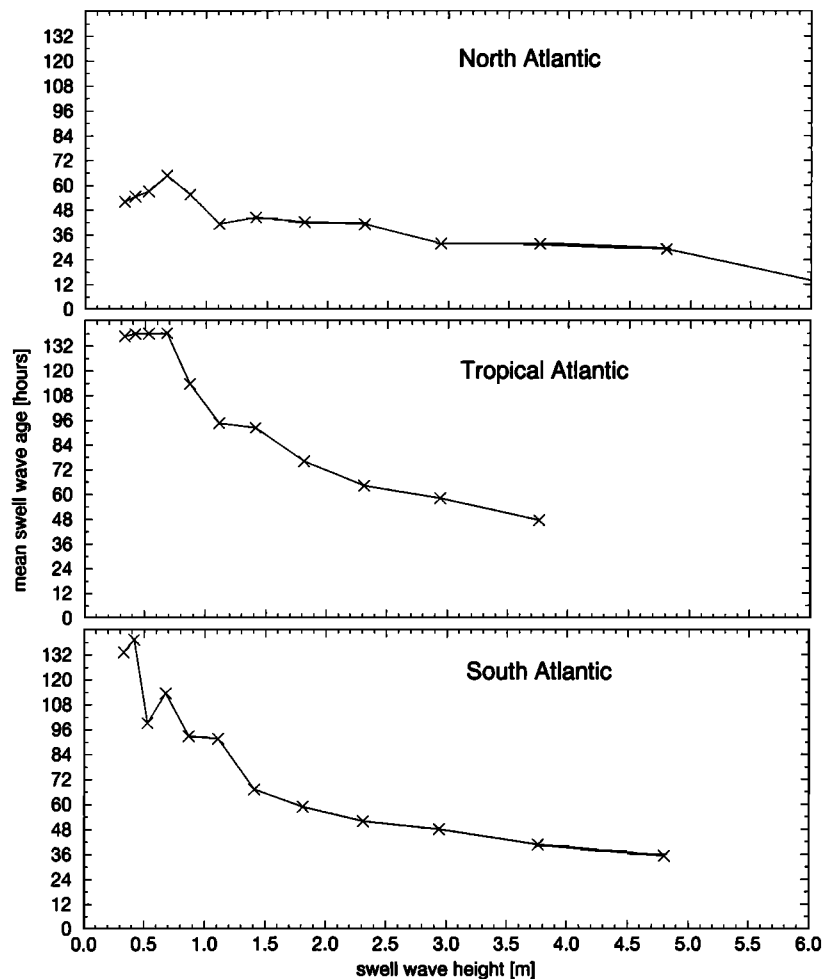
Figure 16. Average wave age as a function of the wave height of individual swell partitionings for a data set in the Atlantic for November 1992.

southern hemisphere; the stronger seasonal cycle in the northern hemisphere noted already in the H_{wi} time series is also seen; (5) the influence of the easterly winds from the polar high-pressure cells south of 65°S in the southern hemisphere; and (6) pronounced seasonal differences in zonally averaged swell wave height around 25°N in the Indian Ocean, caused by the seasonal monsoon cycle, and below 60°S near the Antarctic, presumably caused by changes in sea ice extent.

The seasonal maps and zonal averages of wave heights and directional distributions confirm the previous findings of a generally overestimated wind sea by the WAM model relative to the SWM retrievals. The effect is strongest in high sea states occurring in midlatitudes during winter. However, the modeled wind sea is slightly underestimated in the trade wind regions during JJA and SON.

The modeled and retrieved directional distributions in both Figures 17a and 17b and Figures 18a and 18b are remarkably similar. However, WAM shows a rather more symmetrical distribution of the meridional component about the west-east axis in the southern hemisphere extratropics, with a maximum directed to the east (90°), whereas the SWM retrieved data are more asymmetric with maxima directed toward ENE (60°). Discrepancies can also be seen in the directional distribution of east to northward traveling waves in the tropical Indian Ocean during the summer monsoon.

4.3.2. Swell wave heights. The seasonal maps of swell wave heights and directional distributions are less sensitive to local atmospheric conditions, but the principal features seen in Figures 18a–18b can again be largely attributed to the synoptic conditions that produced the wind sea that is later transformed into swell. Thus the predominance of eastward and equatorward propagating swell in the midlatitudes can be explained by the strong westerly cyclones in that belt. The significant meridional swell components in the tropics, characterized by a marked seasonal variation in the directional distribution, presumably also originate in the midlatitude cyclones. In addition, the tropical distributions exhibit a significant westward component due to the trade winds.

The previously noted underestimation of swell by the WAM model is again apparent, both from the directional distributions of Figure 17b and the zonal averages of Figures 18a–18b. In the extratropics the strongest bias is seen for eastward propagating swell; in the tropics it is seen for westward propagation. A more detailed analysis of the conditions for the South Pacific Ocean is given in section 4.4.

4.3.3. Mean wavelengths. In addition to the significant wave height and mean propagation direction, the third parameter normally used to charactize a wave spectrum or, in the case of a partitioned spectrum, a wave system is the energy-weighted mean frequency $\bar{f}$. Equivalently, we present in the
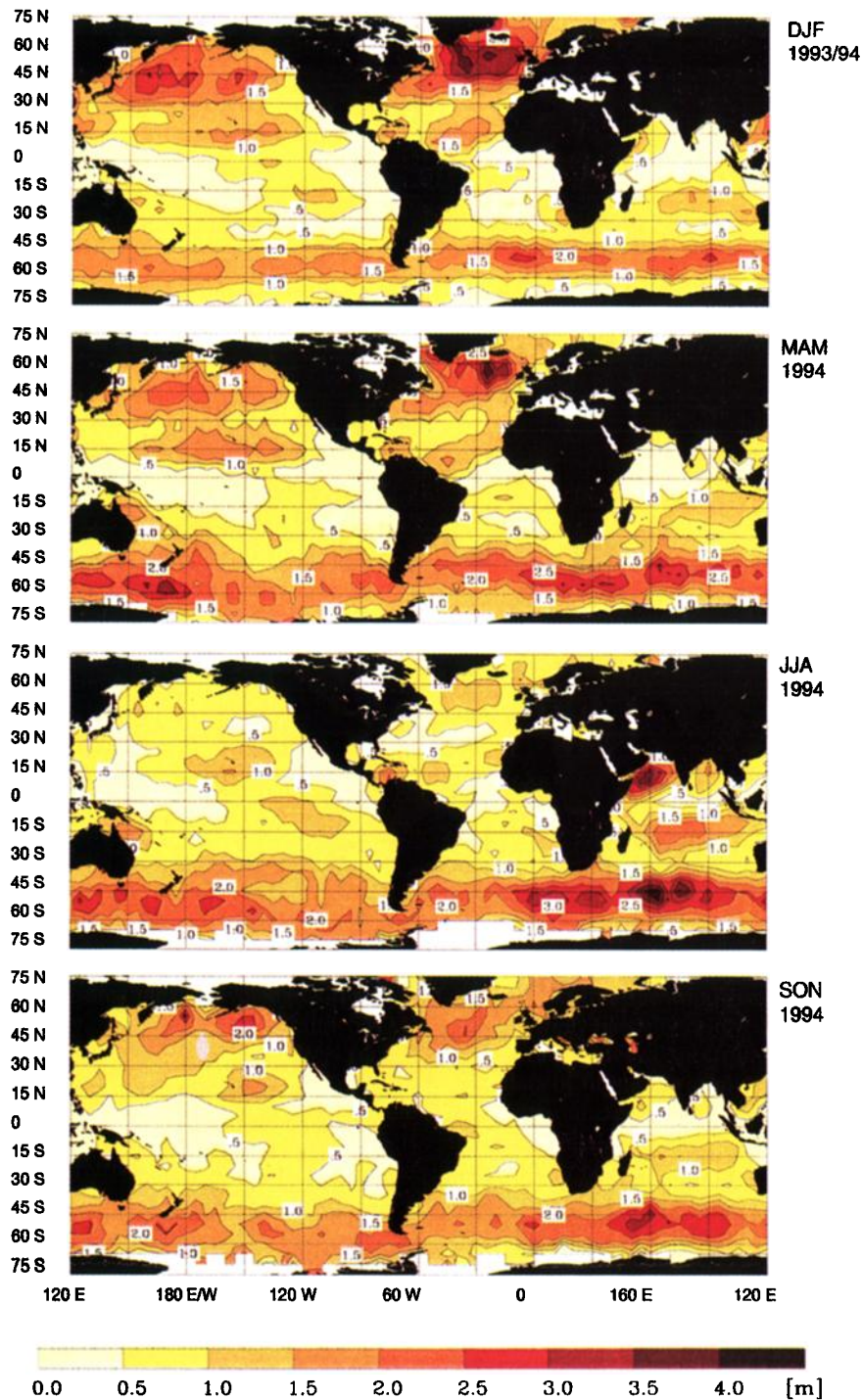
Plate 3a. Global maps of the seasonal mean wind-sea wave height for the four seasons (top two panels) DJF 1993–1994 to (bottom two panels) SON 1994 for the WAM model.

following the mean wavelength $\bar{\lambda} = g/2\pi\bar{f}^2$. Plates 5 and 6 show the distribution of seasonal mean wavelengths for wind sea and swell, respectively, for the modeled and SWM-retrieved spectra for the winter season DJF 1993–1994 (upper two panels) and summer season JJA 1994 (lower two panels).

The retrieved swell wavelengths agree rather closely with the modeled wavelengths but are generally slightly larger. This is consistent with the higher retrieved swell wave heights discussed in section 4.2. Too much significance should not be

attached to the retrieved wind-sea wavelengths. Because of the azimuthal cutoff the wind-sea part of the wave spectrum is normally only partially resolved by the SAR (compare section 5), the full wind-sea spectrum being reconstructed from the SAR data by fitting the azimuthal cutoff parameter and rescaling the parameters of the wind-sea wave system provided by the WAM model.

The effect of fetch be clearly seen in Plates 5 and 6. The shortest wavelengths are found in the lee of the continents, in
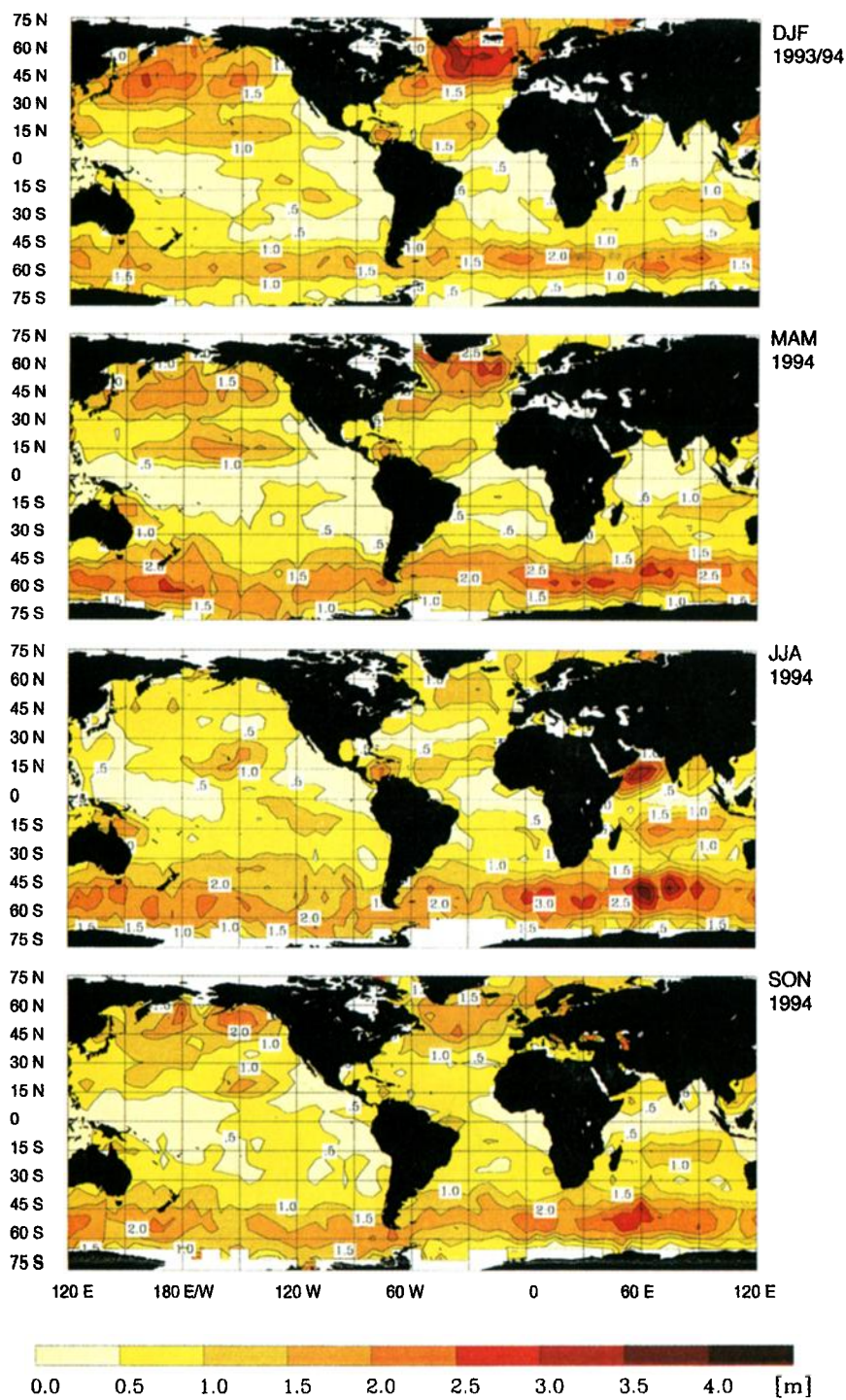
Plate 3b. Same as Plate 3a, but for the ERS-1 SWM.

midlatitudes off the east coasts, and the longest wavelengths are found in the eastern parts of the ocean basins and in the open Southern Ocean. The increase in wavelength with the higher wind speeds in winter is also clearly visible, particularly in the northern hemisphere, which has a more pronounced seasonal cycle (see section 4.1).

An interesting feature is the occurrence of long wavelength swell originating in the high-wind midlatitude regions in the eastern equatorial oceans; the swell wavelength isolines exhibit a distinct eastward-equatorward slant, corresponding to the main direction of propagation from the extratropics, in contrast to the predominantly east-west oriented isolines of the wind-sea wavelengths, corresponding to the mainly zonally directed winds.

The local impact of wind speed is seen most clearly, as expected, in the wind-sea wavelengths, which correlate well with the wind-sea wave heights, compare Plates 3a, 3b, and 5. However, for wind sea both the wind speed and the fetch are important, as demonstrated by the pronounced impact of both coastal shadowing and the high-wind regions on the wind-sea wavelength distributions.
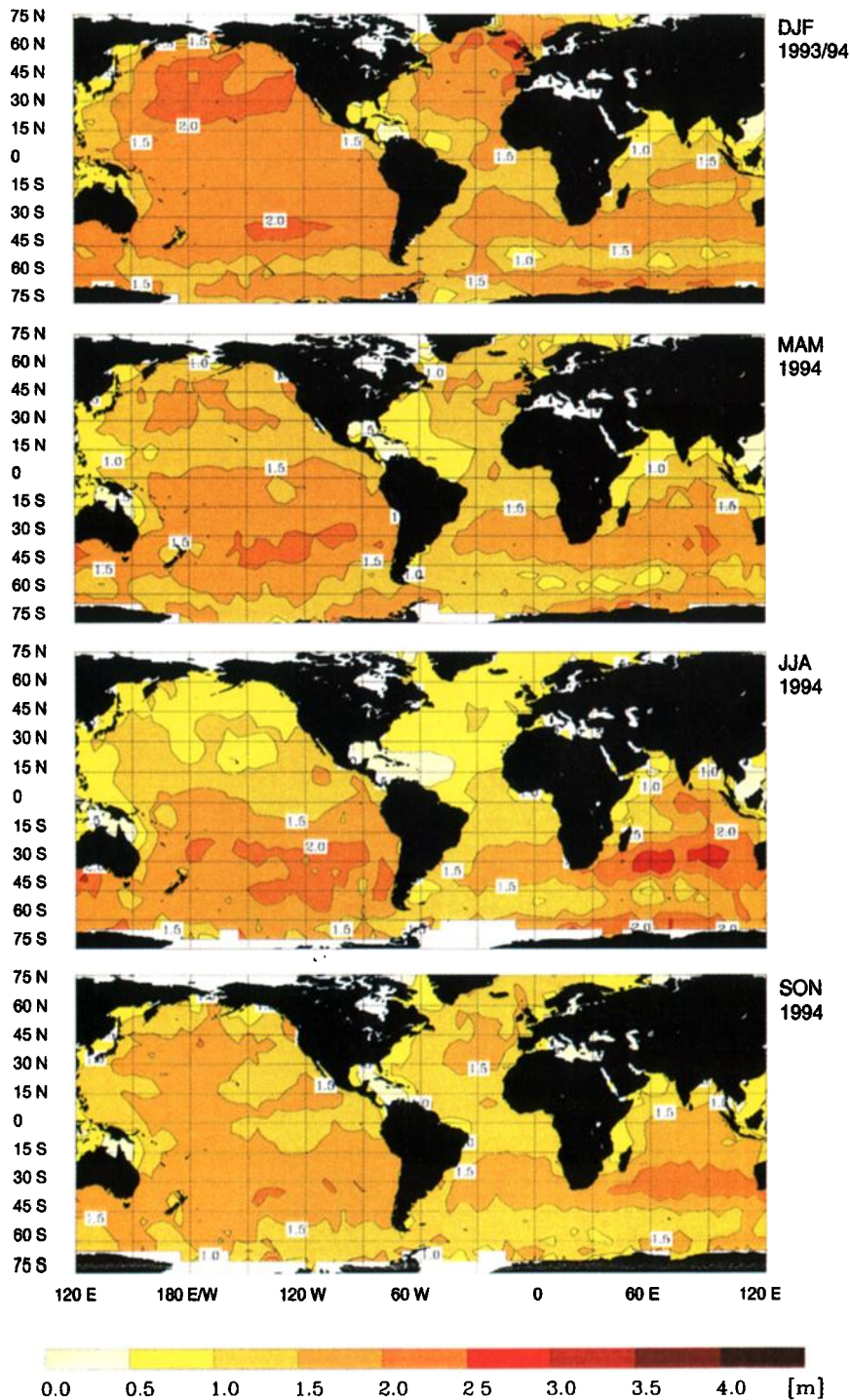
Plate 4a. Same as Plate 3a, but for the seasonal mean swell wave height.

4.4. Regional Analysis for the South Pacific Ocean

As an example illustrating the detailed spectral and regional information contained in the ERS-1 SWM data, we present in Figure 19 the retrieved and modeled wave roses for wind sea (Figures 19a and 19b, for DJF 1993–1994 and JJA 1994, respectively) and swell (Figures 19c and 19d, for DJF 1993–1994 and JJA 1994, respectively) for nine regions in the South Pacific.

4.4.1. Wind sea. The general zonal wind characteristics are reproduced by both the modeled and retrieved data, which show also significant deviations from the mean wind directions that appear as side lobes in the directional distributions. In the sample areas between 0° and 30°S the wind sea is dominated by west to northwest traveling waves generated by the trade winds. The WAM wind sea tends to be turned more equatorward than the retrieved wind sea, suggesting a possible shortcoming in the angular distribution of the ECMWF trade wind field.

Between 30° and 60°S the dominant wind-sea direction is eastward, reflecting the midlatitude westerlies. However, other
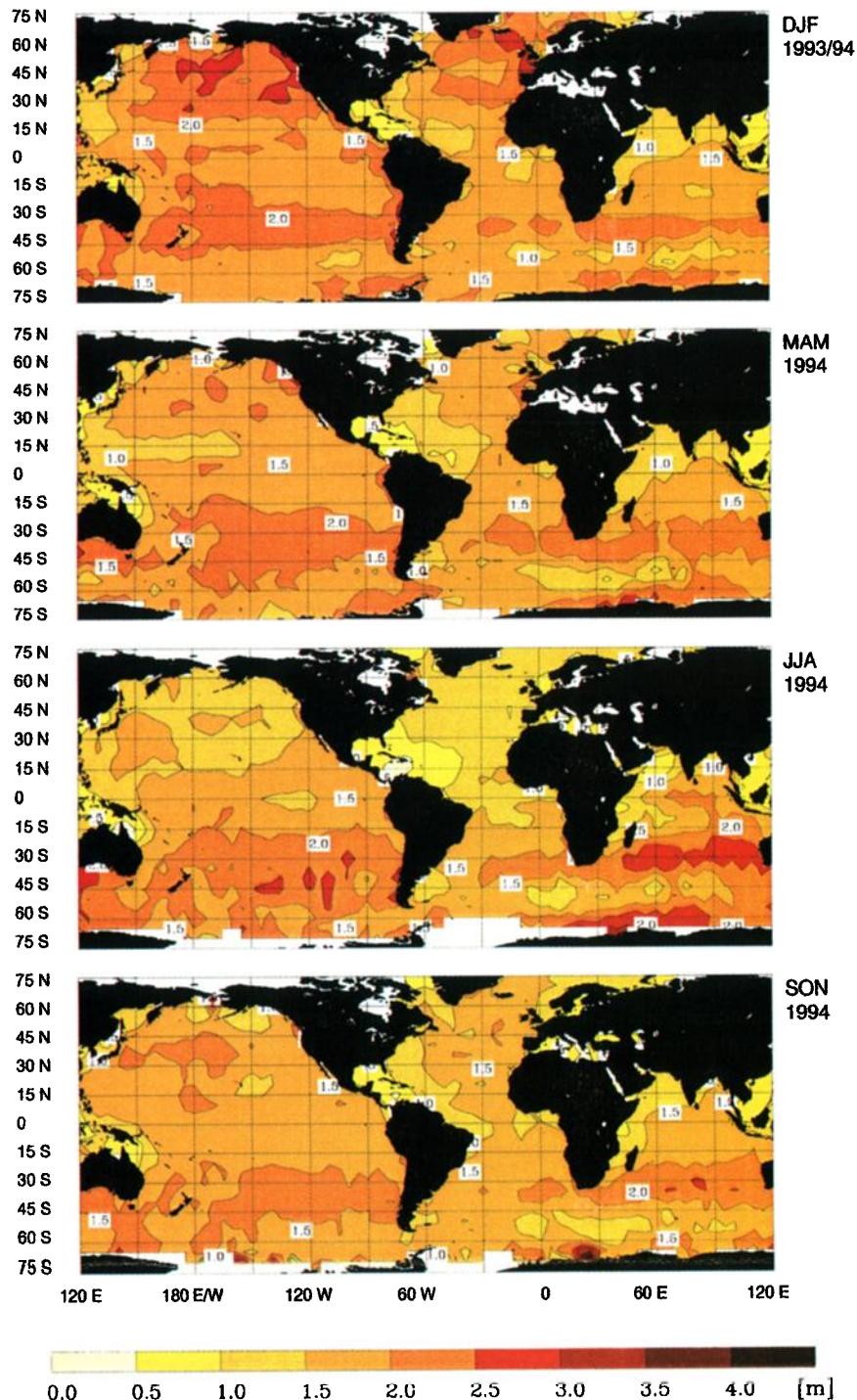
Plate 4b. Same as Plate 3b, but for the seasonal mean swell wave height.

directions also occur with significant probability, for example, toward the NW, as a result of the cyclonic disturbances characteristic of these latitudes. The WAM model overestimates mainly the east and southeast traveling components, suggesting again that the model errors must be attributed at least in part to wind field errors.

In the band south of 60°S the wind-sea distribution is similarly dominated by eastward traveling waves, and the WAM model again tends to overestimate waves traveling east to

southeast. The shadowing effect of Antarctica is clearly evident in the most westerly segment.

4.4.2. Swell. The directional distributions of swell in the tropical latitudinal band between 0° and 30°S are determined by two principal sources: the easterly trades on either side of the ITCZ, producing a broad westward propagating swell sector, and the midlatitude westerlies. The dependence on fetch leads to an increase of the trade wind swell from east to west, while the southeast traveling waves from the midlatitude west-
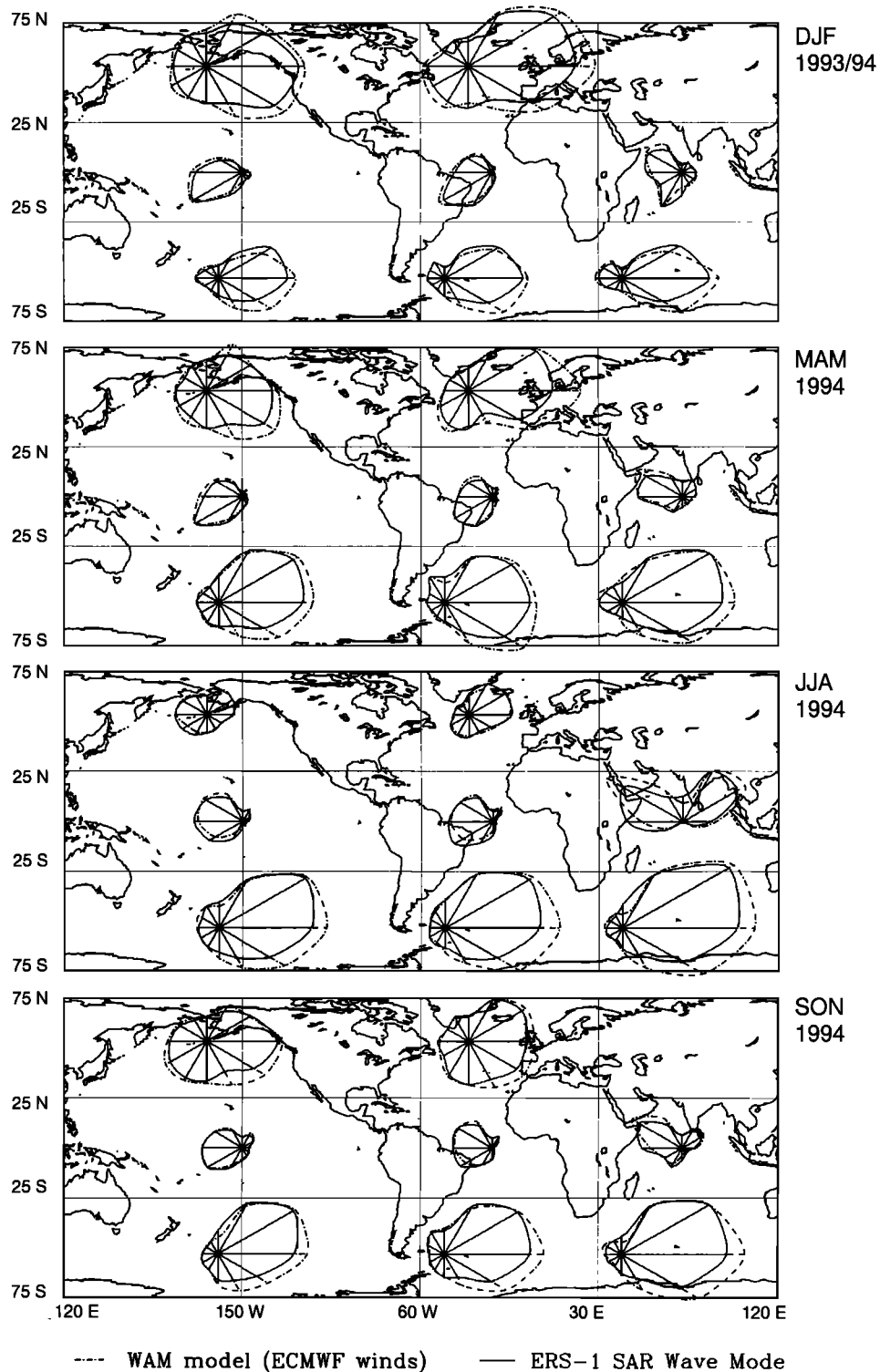
Figure 17a. Seasonal mean directional wave height distribution in different ocean basins for the four seasons (top) DJF 1993–1994 to (bottom) SON 1994. Dashed-dotted lines, modeled; solid lines, retrieved from ERS-1 SWM. For wind sea.

erlies to the south increase from west to east (see also the global distributions of wavelengths for JJA 1994, Plate 6). The WAM model tends to underestimate particularly the trade wind swell components.

In the remaining two latitudinal bands south of 30°S the swell is dominated by the midlatitude westerlies. The distribu-

tions become more isotropic, reflecting the cyclonic character of the generating storms. With a few exceptions, the WAM model underestimates the swell in all directions.

Particularly noticeable is the underestimation of the east and northeast traveling swell south of 60°S. This presumably again points to errors in the wind field. The area is bounded from the
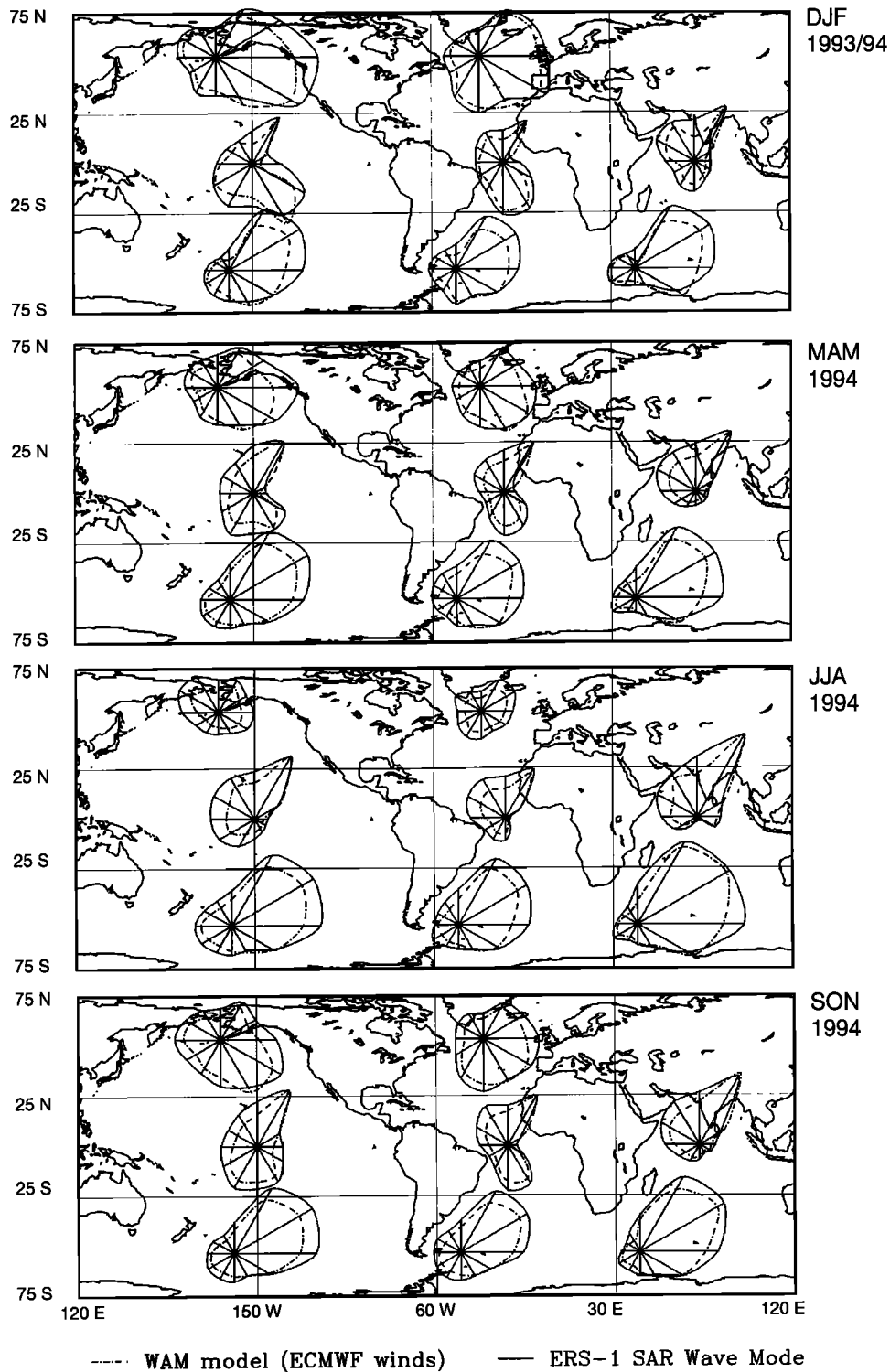
----· WAM model (ECMWF winds)　　　——— ERS-1 SAR Wave Mode

Figure 17b. Same as Figure 17a, but for swell.

south by Antarctic sea ice and thus has rather limited fetch to produce swell with a significant northward component. The existence of such components therefore implies rather strong northward or northeastward blowing winds. Katabatic winds could be a candidate, particularly as they are notoriously difficult to capture adequately in global circulation models. However, the predominantly southeasterly component of katabatic winds is not consistent with the easterly propagation direction

of the swell. We have no ready explanation for this discrepancy.

4.5. North-South Distributions Through the Pacific

As a further example of the detailed spatial-spectral information provided by the ERS-1 SWM, we have investigated the distribution of wave parameters in five areas along a meridional section of the Pacific for the boreal winter DJF 1993–1994
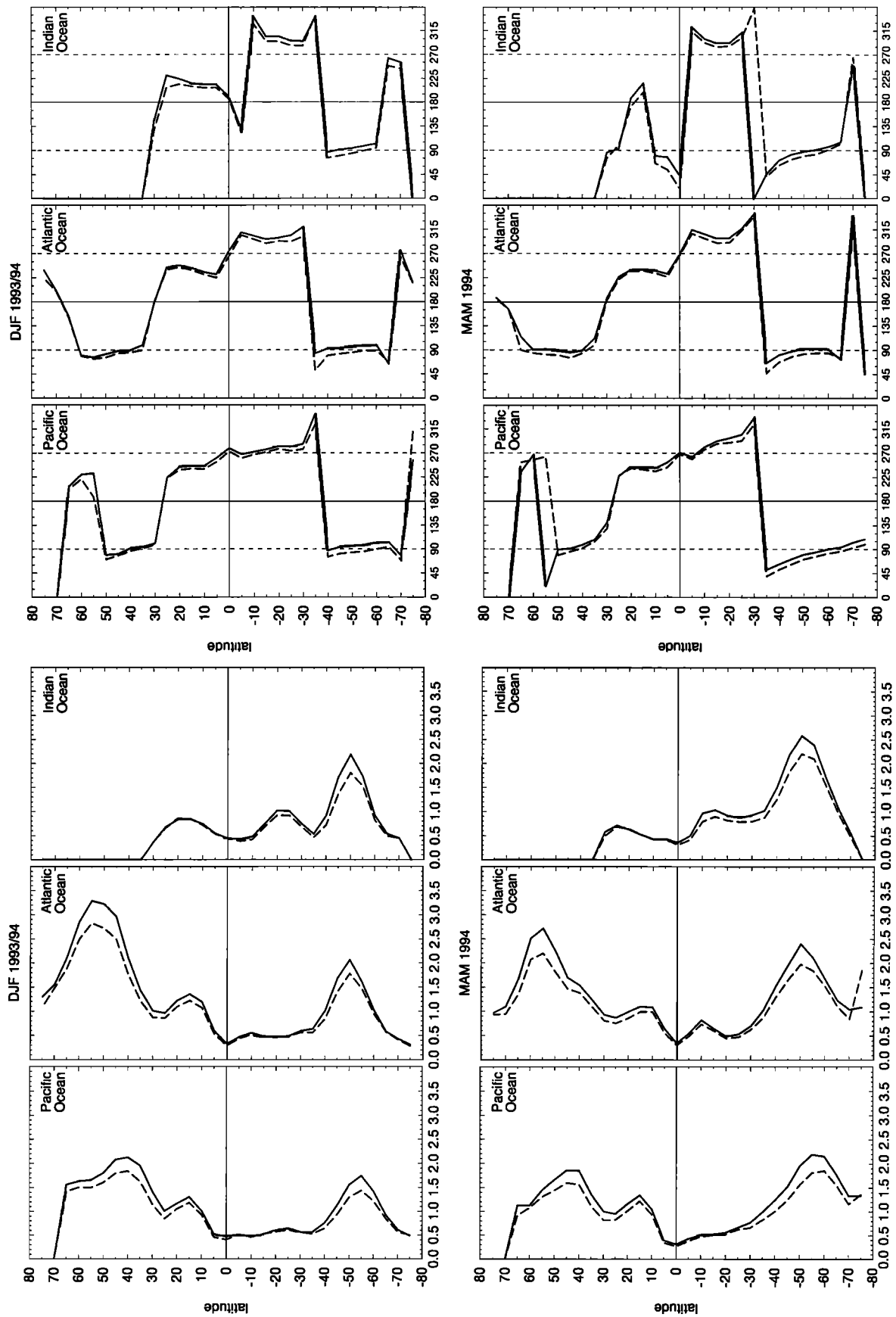
Figure 18a. Seasonal zonal (left) mean wave heights and (right) directions in the Pacific, Atlantic, and Indian Ocean for the four seasons from DJF 1993–1994 to SON 1994. Solid lines, modeled; dashed lines, retrieved from ERS-1 SWM. For wind sea.
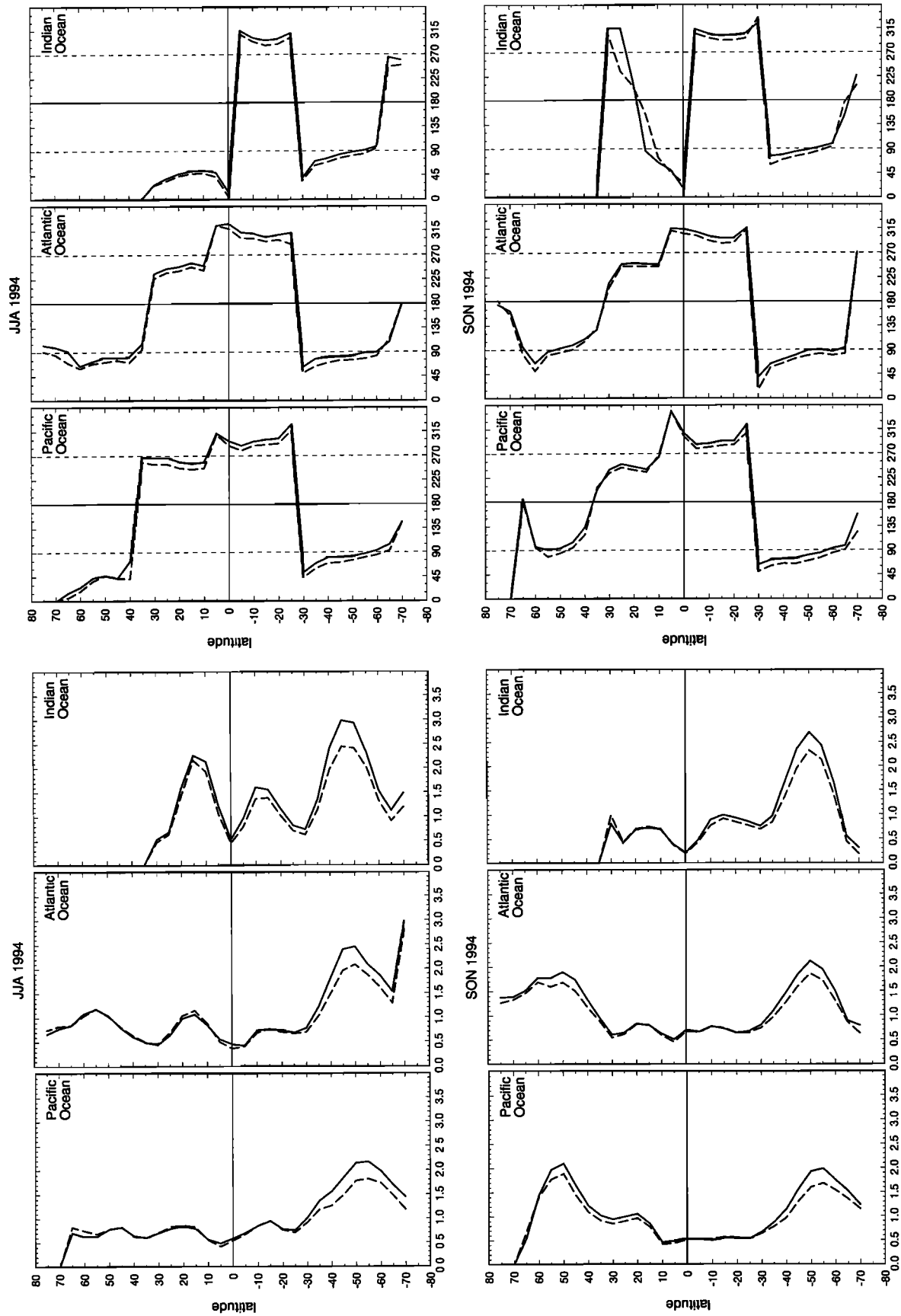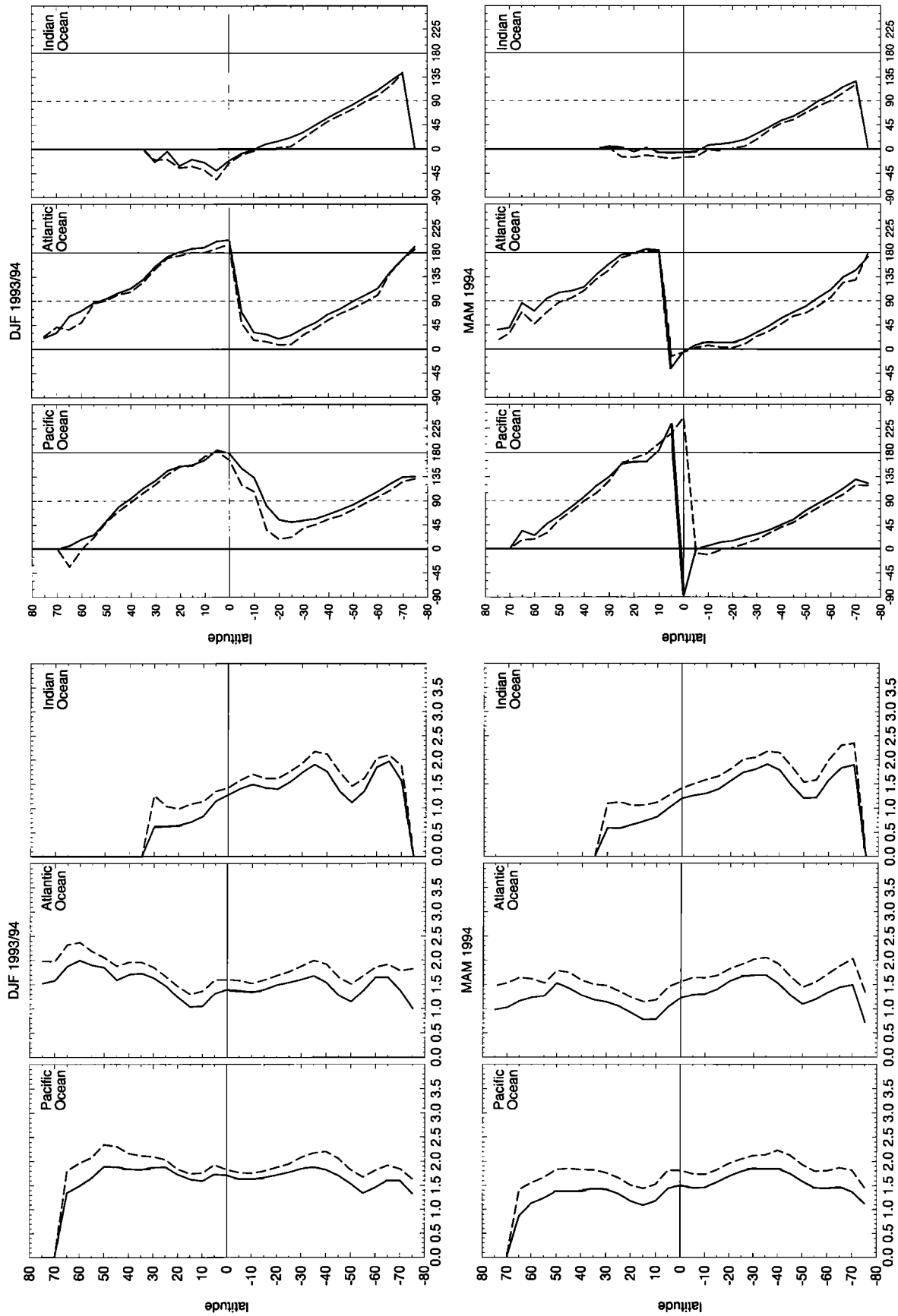
Figure 18a. (continued)
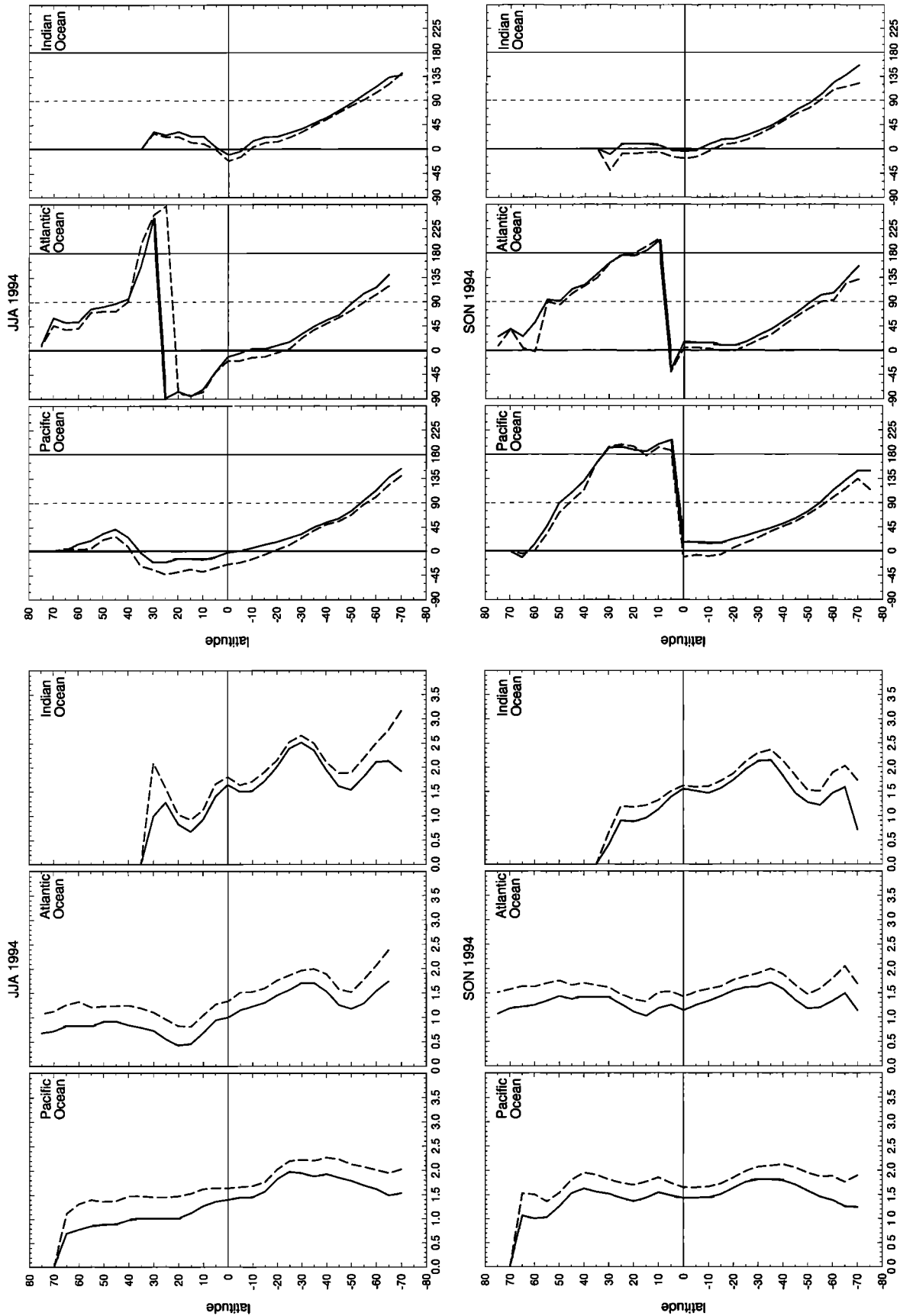
Figure 18b. Same as Figure 18a, but for swell.
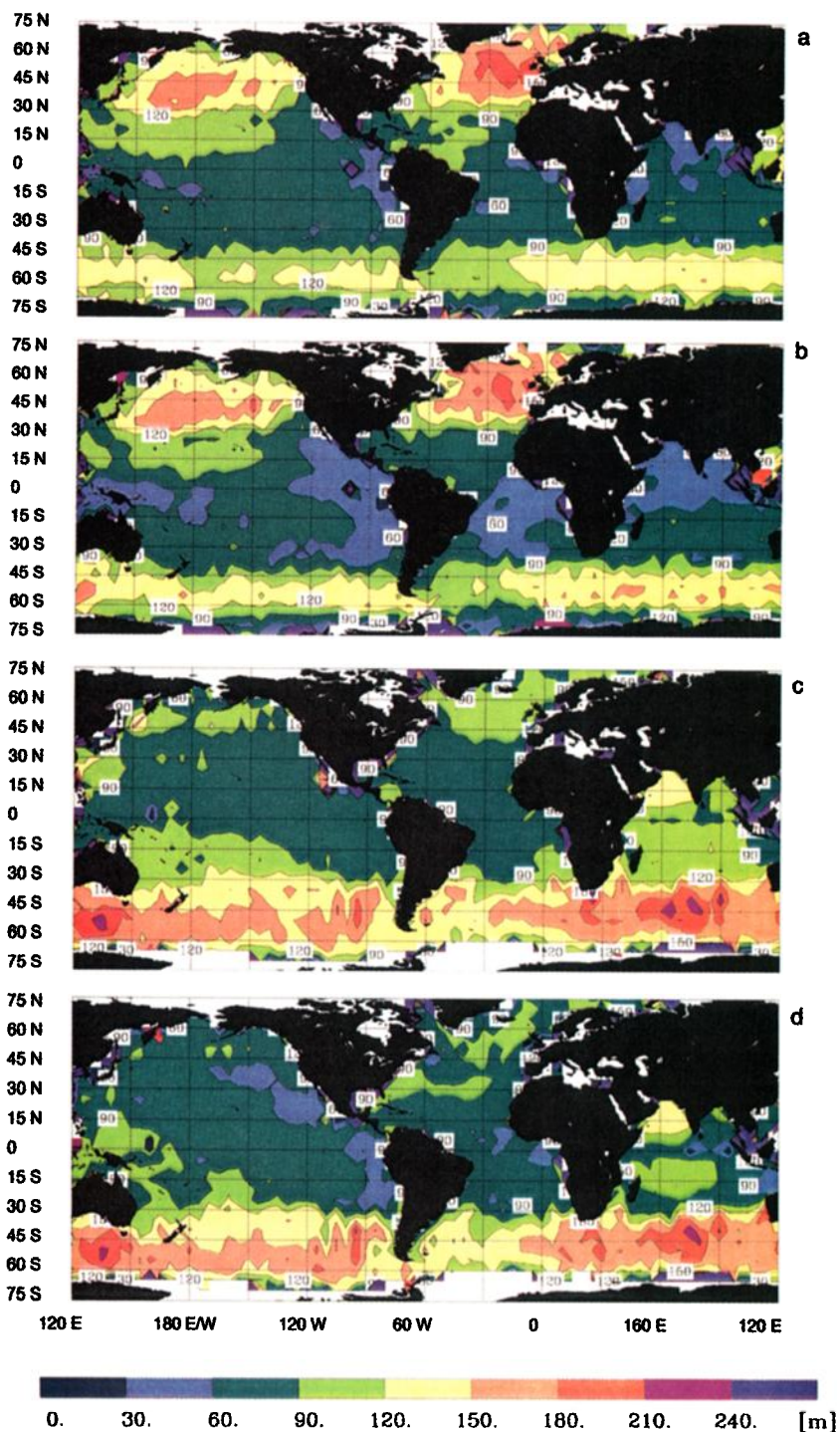
Figure 18b. (continued)

Plate 5. Same as Plates 3a and 3b for the seasonal mean wind-sea wavelength. (a) DJF 1993–1994 WAM, (b) DJF 1993–1994 ERS-1 SWM, (c) JJA 1994 WAM, and (d) JJA 1994 ERS-1 SWM.

and summer JJA 1994 (Figures 20a and 20b). The areas are representative of the northern and southern tropics and mid-latitudes and the Ross Sea in the Antarctic Ocean. Figures 20a and 20b depict the polar wave rose plots of the directional distributions for swell, while Figure 21 shows the relative distributions of wind sea, swell, and mixed wind-sea–swell wave heights.

The directional distributions exhibit considerable structure, with a pronounced seasonal dependence. They can again be explained in terms of the various wind systems characterizing the different latitudinal zones of the Pacific.

As expected, the distribution curves of retrieved swell wave heights (dashed curves) are shifted to higher values than the corresponding model distributions, while the opposite holds, although less pronounced, for the wind-sea curves. A noticeable feature of the distributions (apparent also in the spatial distributions shown earlier) is that the mean significant wave heights are considerably higher for swell than for wind sea.
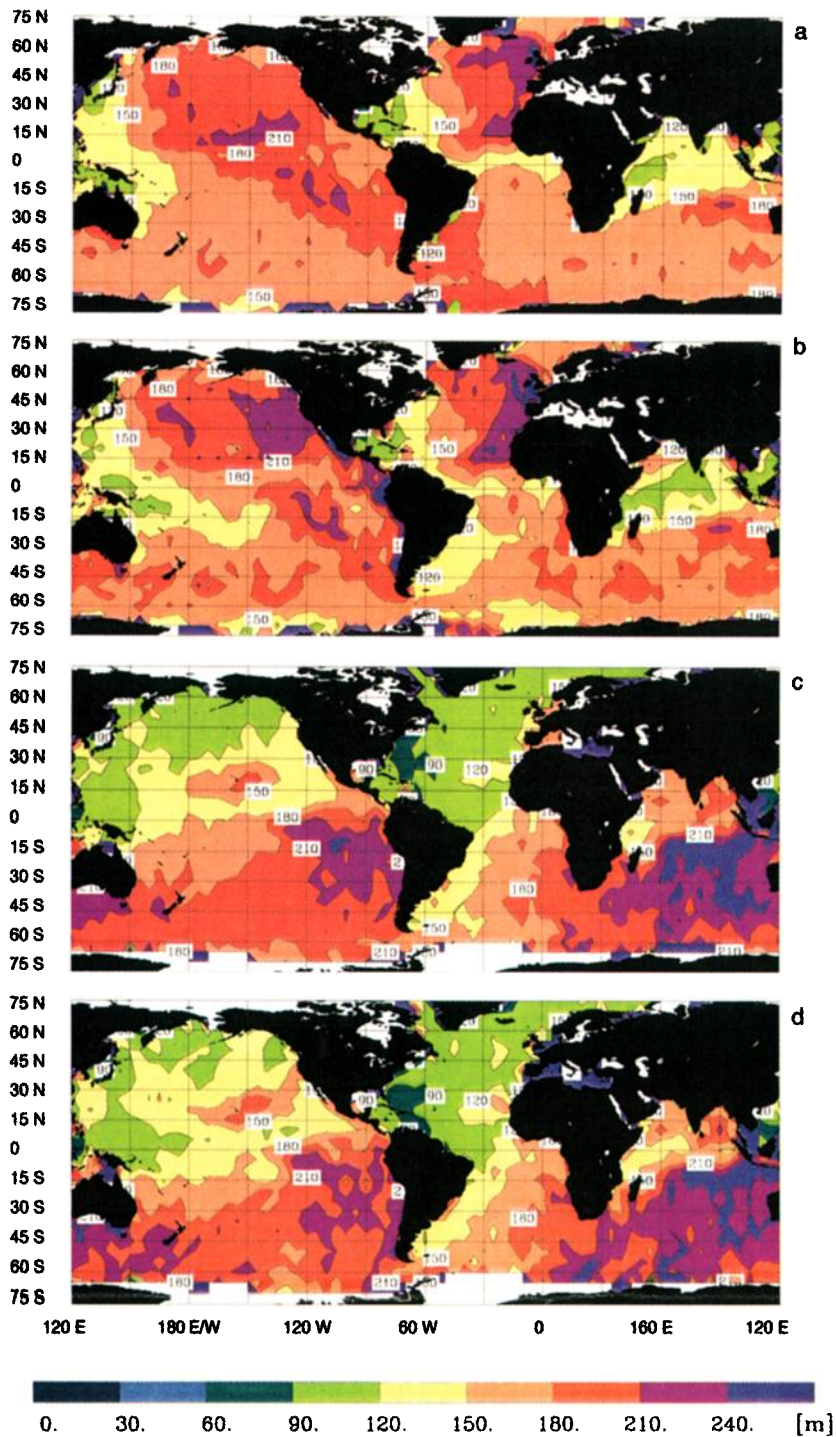
Plate 6. Same as Plate 5, but for swell.

This is because a given spectral wave component, although attaining its maximum energy at the end of its relatively short wind-sea growth period, subsequently propagates through the ocean for a significantly longer period as swell.

We note that while the modeled and retrieved directional distributions for swell are generally consistent with the hypothesis that the WAM model underestimates swell because of a too large swell dissipation, individual features of the polar distributions do not appear to support this interpretation. In particular, the NNE and SSE traveling swell components in

northern hemisphere and southern hemisphere tropics are overestimated by the WAM model. In the next section we analyze this phenomenon in more detail in the spectral domain.

4.6. Stratification With Respect to Swell System Wavelength

For a clearer insight into the nature of the differences between the modeled and retrieved wave spectra we need to stratify the partitioned wave systems with respect to wave-
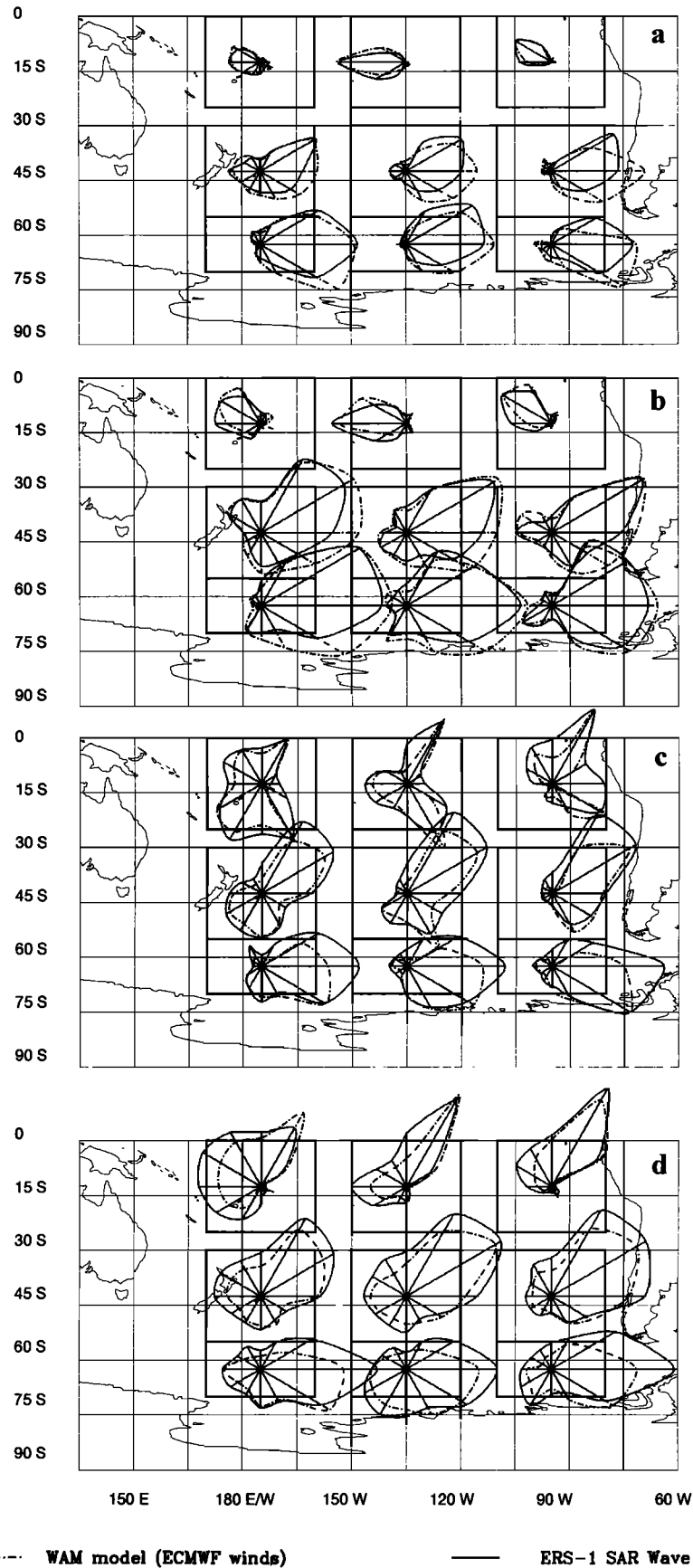
Figure 19.   Seasonal directional wave height distribution of the wind sea and swell in selected areas of the South Pacific. (a) DJF 1993–1994 wind sea, (b) JJA 1994 wind sea, (c) DJF 1993–1994 swell, and (d) JJA 1994 swell. Dashed-dotted lines, modeled; solid lines, retrieved.
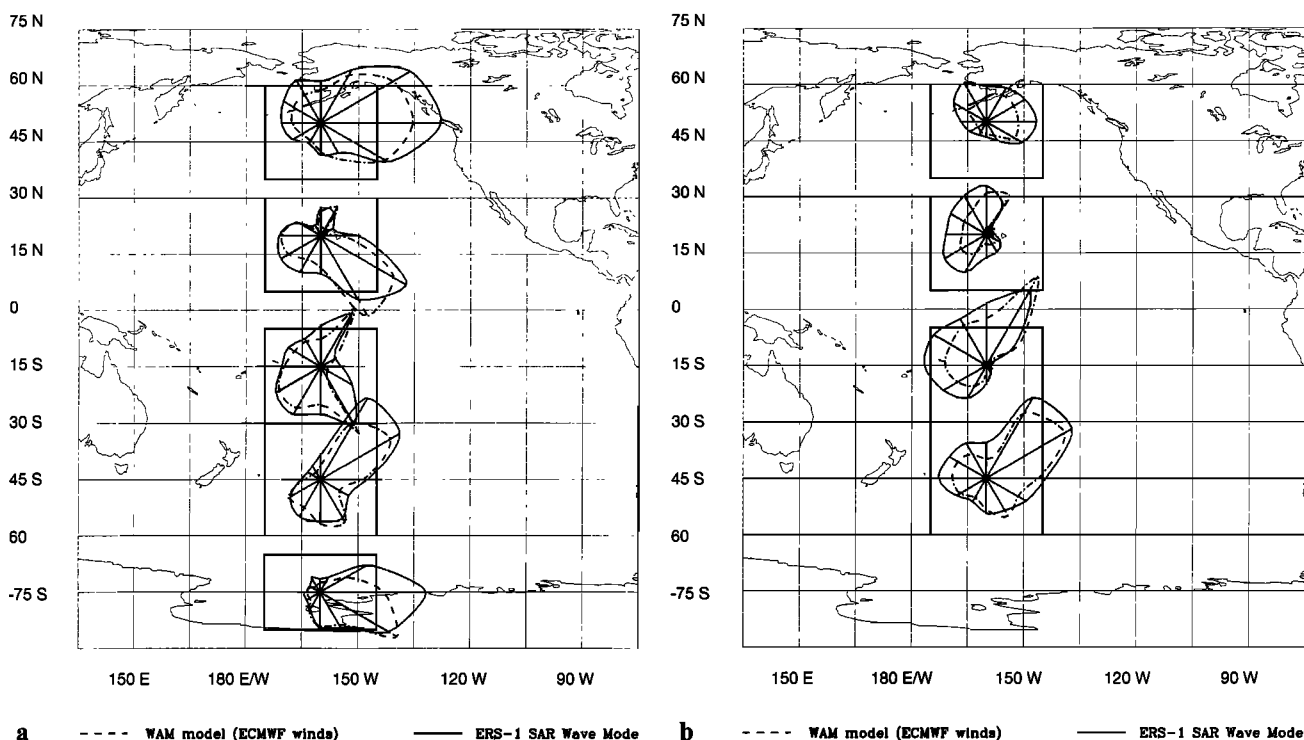
a - - - - WAM model (ECMWF winds) ———— ERS-1 SAR Wave Mode **b** - - - - WAM model (ECMWF winds) ———— ERS-1 SAR Wave Mode

Figure 20. Seasonal directional wave height distribution of the swell in five meridionally distinct boxes of the Pacific Ocean zonally bounded between 170°E and 150°W for (a) DJF 1993–1994 and (b) JJA 1994. Dashed-dotted lines refer to WAM model values, and solid lines refer to ERS-1 SWM values.

length as well as direction. Plate 7 shows the global distributions of mean wave height for the same winter and summer seasons DJF 1993–1994 (Plates 7a and 7b for WAM and ERS-1 SWM, respectively) and JJA 1994 (Plates 7c and 7d for WAM and ERS-1 SWM, respectively) considered previously, but now only for the longest wavelength swell system in each spectrum. To be included in the statistic, however, the swell wavelength was required to exceed a lower threshold, set in Plate 7 at 250 m. Consistent with our general findings for the total swell, the SWM-derived wave heights for these swell systems are again higher than the WAM wave heights. However, in contrast to the maps of the total swell wave height (defined as the rms value of the energy summed over all partitioned swell systems), the distributions for individual long wavelength wave systems are seen to be very similar to the maps of mean swell wavelengths. One can thereby more easily identify the regions into which the long wavelength swell is radiated from the midlatitude source regions.

Figures 22a and 22b show the associated directional swell wave height distributions in different sampling areas in the South Pacific for different lower long wavelength thresholds. With increasing wavelength threshold, the wave heights diminish, as expected. The model wave heights generally decrease faster than the SWM-retrieved wave heights, as again expected if the underestimation of swell by the model is due to a too strong model dissipation acting selectively on the longer swell components. However, the discrepancies in the details of the directional distribution increase with the swell wavelength, and not all of these can be explained simply by an incorrect dissipation expression. For example, the WAM model predicts significant SE traveling swell components in the southern hemisphere in the northern winter, presumably radiating from

northern midlatitude storms, which are not seen in the retrieved swell.

The processes involved in the transformation of wind sea into swell and the subsequent propagation of swell over large distances in the ocean are clearly complex and cannot be adequately analyzed within the framework of a general statistical study. A more appropriate approach for a process analysis would be a detailed investigation of a set of individual events. The ERS SWM measurements provide a valuable comprehensive database for such investigations, but these lie outside the scope of the present exploratory study.

5. Analysis of the rms Orbital Velocity

5.1. General Considerations

As already pointed out, a basic limitation of SAR ocean wave images is the azimuthal cutoff of the image spectrum caused by the nonlinear velocity bunching mechanism (HH; HBHH). The cutoff normally lies within the wind-sea part of the spectrum and suppresses the direct spectral information provided by the SAR on short to moderate wavelength waves with significant components of propagation in the azimuthal direction. However, the azimuthal cutoff wavenumber also provides a direct measure of an important integral parameter of the wave field, the rms orbital velocity component in the range direction. This information is used in the retrieval algorithm to adjust the rms orbital velocity to reproduce the observed cutoff, thereby partially replacing the missing direct spectral information at high wavenumbers, as discussed in section 2.2.2. However, the cutoff wavenumber, as a measure of the orbital velocity, is also useful data in its own right.
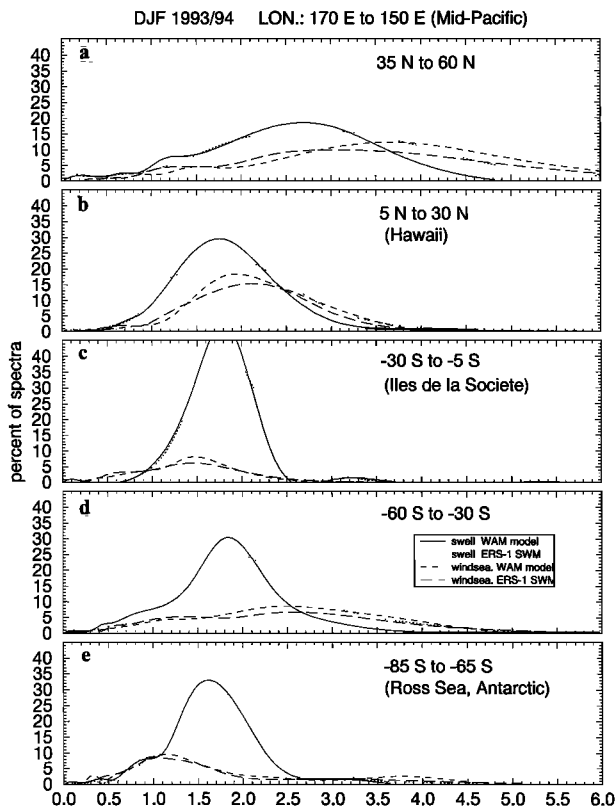
DJF 1993/94   LON.: 170 E to 150 E (Mid-Pacific)

Figure 21. Distribution of seasonal wind sea, swell, and mixed wind-sea–swell wave heights for the five meridionally distinct mid-Pacific boxes of Figure 20 for DJF 1993–1994. Solid lines refer to WAM model values, and dashed lines refer to ERS-1 SWM values. Figure 21b corresponds to an area around Hawaii, Figure 21c corresponds to an area around the Îles de la Société, and Figure 21e corresponds to an area of the Ross Sea in the Antarctic.

5.2. Comparison of Observed Versus Simulated Cutoff

Figure 23 shows scatter diagrams and regression lines for the observed and simulated azimuthal cutoff wavelengths for the boreal winter DJF 1993–1994 in the tropics and the northern and southern hemisphere extratropics. The observed azimuthal cutoff wavelengths were determined directly from the SAR imagette spectra, while the simulated cutoff wavelengths were inferred, using the same algorithm, from the SAR imagette spectra computed from the retrieved wave spectra. Regression line slopes close to 1 and correlation coefficients of 0.9 and higher in all three data sets indicate that the adjustment of the cutoff parameter in the retrieval algorithm was successful.

5.3. Spectral Resolution Imposed by the Cutoff

To estimate the impact of the azimuthal cutoff on the retrieval of wind-sea and swell systems, we have computed the ratio k_c/k_x of the observed azimuthal cutoff wavenumber to the mean azimuthal wavenumber component for an ensemble of wind-sea and swell systems. Figure 24 shows the resulting histograms for three wind-sea (Figure 24a) and swell (Figure 24b) data sets for the period DJF 1995–1996 for the northern hemisphere extratropics, the tropics between 25°N and 25°S, and the southern hemisphere extratropics. The medians of the histograms are listed in Table 4, together with the percentage of wave systems with ratios $k_c/k_x > 1$, representing waves that

can be explicitly imaged by the SAR. The values clearly demonstrate the ability of the ERS-1 SAR to detect a substantial fraction of the swell systems encountered in the ocean, despite the high R/v ratio. A fair fraction of 30% of the wind-sea systems can also be directly imaged by the SAR, but short wavelength wind seas generated by light winds cannot be seen at all by the SAR.

5.4. Global Analysis of the Cutoff

A global map of the mean azimuthal cutoff wavelength λ_c for DJF 1995–1996 is shown in Plate 8. High cutoff wavelengths corresponding to high rms orbital velocities are found, as expected, in the regions of high winds in midlatitudes. In addition, a pronounced fetch effect is seen. Young wind seas have higher energies at shorter wavelengths and therefore higher rms orbital velocities than well-developed wind seas [cf. Komen et al., 1994]. Thus the cutoff wavelength is significantly higher in the western parts of the midlatitude ocean basins and in enclosed or partially enclosed seas such as the Baltic Sea, Mediterranean Sea, Gulf of Mexico, Caribbean Sea, Bering Sea, or the seas south of New Guinea.

In view of the strong dependence of the orbital velocity on fetch a general expression relating λ_c alone to the wind velocity u_{10} at 10-m height, for example, in the form $\lambda_c = 25u_{10}$ [Chapron et al., 1995], cannot be expected to be generally valid. Although dimensionally consistent and therefore presumably appropriate for fully developed seas, the expression yielded a low correlation of 0.3–0.4 between the observed and predicted cutoff wavelengths for the global data set of DJF 1995–1996.

6. Summary and Conclusions

The ERS-1 SAR wave mode (SWM) data represent the first data set to provide detailed spectral information of ocean surface waves with continuous global coverage over several years. In the first part of this paper we have carried out an assessment of the SWM data quality and the performance (fidelity) of the ocean wave spectral retrieval algorithm by HBHH over the 3-year period January 1993 to December 1995 for which reliable SWM data are available. In the second part we investigated the statistical properties of the retrieved wave spectra and intercompared the retrievals with wave spectra computed by the operational global wave model WAM of the European Centre for Medium-Range Forecasts.

Approximately 75% of the available SWM data yielded successful retrievals. This net return factor represented the product of two quality tests. About 12% of the SWM data were rejected for data quality reasons related to too low signal-to-noise ratios or contaminations such as slicks or wind rows. The retrieval performance (defined in terms of the level of agreement between the observed SAR spectrum and the SAR spectrum computed from the retrieved wave spectrum) was accepted for roughly 85% of the SWM data that passed the first test.

Iteration of the first-guess spectrum used as input for the inversion was found to have a significant positive impact on the fidelity of the retrievals. Tests with different numbers of iteration cycles suggest that one or preferably two iterations may represent a reasonable compromise in operational applications between computing costs and retrieval fidelity. For the present study we carried out five iterations and chose as the retrieval the inversion with the highest fidelity.

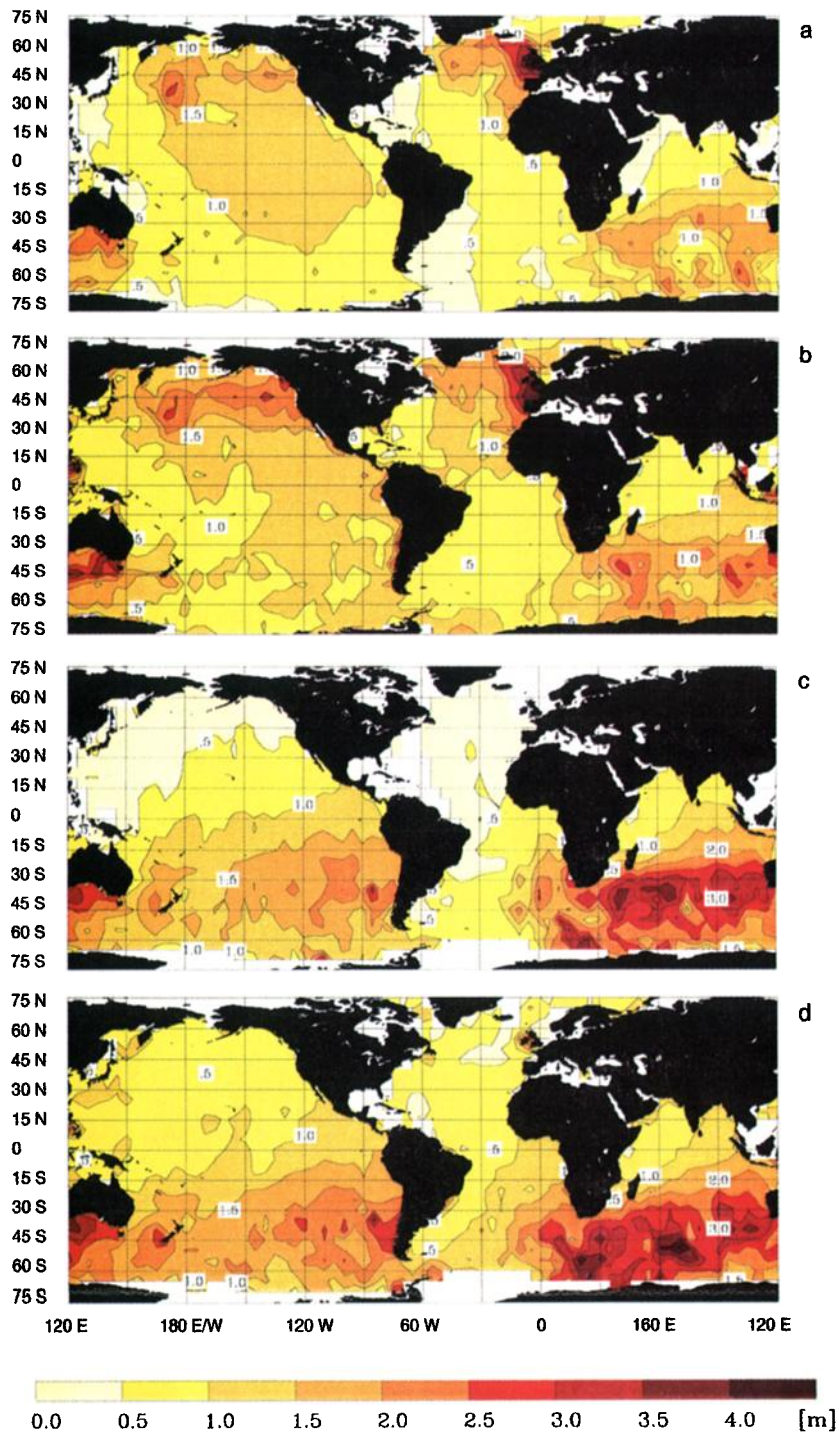In the statistical investigations in the second part of the

Plate 7. Global maps of seasonal mean wave height distributions of individual largest wavelength swell systems of wavelength exceeding 250 m. Plates 7a–7d same as Plates 5a–5d, respectively.

paper the SWM-retrieved data were analyzed together with the corresponding data computed with the ECMWF WAM model. The data were subdivided into wind-sea and swell constituents and were presented in the form of time series for different ocean basins, global maps for different seasons, and polar "wave rose" plots of directional energy distributions. In addition, results were presented for the dominant long wavelength swell components and for the cutoff wavelengths of the SWM

spectra (which provide a direct measure of the rms orbital velocity).

In the discussion of the intercomparison results, it was assumed that the retrieved spectra represented the "truth"; all discrepancies between the retrieved and modeled data were attributed to the model. This assumption will need to be scrutinized more carefully as further data become available, but for the present state of knowledge it appears a reasonable assump-
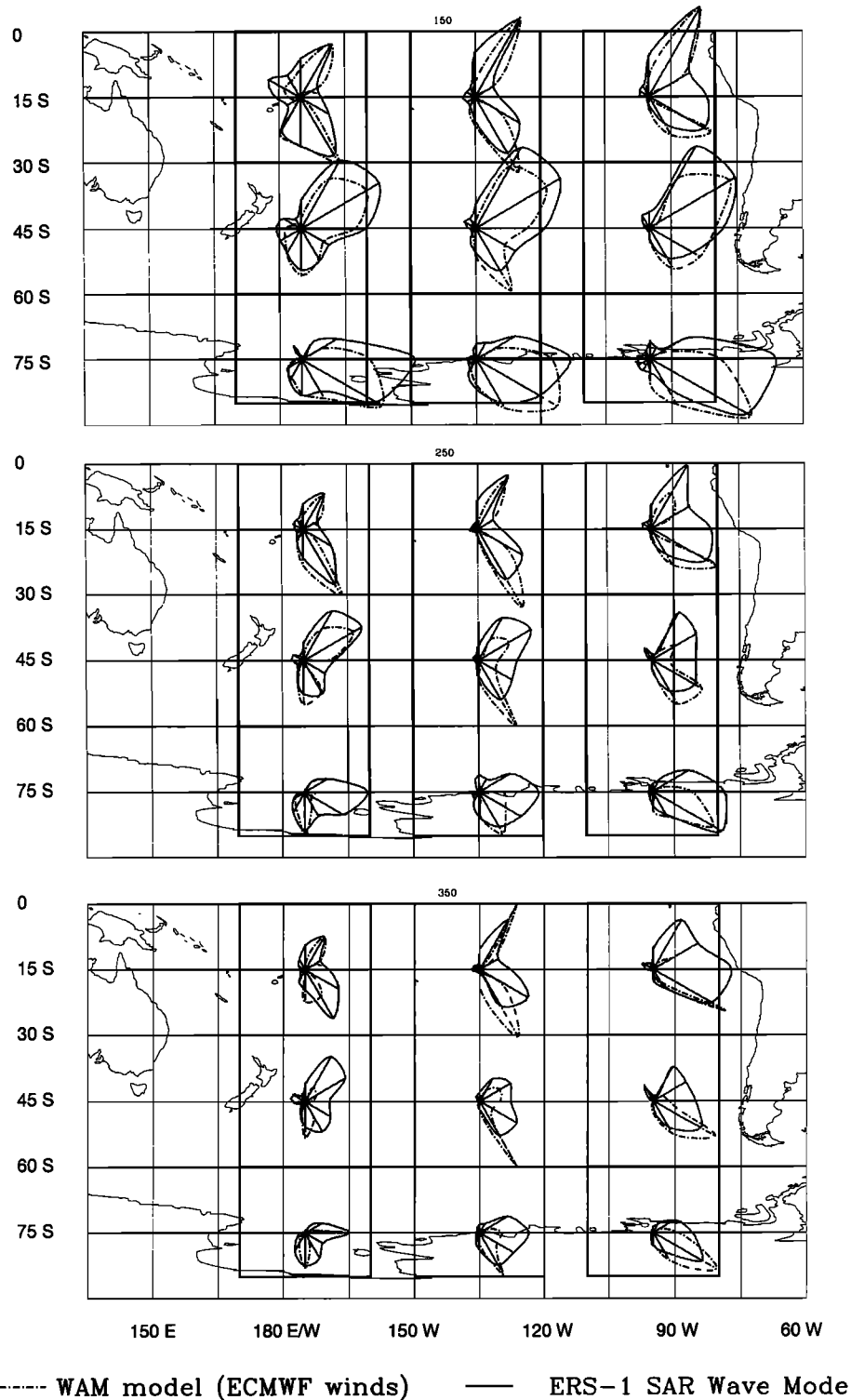
----- WAM model (ECMWF winds)   —— ERS–1 SAR Wave Mode

Figure 22a. Directional wave height distributions of individual longest wavelength swell systems in various sampling areas of the South Pacific for different lower wavelength thresholds; (top) λ > 150 m, (middle) λ > 250 m, and (bottom) λ > 350 m. For DJF 1993–1994.

tion; it would be difficult to explain the various types of discrepancies for wind sea and swell, different ocean regions, and different propagation directions, in terms of a common error source in the SAR retrievals. Also, validation studies of wave spectra retrieved from SAR spectra (e.g., HH; HBHH; E. Bauer and P. Heimbach, manuscript in preparation, 1998)

have revealed no obvious significant systematic errors in the SAR retrievals.

The retrieved and modeled data both confirm on a global scale the complexity of the spatial, temporal, and spectral distributions of ocean wave energy found previously by *Brüning et al.* [1994] in their first analysis of a 3-day period of SWM
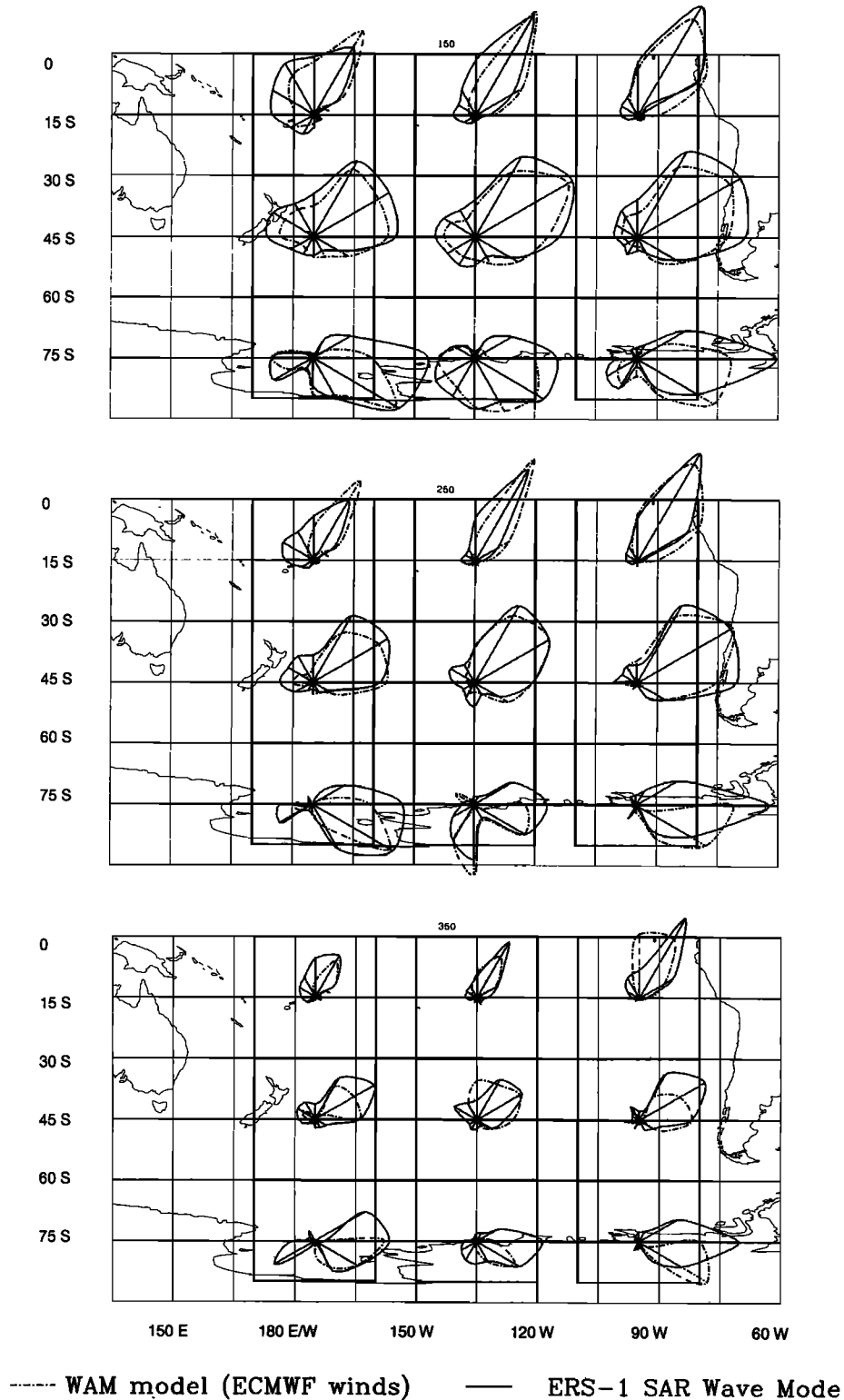
------ WAM model (ECMWF winds)   ——— ERS-1 SAR Wave Mode

Figure 22b. Same as Figure 22a, but for JJA 1994.

spectral data for the Atlantic. In view of this complexity the general structural agreement between the modeled and retrieved spectra is encouraging. It has been demonstrated by HH and HBHH that this cannot be attributed to the use of a first-guess model spectrum in the retrieval algorithm; the retrieval is largely decoupled from the input spectrum, particularly with the introduction of an iterative modification of the

input spectrum in the improved algorithm by HBHH. Their result is confirmed by further detailed sensitivity tests of the present data set.

The availability of global spectral data has made possible a more detailed analysis of the performance of the WAM model than has previously been feasible. However, the present statistical analysis summarized below is necessarily restricted in
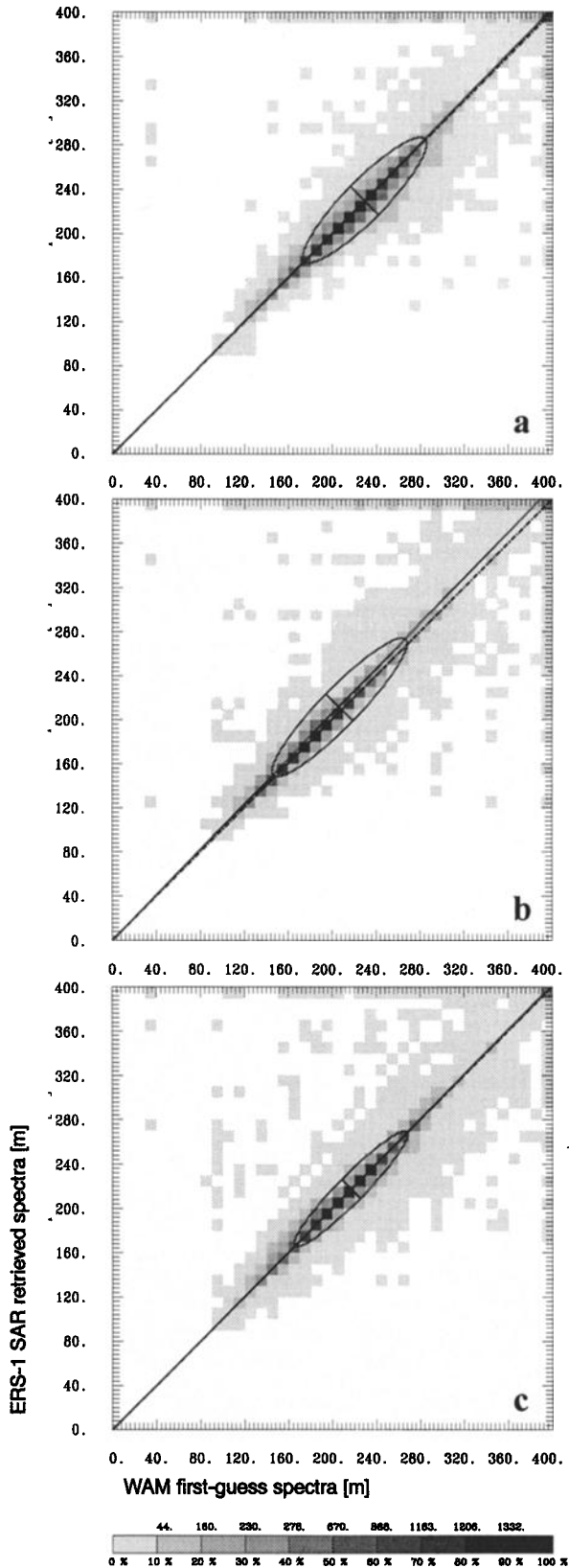
Figure 24. (a) Histogram of (a) wind-sea and (b) swell systems with respect to the ratio k_c/k_x of the observed azimuthal cutoff wavenumber to the mean azimuthal wavenumber component. The data for the period DJF 1995–1996 were divided into three ensembles for the northern hemisphere extratropics, the tropics between 25°N and 25°S, and the southern hemisphere extratropics.

Figure 23. Regression between observed and simulated azimuthal cutoff wavelengths for (a) northern hemisphere extratropics, (b) tropics, and (c) southern hemisphere extratropics.
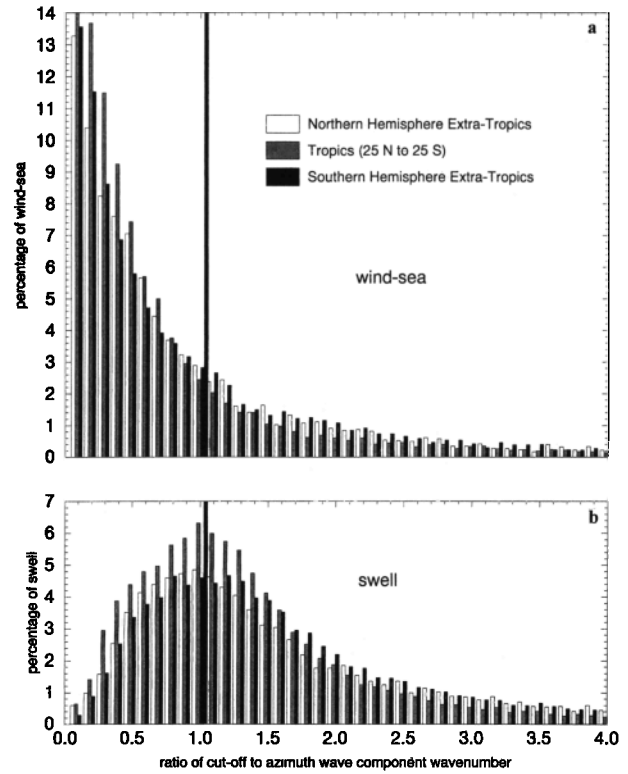
scope. Moreover, a quantitative assessment of the dynamical effects identified by our statistical approach is made difficult by the continual assimilation of observed altimeter data in the ECMWF operational model. This attenuates systematic model errors, for example, in swell propagation. Specific investigations of a larger ensemble of individual wave events and the application of the WAM model without wave data assimilation can be expected to yield significantly more insight into the basic wave dynamical processes governing the general statistical results presented here. Nevertheless, the following general conclusions can be drawn from our analysis.

1. The time series and regression parameters of significant wave height indicated a good overall agreement between mod-

Table 4. Characteristics of Histograms of Observed Azimuthal Cutoff Wavenumber to Wavenumber Component in the Azimuth Direction

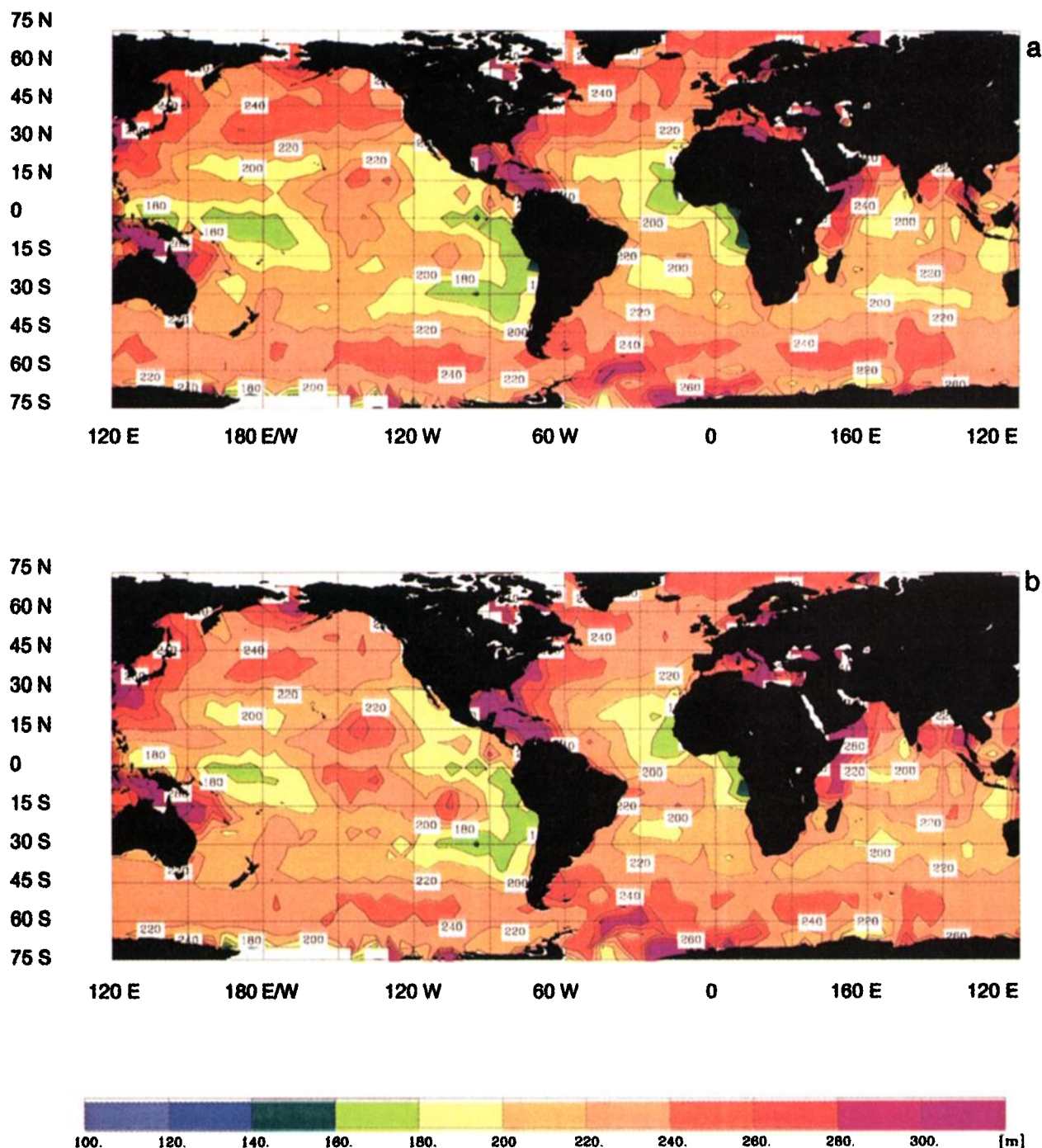|	Median		Percent of Waves With Ratio $k_c/k_x > 1$	
	Wind Sea	Swell	Wind Sea	Swell
Northern hemisphere	0.65	1.4	34	72
Tropics	0.5	1.85	28	78
Southern hemisphere	0.65	1.5	35	74

Plate 8. Global maps of the seasonal mean azimuthal cutoff wavelength for DJF 1995–1996. (a) Cutoff simulated from retrieved wave spectrum; (b) cutoff from observed SWM imagette spectrum.

eled and retrieved spectra, with a small but systematic underestimation of H_s by the WAM model in all ocean basins.

2. The decomposition of the wave energy into wind-sea and swell components revealed that the net wave height underestimation by the model is due to an underprediction of the swell components by 20–30%, the wind sea being slightly overpredicted on average by about 10%. This holds with few exceptions throughout the 3-year period and for all ocean basins and seasons.

3. The relative wind-sea overprediction was found to be

fairly constant, but slightly higher for high sea states in the midlatitude winters, suggesting that either the wind dependence of the WAM input source term should be slightly reduced or that the analyzed wind fields used to drive the model are too strong.

4. The relative swell bias is fairly uniformly distributed but exhibits maxima in the midlatitude summers. In contrast to the fairly constant relative wind-sea bias, the negative swell bias increases in relative magnitude with decreasing swell wave height. We interpret this as reflecting a dependence of the

swell underprediction on the wave age, larger wave ages being associated statistically with smaller wave heights (wave age refers here literally to the travel time of the swell since emerging from the wind-sea generation region). A model error with this characteristic may be explained by a dissipation source term which is too large for low frequencies or not sufficiently nonlinear. Another possible explanation is an inadequate representation of the nonlinear transition from wind sea to swell in the strongly simplified discrete interaction parametrization. However, this would not readily explain the increase of the swell error with decreasing wave height.

5. Modeled wavelengths were generally found to be in close agreement with the retrieved wavelengths, also favoring the hypothesis of errors in the swell dissipation rather than in the representation of the nonlinear wind-sea-swell transition process.

6. Most of the temporal and spatial features of the wave field distributions could be explained by the general properties of the seasonally varying global wind system. The data for both wind sea and swell exhibited a pronounced fetch dependence extending across entire ocean basins. This information is valuable for determining the transition of a growing wind sea to a fully developed state, for which little data is otherwise available. Intercomparisons of retrieved and modeled fetch dependences suggest no systematic errors of the WAM model in this respect. Global maps of mean swell wavelengths and the wave heights of long swell, together with polar "wave rose" distributions of wave propagation directions, were useful in identifying the radiation emanating from the midlatitude storm areas into distant regions. Some discrepancies between modeled and retrieved swell data were detected in the radiation of long swell from the northern into the southern hemisphere, which appeared to be more effective in the model than observed.

In summary we emphasize again that our conclusions from this first exploratory study of the 3-year ERS-1 SAR wave mode data set were based solely on statistical analyses. These have provided an interesting overview of the seasonally varying wind-sea and swell distributions of the global ocean and have demonstrated an encouraging overall correspondence between the complex wave systems inferred from the ERS SAR wave mode data and computed by the ECMWF operational wave model WAM. The statistical analyses also enabled the identification of a number of discrepancies between the two data sets, pointing to various features and possible shortcomings of the WAM model or the forcing wind fields, which require closer investigation. However, we have not undertaken investigations of individual events, which would have presumably shed more light on the underlying wave dynamical processes responsible for the mean distributions and observed discrepancies. It is hoped that this first investigation will motivate such dynamical event studies, for which the ERS-1/2 SWM system has provided and is still producing a unique comprehensive database.

Appendix

A1. Orbit, Instrument, and Data Specifications for the ERS-1 SWM

Tables 5 and 6 list data on the ERS-1 satellite, its orbit, the SAR instrument, the wave mode fast delivery product, and the repeat cycles between July 1992 and May 1996.

Table 5. Some ERS-1 Satellite and SAR Instrument Specifications

Aspect	Description
Start	July 17, 1991
Altitude (nadir)	782–785-km polar orbit (Sun synchronous)
Inclination	98.52°
Orbit period	about 100 min ($\cong$14.3 orbits per day)
Platform velocity	7455 m/s
Daily coverage	about 1100 spectra per day on average
Incidence angle	until June 1995, 19.9° at center of imagette (right looking); after June 1995, 23.5°
Polarization	linear vertical (VV)
Radar Bragg frequency	5.3 GHz, C band (5.6 cm)
Imagette size	10 km (range) × 5 km (azimuth)
Product spacing	200 km along track (every 30 s)
Spectral grid	12 wavenumbers in logarithmic spacing corresponding to wavelengths between 100 and 1000 m
	12 directional sectors of 15° width (between 0° and 180°, anticlockwise relative to azimuth)
Intensity	8 bit (0–255) relative to maximum
Number of looks	three-look incoherent averaging of single-look amplitude
SAR integration time	1.8 s
R/v ratio	112 s (R, distance SAR − target; v, platform velocity in orbit)

A2. SWM, WAM, and Cost Function Grid

Three different Cartesian wavenumber, polar wavenumber, or frequency/direction grids are involved in the inversion process: (1) the ERS-1 SAR Wave Mode grid (k, θ); the SWM spectra of the FDP are given on a polar wavenumber grid on a semidisc and are composed of 12 15° angular sectors between 0° and 180° running counterclockwise relative to the satellite flight direction (azimuth) and $N_{swm} = 12$ wavenumbers corresponding to wavelengths between 100 and 1000 m on a logarithmic scale

$$k_{j+1} = 10^{1/(N_{swm}-1)}k_j \qquad j = 1, \cdots, N_{swm}$$

with

$$k_1 = \frac{2\pi}{100}\ \mathrm{m}^{-1}$$

(2) the WAM model grid (f, θ); the first-guess WAM and the retrieved wave spectra are defined on a polar frequency/direction grid composed of 12 30° angular sectors between 0° and 360°, running clockwise relative to north, and $N_{wam} = 25$

Table 6. ERS-1 Mission Phases and Repeat Cycles Between July 1992 and May 1996

Phase	Start	End	Repeat Cycle, days	Orbits Per Cycle
C	April 14, 1992	December 21, 1993	35	501
D	December 24, 1993	April 10, 1994	3	43
E	April 10, 1994	September 28, 1994	168	2408
F	September 28, 1994	March 21, 1995	168	2408
G	March 21, 1992	end	35	501

The satellite was switched off in June 1996 but is parked in orbit in a "sleeping" mode.

frequencies corresponding to logarithmically spaced wavelengths between 9 and 895 m, or frequencies

$$f_{j+1} = 1.1f_j \qquad j = 1, \cdots, N_{wam}$$

with

$$f_1 = 0.04177 \text{ Hz}$$

(3) the cost function grid (k_x, k_y); both the observed SWM image spectrum and the first-guess wave spectrum are interpolated to a $N_{cart} \times N_{cart}$ cartesian wavenumber grid with $N_{cart} = 128$ and

$$k_x(j), \, k_y(j) = j\Delta k$$

with

$$-\frac{N_{cart}}{2} < j \leq \frac{N_{cart}}{2} \qquad \Delta k = \frac{2\pi}{32} \text{ m}^{-1}$$

on which all computations (nonlinear mapping, cost function, etc.) are performed.

To properly account for the spectral smoothing incurred through the processing of the SWM imagette to the low-resolution polar wavenumber grid of the SWM FDP imagette spectrum, a smoothing filter is introduced whenever a SAR image spectrum is computed from a model spectrum. The filter is obtained by transforming the computed SAR image spectrum from the fine Cartesian grid (k_x, k_y) to the coarse polar grid (k, θ) and subsequently interpolating back to the (k_x, k_y) grid, yielding a net smoothing of the simulated high-resolution SAR spectrum analogous to the treatment of the FDP.

A3. Regression Analysis

In standard regression analysis a straight line $y(x) = mx + a$ is drawn through a scatterplot of data pairs (x_i, y_i) with slope m and y-axis intercept a, chosen such that the sum of the square differences $\Sigma_i[y_i - y(x_i)]^2$ is minimized. However, the use of two regression parameters makes it more cumbersome to intercompare the effective calibration of two data sets, and we have therefore restricted the regression line in our analyses to pass through the origin, $a = 0$ (comparisons with adjustable intercepts have shown that these in fact have little influence).

Instead of the asymmetric definition of the square error in terms of the ordinate errors, we have then fitted our regression line

$$y_i = bx_i$$

through the origin by minimizing the sum of the orthogonal distances of the data points from the regression line. The extreme values of this quantity yield the major and minor axes of the covariance ellipse. The method is not only symmetric with respect to an interchange of x and y but is also invariant with respect to rotations in the x, y plane [see, e.g., *Preisendorfer*, 1988; *Bauer et al.*, 1992; *Bauer and Staabs*, 1998]. The slope b is given by

$$b = \tan \phi \qquad \tan 2\phi = \frac{\langle 2xy \rangle}{\langle x^2 \rangle - \langle y^2 \rangle}$$

and $\langle \ \rangle$ denotes the average over the data ensemble. The angle ϕ as defined above is actually not invariant with respect to an interchange of x and y, which yields $\phi \rightarrow \phi + 90°$. The correct solution yielding the major rather than the minor ellipse axis can be determined by comparing the square errors

for the two solutions. (The only exception to our symmetrical regression approach is in the scatter diagram of Figure 8, comparing the retrievals for a modified and nonmodified input spectrum. Here we resorted to the standard nonsymmetrical regression analysis, as this yielded a more realistic-looking line passing through the maxima of the distribution.)

References

Allan, T. D. (Ed.), *Satellite Microwave Remote Sensing*, 526 pp., Ellis Horwood, Chichester, England, 1983.

Alpers, W., Monte Carlo simulations for studying the relationship between ocean wave and synthetic aperture radar image spectra, *J. Geophys. Res.*, 88, 1745–1759, 1983.

Alpers, W., and K. Hasselmann, Spectral signal-to-clutter and thermal noise properties of ocean wave imaging synthetic aperture radars, *Int. J. Remote Sens.*, 3, 423–446, 1982.

Alpers, W., D. B. Ross, and C. L. Rufenach, On the detectability of ocean surface waves by real and synthetic aperture radar, *J. Geophys. Res.*, 86, 6481–6498, 1981.

Alpers, W., C. Brüning, and K. Richter, Comparison of simulated and measured synthetic aperture radar image spectra with buoy-derived ocean wave spectra during the shuttle imaging radar-B mission, *IEEE Trans. Geosci. Remote Sens.*, 24, 559–566, 1986.

Bacon, S., and D. J. T. Carter, Wave climate changes in the North Atlantic and North Sea, *Int. J. Climatol.*, 11, 545–558, 1991.

Bamler, R., and B. Schättler, SAR geocoding: Data and systems, in *SAR Data Acquisition and Image Formation*, edited by G. Schreier, pp. 53–102, Wichmann, Heidelberg, Germany, 1993.

Bao, M., and W. Alpers, On the cross spectrum between single-look synthetic aperture radar images of ocean waves, *IEEE Trans. Geosci. Remote Sens.*, in press, 1998.

Bao, M., C. Brüning, and W. Alpers, A generalized nonlinear ocean wave–SAR spectral integral transform and its application of ERS-1 SAR ocean wave imaging, in *Proceedings of the Second ERS-1 Symposium, Hamburg, Germany, 11–14 October 1993, Eur. Space Agency Spec. Publ., ESA SP-361*, 219–224, 1994.

Bauer, E., and C. Staabs, Statistical properties of global significant wave heights and their use for validation, *J. Geophys. Res.*, 103, 1153–1166, 1998.

Bauer, E., S. Hasselmann, K. Hasselmann, and H. C. Graber, Validation and assimilation of Seasat altimeter wave heights using the WAM wave model, *J. Geophys. Res.*, 97, 12,671–12,682, 1992.

Bauer, E., S. Hasselmann, and K. Hasselmann, An operational wave forecast system using wind and wave data, in *Proceedings of the Second ERS Applications Workshop, London, 6–8 December 1995, Eur. Space Agency Spec. Publ., ESA SP-383*, 309–312, 1996a.

Bauer, E., K. Hasselmann, I. R. Young, and S. Hasselmann, Assimilation of wave data into the wave model WAM using an impulse response function, *J. Geophys. Res.*, 101, 3801–3816, 1996b.

Beal, R. C. (Ed.), *Directional Ocean Wave Spectra*, Johns Hopkins Univ. Press, Baltimore, Md., 1991.

Beal, R. C., T. W. Gerling, F. M. Monaldo, and D. G. Tilley, Measuring ocean waves from space, *Int. J. Remote Sens.*, 12, 1713–1722, 1991.

Bouws, E., D. Jannink, and G. J. Komen, The increasing wave height in the North Atlantic Ocean, *Bull. Am. Meteorol. Soc.*, 77, 2275–2277, 1996.

Breivik, L.-A., B. Haugse, H. Johnsen, H. E. Krogstad, and M. Reistad, Evaluation of SAR wave products, *Res. Rep. 2, Norw. Meteorol. Inst., Oslo*, January 1995.

Breivik, L.-A., M. Reistad, H. Schyberg, J. Sunde, H. E. Krogstad, and H. Johnsen, Assimilation of ERS SAR wave spectra in an operational wave model, *J. Geophys. Res.*, this issue.

Brooker, G., UWA processing algorithm specification, *Rep. ER-TN-ESA-GS-0342*, version 2.0, 26 pp., Eur. Space Res. and Technol. Cent., Noordwijk, Netherlands, 1995.

Brüning, C., On the relative importance of the ocean wave-radar modulation transfer function for inverting ERS-1 SAR image spectra into ocean wave spectra, in *Proceedings of the Second ERS-1 Symposium, Hamburg, Germany, 11–14 October 1993, Eur. Space Agency Spec. Publ., ESA SP-361*, 233–238, 1994.

Brüning, C., W. Alpers, L. F. Zambresky, and D. G. Tilley, Validation of a SAR ocean wave imaging theory by the shuttle imaging radar-B experiment over the North Sea, *J. Geophys. Res., 93*, 15,403–15,425, 1988.

Brüning, C., W. Alpers, and K. Hasselmann, Monte-Carlo simulation studies of the nonlinear imaging of a two-dimensional surface wave field by a synthetic aperture radar, *Int. J. Remote Sens., 90*, 1695–1727, 1990.

Brüning, C., S. Hasselmann, K. Hasselmann, S. Lehner, and T. Gerling, On the extraction of ocean wave spectra from ERS-1 SAR wave mode image spectra, in *Proceedings of the First ERS-1 Symposium, Cannes, France, 4–6 November 1992, Eur. Space Agency Spec. Publ., ESA SP-359*, 747–752, 1993.

Brüning, C., S. Hasselmann, K. Hasselmann, S. Lehner, and T. Gerling, A first evaluation of ERS-1 synthetic aperture radar wave mode data, *Global Atmos. Ocean Syst., 2*, 61–98, 1994.

Chapron, B., T. Elfouhaily, and V. Kerbaol, Calibration and validation of ERS wave mode products, *Doc. DRO/OS/95-02*, Inst. Fr. de Rech. pour l'Exploit. de la Mer, Brest, France, March 1995.

Engen, G., and H. Johnsen, SAR ocean wave inversion using image cross spectra, *IEEE Trans. Geosci. Remote Sens., 33*, 1047–1056, 1995.

European Centre for Medium-Range Weather Forecasts, (ECMWF), User guide to ECMWF products, *Meteorol. Bull. M3.2*, edition 2.1, Reading, England, 1995.

European Space Agency (ESA), ERS user handbook, *Eur. Space Agency Spec. Publ., ESA SP-1148*, 30–31, 1993.

European Space Agency (ESA), Application achievements of ERS-1, *Eur. Space Agency Spec. Publ., ESA SP-1176/III*, pp. 15–18, 1996.

European Space Agency (ESA), ENVISAT-1, Mission and system summary, report, Eur. Space Res. and Technol. Cent., Noordwijk, Netherlands, March 1997.

Fairall, C. W., E. F. Bradley, D. P. Rogers, J. B. Edson, and G. S. Young, Bulk parameterization of air-sea fluxes for Tropical Ocean-Global Atmosphere Coupled Ocean-Atmosphere Response Experiment, *J. Geophys. Res., 101*, 3747–3764, 1996.

Feindt, F., Radar-Rückstreuexperimente am Wind-Wellen-Kanal bei sauberer und filmbedeckter Wasseroberflache, Ph.D. thesis, Fachbereich Geowiss., Univ. of Hamburg, Germany, 1985.

Geernaert, G. L., Bulk parameterizations for the wind stress heat fluxes, in *Surface Waves and Fluxes*, vol. 1, edited by G. L. Geernaert and W. L. Plant, chap. 5, pp. 91–172, Kluwer Acad., Norwell, Mass., 1990.

Gerling, T. W., Partitioning sequences and arrays of directional wave spectra into component wave systems, *J. Atmos. Oceanic Technol., 9*, 444–458, 1992.

Günther, H., S. Hasselmann, and P. A. E. M. Janssen, WAModel Cycle 4 (revised version), *Tech. Rep. 4*, Ger. Clim. Comput. Cent., Hamburg, Germany, 1992.

Hansen, B., C. Brüning, and C. Staabs, Global comparison of significant wave heights derived from ERS-1 SAR wave mode, ERS-1 altimeter and TOPEX altimeter data, in *Proceedings of the Second ERS-1 Symposium, Hamburg, Germany, 11–14 October 1993, Eur. Space Agency Spec. Publ., ESA SP-361*, 33–36, 1994.

Harger, R. O., *Synthetic Aperture Radars: Theory and Design*, Academic, San Diego, Calif., 1970.

Hasselmann, K., On the spectral dissipation of ocean waves due to white capping, *Boundary Layer Meteorol., 6*, 107–127, 1974.

Hasselmann, K., and S. Hasselmann, On the nonlinear mapping of an ocean wave spectrum into a synthetic aperture radar image spectrum and its inversion, *J. Geophys. Res., 96*, 10,713–10,729, 1991.

Hasselmann, K., R. K. Raney, W. J. Plant, W. Alpers, R. A. Shuchman,

D. R. Lyzenga, C. L. Rufenach, and M. J. Tucker, Theory of synthetic aperture radar ocean imaging, A MARSEN view, *J. Geophys. Res., 90*, 4659–4686, 1985.

Hasselmann, K., S. Hasselmann, E. Bauer, C. Brüning, S. Lehner, H. Gaber, and P. Lionello, Development of a satellite SAR image spectra and altimeter wave height data assimilation system for ERS-1, *Rep. 19*, Max-Planck-Inst. für Meteorol., Hamburg, Germany, July 1988.

Hasselmann, K., S. Hasselmann, C. Brüning, and A. Speidel, Interpretation and application of SAR wave image spectra in wave models, in *Directional Ocean Wave Spectra*, edited by R. C. Beal, pp. 117–124, Johns Hopkins Univ. Press, Baltimore, Md., 1991.

Hasselmann, S., and K. Hasselmann, Computations and parameterisations of the nonlinear energy transfer in a gravity wave spectrum, I, A new method for efficient computations of the exact nonlinear energy transfer integral, *J. Phys. Oceanogr., 15*, 1369–1377, 1985.

Hasselmann, S., K. Hasselmann, J. H. Allender, and T. P. Barnett, Computations and parameterisations of the nonlinear energy transfer in a gravity wave spectrum, II, Parameterisations of the nonlinear energy transfer for application in wave models, *J. Phys. Oceanogr., 15*, 1378–1391, 1985.

Hasselmann, S., C. Brüning, and P. Lionello, Towards a generalized optimal interpolation method for the assimilation of ERS-1 SAR retrieved wave spectra in a wave model, in *Proceedings of the Second ERS-1 Symposium, Hamburg, Germany, 11–14 October 1993, Eur. Space Agency Spec. Publ., ESA SP-361*, 21–25, 1994.

Hasselmann, S., C. Brüning, K. Hasselmann, and P. Heimbach, An improved algorithm for the retrieval of ocean wave spectra from SAR image spectra, *J. Geophys. Res., 101*, 16,615–16,629, 1996.

Hasselmann, S., P. Lionello, and K. Hasselmann, An optimal interpolation scheme for the assimilation of spectral wave data, *J. Geophys. Res., 102*, 15,823–15,836, 1997.

Hasselmann, S., P. Heimbach, and C. Bennefeld, Algorithm for retrieving ocean wave spectra from SAR image spectra, technical report, Ger. Clim Comput. Cent., Hamburg, Germany, 1998.

Heimbach, P., S. Hasselmann, C. Brüning, and K. Hasselmann, Application of wave spectral retrievals from ERS-1 SAR wave mode data for improved wind and wave field analyses, in *Proceedings of the Second ERS Applications Workshop, London, 6–8 December 1995, Eur. Space Agency Spec. Publ., ESA SP-383*, 303–308, February 1996.

Jähne, B., and E. C. Monahan (Eds.), *Air-Water Gas Transfer*, AEON, Hanau, Germany, 1995.

Janssen, J. A. M., Does wind stress depend on sea-state or not?–A statistical error analysis of HEXMAX data, *Boundary Layer Meteorol., 83*, 479–503, 1997.

Janssen, P. A. E. M., Wave-induced stress and the drag of the air flow over sea waves, *J. Phys. Oceanogr., 19*, 745–754, 1989.

Janssen, P. A. E. M., Quasi-linear theory of wind-wave generation applied to wave forecasting, *J. Phys. Oceanogr., 21*, 1631–1391, 1991.

Janssen, P. A. E. M., Experimental evidence of the effect of surface waves on the airflow, *J. Phys. Oceanogr., 22*, 1600–1604, 1992.

Janssen, P. A. E. M., and P. Viterbo, Ocean waves and the atmospheric climate, *J. Clim., 9*, 1269–1287, 1996.

Janssen, P. A. E. M., B. Hansen, and J. Bidlot, Verification of the ECMWF wave forecasting system against buoy and altimeter data, *Tech. Memo. 229*, Eur. Cent. for Medium Range Weather Forecasts, Reading, England, July 1996.

Johnsen, H., Multi-look versus single-look processing of synthetic aperture radar images with respect to ocean wave spectra estimation, *Int. J. Remote Sens., 13*, 1627–1643, 1992.

Kerbaol, V., and B. Chapron, Calibration and validation of ERS-1/2 wave mode products, report, Inst. Fr. de Rech. pour l'Exploit. de la Mer, Brest, France, October 1996.

Komen, G. J., L. Cavaleri, M. Donelan, K. Hasselmann, S. Hasselmann, and P. A. E. M. Janssen, *Dynamics and Modelling of Ocean Waves*, 560 pp., Cambridge Univ. Press, New York, 1994.

Komen, G. J., P. A. E. M. Janssen, V. K. Makin, C. Mastenbroek, and W. A. Oost, On the sea state dependence of the Charnock parameter, *Global Atmos. Ocean Syst.*, in press, 1998.

Krogstad, H. E., A simple derivation of Hasselmann's nonlinear ocean-synthetic aperture radar transform, *J. Geophys. Res., 97*, 2421–2425, 1992.

Krogstad, H. E., The speckle spectrum of the ERS-1 wave mode product, *SINTEF Industrial Mathematics Rep. STF10 A94008*, Trondheim, Norway, 1994.

Krogstad, H. E., O. Samset, and P. W. Vachon, Generalization of the

non-linear ocean-SAR transform and a simplified SAR inversion algorithm, *Atmos. Ocean*, *32*, 61–82, 1994.

Large, W. G., J. Morzel, and G. B. Crawford, Accounting for surface wave distortion of the marine wind profile in low-level ocean storm wind measurements, *J. Phys. Oceanogr.*, *25*, 2959–2971, 1995.

Lionello, P., H. Günther, and P. A. E. M. Janssen, Assimilation of altimeter data in a global third-generation wave model, *J. Geophys. Res.*, *97*, 14,453–14,474, 1992.

Lionello, P., H. Günther, and B. Hansen, A sequential assimilation scheme applied to global wave analysis and prediction, *J. Mar. Syst.*, *6*, 87–107, 1995.

Mastenbroek, C., G. Burgers, and P. A. E. M. Janssen, The dynamical coupling of a wave model and a storm surge model through the atmospheric boundary layer, *J. Phys. Oceanogr.*, *23*, 1856–1866, 1993.

Miles, J., On the generation of surface waves by shear flows, *J. Fluid Mech.*, *3*, 185–204, 1957.

Monaldo, F. M., and R. C. Beal, Real-time observations of Southern Ocean wave fields from the shuttle imaging radar, *IEEE Trans. Geosci. Remote Sens.*, *33*, 942–949, 1995.

Monaldo, F. M., and D. R. Lyzenga, On the estimation of wave slope- and height variance spectra from SAR imagery, *IEEE Trans. Geosci. Remote Sens.*, *24*, 543–551, 1986.

Monaldo, F. M., and D. R. Lyzenga, Comparison of shuttle imaging radar–B ocean wave spectra with linear model predictions based on aircraft measurements, *J. Geophys. Res.*, *93*(C12), 15,374–15,388, 1988.

Peixoto, J. P., and A. H. Oort, *The Physics of Climate*, Am. Inst. of Phys., New York, 1992.

Plant, W. J., and W. Alpers, An introduction to SAXON-FPN, *J. Geophys. Res.*, *99*, 9699–9703, 1994.

Preisendorfer, R. P., *Principal Component Analysis*, Elsevier, New York, 1988.

Rieder, K. F., Analysis of sea-surface drag parameterizations in open ocean conditions, *Boundary Layer Meteorol.*, *83*, 355–377, 1997.

Rieder, K. F., J. A. Smith, and R. A. Weller, Observed directional characteristics of the wind, wind stress, and surface waves on the open ocean, *J. Geophys. Res.*, *99*, 22,589–22,596, 1994.

Smith, S. D., et al., Sea surface wind stress and drag coefficients: The HEXOS results, *Boundary Layer Meteorol.*, *60*, 109–142, 1992.

Snodgrass, F. E., G. W. Groves, K. Hasselmann, G. R. Miller, W. H. Munk, and W. H. Powers, Propagation of ocean swell across the Pacific, *Philos. Trans. R. Soc. London A*, *249*, 431–497, 1966.

Snyder, R. L., F. W. Dobson, J. A. Elliott, and R. B. Long, Array measurements of atmospheric pressure fluctuations above surface gravity waves, *J. Fluid Mech.*, *102*, 1–59, 1981.

Tolman, H. L., Effects of numerics on the physics in a third-generation wind-wave model, *J. Phys. Oceanogr.*, *22*, 1095–1111, 1992.

Tolman, H. L., On the selection of propagation schemes for a spectral wind-wave model, *Off. Note 411*, Natl. Weather Serv., La Jolla, Calif., 1995.

Vachon, P. W., and R. K. Raney, Resolution of the ocean wave propagation direction in SAR imagery, *IEEE Trans. Geosci. Remote Sens.*, *29*, 105–112, 1991.

von Storch, H., J. Guddal, K. A. Iden, T. Jonson, J. Perlwitz, M. Reistad, J. de Ronde, H. Schmidt, and E. Zorita, Changing statistics of storms in the North Atlantic?, *Rep. 116*, Max-Planck-Inst. für Meteorol., Hamburg, Germany, 1993.

Wave Model Development and Implementation (WAMDI) Group, The WAM model–A third generation ocean wave prediction model, *J. Phys. Oceanogr.*, *18*, 1775–1810, 1988.

Wave and Storms in the North Atlantic (WASA) Group, The WASA project: Changing storm and wave climate in the northeast Atlantic and adjacent seas?, paper presented at the Fourth International Workshop on Wave Hindcasting and Forecasting, Environ. Can., Banff, Alberta, Canada, Oct. 16–20, 1995.

Weber, S. L., H. von Storch, P. Viterbo, and L. Zambresky, Coupling an ocean wave model to an atmospheric general circulation model, *Clim. Dyn.*, *9*, 63–69, 1993.

Weisse, R., and E. F. Alvarez, The European Coupled Atmosphere Wave Ocean Model ECAWOM, *Rep. 238*, Max-Planck-Inst. für Meteorol., Hamburg, Germany, July 1997.

Wilde, A., C. Brüning, W. Alpers, V. Etkin, K. Litovchenko, A. Ivanov, and V. Zajtsev, Comparison of ocean wave imaging by ERS-1 and ALMAZ-1 synthetic aperture radar, in *Proceedings of the Second ERS-1 Symposium, Hamburg, Germany, 11–14 October 1993, Eur. Space Agency Spec. Publ., ESA SP-361*, 239–245, 1994.

Young, I. R., W. Rosenthal, and F. Ziemer, A three-dimensional analysis of marine radar images for the determination of ocean wave directionality and surface currents, *J. Geophys. Res.*, *90*, 1049–1059, 1985.

Young, I. R., S. Hasselmann, and K. Hasselmann, Computations of the response of a wave spectrum to a sudden change in wind direction, *J. Phys. Oceanogr.*, *17*, 1317–1338, 1987.

K. Hasselmann, S. Hasselmann, and P. Heimbach, Max-Planck-Institut für Meteorologie, Bundesstrasse 55, 20146 Hamburg, Germany. (e-mail: klaus.hasselmann@dkrz.de; susanne.hasselmann@dkrz.de; heimbach@dkrz.de)